Tribological characterization and in-silico wear assessment of lower limb joint prosthesis

Massimiliano Merola

Alla mia famiglia,
per avermi mostrato
l’amore incondizionato.

Unione Europea

UNIVERSITÀ DEGLI
STUDI DI SALERNO

FONDO SOCIALE EUROPEO

Programma Operativo Nazionale 2000/2006
"Ricerca Scientifica, Sviluppo Tecnologico, Alta Formazione"
Regioni dell'Obiettivo 1 – Misura III.4
"Formazione superiore ed universitaria"

Department of Industrial Engineering

Ph.D. Course in Industrial Engineering
(XVI Cycle-New Series, XXX Cycle)

Tribological characterization and in-silico wear assessment of lower limb joint prosthesis

Supervisor
Prof. Alessandro Ruggiero

Ph.D. student
Massimiliano Merola

Scientific Committee
Dott. Saverio Affatato
Prof. Roque Calvo Iranzo

Scientific Referee
Prof. Sergej Hloch
Prof. Stefania Bruschi

Ph.D. Course Coordinator
Prof. Ernesto Reverchon

List of publications

Publications on international journals

1. S Affatato, A Ruggiero, M Merola, Advanced Biomaterials in Hip Joint Arthroplasty. A Review on Polymer and Ceramics Composites as Alternative Bearings (2015) Composites Part B: Engineering.
2. M Merola, P Carlone, A Ruggiero, V-M Archodoulaki, Mechanical and tribological characterization of composite laminates manufactured by liquid composite molding processes Key Engineering Materials 651-653 (2015).
3. A Ruggiero, M Merola, P Carlone, V-M Archodoulaki, Tribo-mechanical characterization of reinforced epoxy resin under dry and lubricated contact conditions (2015) Composites Part B: Engineering
4. A Sorrentino, C Altavilla, M Merola, A Senatore, P Ciambelli, S Iannace, Nanosheets of MoS2-Oleylamine as Hybrid Filler for Self-Lubricating Polymer Composites: Thermal, Tribological, and Mechanical Properties. Polymer Composites 36 (6) (2015).
5. A Ruggiero, R D'Amato, E Gómez, M Merola, Experimental comparison on tribological pairs UHMWPE/TIAL6V4 alloy, UHMWPE/AISI316L austenitic stainless and UHMWPE/AL2O3 ceramic, under dry and lubricated conditions Tribology International 96 (2016).
6. A Ruggiero, V D'Agostino, M Merola, P Valasek, K Dedicova, Friction and wear characterization of a new ecological composite: glass waste beads reinforced epoxy. International Journal of Mechanics 10 (2016).
7. A Ruggiero, P Valasek, M Merola, Friction and Wear Behaviors of Al/Epoxy Composites during Reciprocating Sliding Tests Manufacturing Technology 15 (2015).
8. M Merola, A Ruggiero, J-S De Mattia, S Affatato, On the tribological behavior of retrieved hip femoral heads affected by metallic debris. A comparative investigation by stylus and optical profilometer for a new roughness measurement protocol Measurement 90 (2016).
9. A Ruggiero, R D'Amato, M Merola, P Valášek, M Müller, On the tribological performance of vegetal lubricants: experimental investigation on Jatropha Curcas L. oil. Procedia Engineering 149 (2016).
10. A Astarita, F Rubino, P Carlone, A Ruggiero, C Leone, S Genna, M Merola, A Squillace, On the Improvement of AA2024 Wear

Properties through the Deposition of a Cold-Sprayed Titanium Coating. Metals 6 (8) (2016).

11. S Affatato, A Ruggiero, M Merola, S Logozzo, Does metal transfer differ on retrieved Biolox® Delta composites femoral heads? Surface investigation on three Biolox® generations from a biotribological point of view Composites Part B: Engineering 113 (2017).
12. A Ruggiero, R D'Amato, M Merola, P Valašek, M Müller, Tribological Characterization of Vegetal Lubricants: Comparative Experimental investigation on Jatropha Curcas L. oil, Rapeseed Methyl Ester oil, Hydrotreated Rapeseed oil. Tribology International 109 (2017).
13. A Ruggiero, M Merola, S Affatato, On the Biotribology of Total Knee Replacement: a new Roughness Measurements Protocol on in-vivo Condyles considering the Dynamic Loading from Musculoskeletal Multibody Model. Measurement 112 (2017).

Publications in conference proceedings

1. V-M Archodoulaki, M Merola, D Kastanis, T Koch, P Carlone, Influence of the impregnation velocity on impregnation quality and mechanical properties of Vacuum Assisted Resin Transfer Moulding (VARTM) 20th Symposium on Composites, 2015 Vienna.
2. A Ruggiero, V D'Agostino, M Merola, P Valášek, K Dedicova, The Tribological Effect of Glass Particles Waste Reinforcement within Epoxy Resin, WSEAS Conference 2015, Salerno.
3. A Astarita, F Rubino, P Carlone, A Ruggiero, C Leone, M Merola, A Squillace, Influence of Selective Post-Deposition Laser Treatment on Tribological and Wear Properties of Cold Sprayed Titanium Coatings. Proceedings of the Twenty Ninth International Conference on Surface Modification Technologies XXIX, 2016 Milan.
4. A Ruggiero, M Merola, (Bio)Tribology of lower limb synovial joint: Recent Investigations and future research trends. Workshop dell'Associazione Italiana di Tribologia AIT "Tribologia e Industria" 2016, Salerno.
5. A Ruggiero, S Affatato, M Merola, Metal transfer and surface roughness in ceramic femoral heads: recent investigations and future research trends. Proceedings of ECOTRIB 2017, Ljubljana.
6. A Ruggiero, V D'Agostino, M Merola, R D'Amato, On the wear protection ability of three eco-friendly base lubricants: first results from wear debris analysis. Proceedings of the XXIII Conference of the Italian Association of Theoretical and Applied Mechanics, 2017 Salerno.

7. A Ruggiero, S Affatato, M Merola, M-C De Simone, FEM analysis of metal on UHMWPE total hip prosthesis during normal walking cycle. Proceedings of the XXIII Conference of the Italian Association of Theoretical and Applied Mechanics, 2017 Salerno.

Index

II

Abstract

Hip and knee articulations are the main joints in human body and they have the duty of sustaining heavy loads. This task is normally well performed by a healthy joint but, in some cases, the occurrence of diseases can affect the functionality of the joint: when ambulation is limited, surgery is required.

Even if the orthoprosthesis is one of the most effective and successful surgical procedure in the modern medicine, around the 10% of the implanted devices will fail and so require a second surgery. The revision operation is a difficult procedure which needs a long scheduling prior to surgery.

Currently, hip and knee joint prostheses are analysed and subjected to simulation tests before receiving the required approval for clinical use. These tests are performed with the aim of establish the behaviour of the prosthesis, assess the wear rate of the components and the surface finishing. However, wear tests on a simulator are long and expensive due to the large number of cycles at low frequency that must be executed. The idea was to move toward an in-silico wear assessment.

In order to define which are the most influencing parameters on the tribology of the implants it was investigated the Metal Transfer. It is a migration phenomenon of metal particles found on femoral heads and on acetabular cups of retrieved ceramic hip prostheses, which implies an important alteration of the bearing surface. The presence of transferred metal on ceramic heads changes the surface properties and thus affects lubrication, friction and wear. They were studied 35 ceramics femoral heads of different materials, including zirconia, *Biolox® Delta*, *Biolox®* and *Biolox® Forte*. Differences in surface characteristic appear, as an evidence of the phenomenon, between the affected and unaffected areas.

As in literature they can be found several wear models introducing contact pressure distribution as input data, an aim of the study was to develop a finite elements model of the hip joint, for the calculation of the stress map on the acetabular cup. The proposed model consists of a hard-on-soft implant (metal head and polyethylene cup).

From a multibody analysis, they were gained the forces and the rotations taking place on the articulations of the hip and the knee. The *Gait Analysis* was used to assess the human gait, reached by solving the *Inverse Dynamics Problem*. It was studied the influence of the load distribution on knee implants, to assess if it causes a different wear and surface topography on the menisci.

The forces and motion of the hip joint were used as input parameters to define the dynamic loading of the finite element model. The femoral head was modelled as a rigid body, whereas for the acetabular cup it was selected the UHMWPE material. The material is assumed to be homogenous, isotropic and

linearly elastic. Two cases of studies were analysed, the dry and the boundary lubricated contacts, which are discerned by a different friction coefficient gained by experimental investigations. Furthermore, it was investigated the influence of the radial clearance presence on the stress distribution. The stress state obtained can be applied to the evaluation of the cup wear. The linear wear at any point on the surface along the gait cycle was derived by Archard's wear model.

Introduction

The main aim of this research work is to obtain a better comprehension of the tribological aspects related to the hip and knee implants in human beings. As consequence of this target, a wide range of aspects, in the biotribology and biomechanics fields, has been investigated during the development of this PhD project.

To give a useful contribution to the hip and knee implant investigation, it has been conducted both experimental characterizations and model simulations. The final aim of this research arm is to obtain a complete model, which could avoid the standard time-consuming investigation procedure. In fact, to investigate on the condition and evolution of an implant there are different possibilities. There is the chance to investigate on the actual condition of a joint prosthesis as it is implanted in a living human, these procedures are therefore called *in-vivo*. To investigate in this way, many techniques are available, from the standard radiography to the more complex microtomography (see **Figure1a**). With these techniques it is possible to estimate the current wear volume of an implant or to find other issues, as the osteolysis. Even though, these procedures are strongly dependent on the single

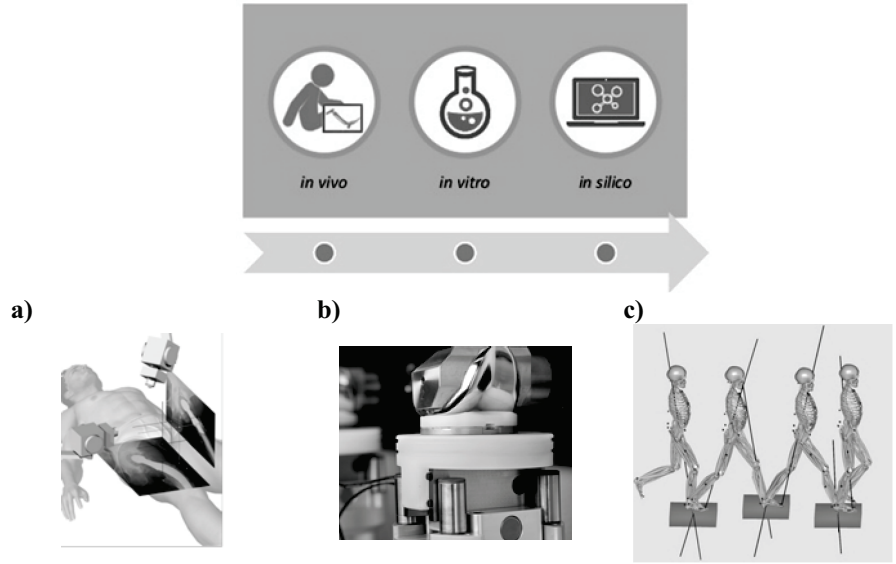

Figure 1: *From in-vivo to in-silico characterization of implants. a) in-vivo 3D radiography; b) in-vitro knee joint simulator; c) musculoskeletal model of a human body.*

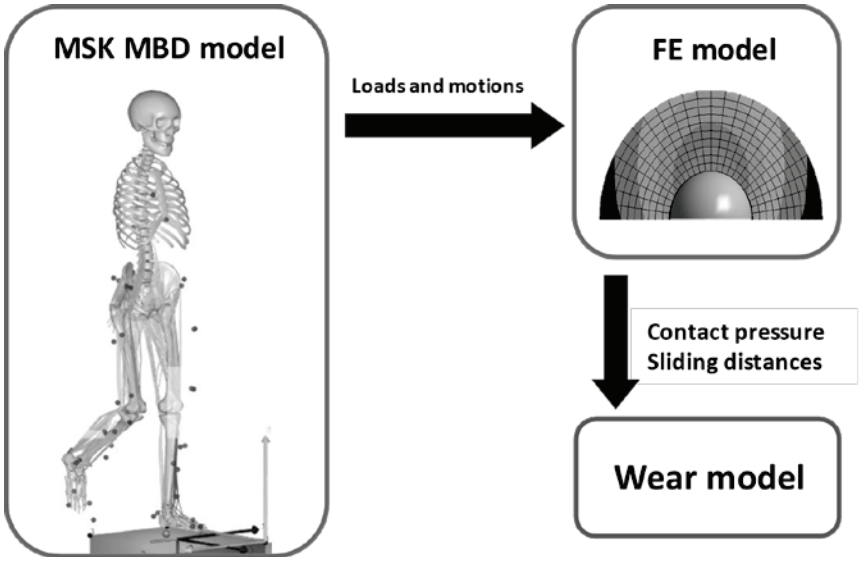

Figure 2: *Flowchart of the procedure from the multibody system to the analysis of the wear.*

patient under observation, thus it is not possible to define the behaviour of a certain kind of prosthesis.

On the other hand, there is the possibility to characterize an implant by subjecting it to *in-vitro* analysis (**Figure1b**). These tests are the most common way to obtain insight into how an implant is going to work and how long it will last once implanted. As these methodologies require significant amount of time and money, in term of instruments and human resources, there is the need to obtain an *in-silico* analysis of the joint implant (**Figure1c**). Which could also be more flexible, by considering and adapting the simulation to the specific requirements of a particular category of patients (or even to the single patient). This *in-silico* simulation should therefore consider the activity of patients within the model, where the dynamic load can be evaluated as function of a specific motion. Therefore, the idea was to develop a musculoskeletal multibody model, from which obtain the dynamic loads acting on the knee and hip joints. These results could be used as input parameters for a finite element model with which obtain the tensional stress, the elastic deformation and the sliding distance covered. As consequence, the value of the linear wear on the coupled surface could be extracted from the application of a wear model.

I Chapter
The Lower Limb Joints

The lower limb of a human being is composed of three major parts: a girdle realized by the hip bones, the thigh, the leg and the foot. Their major duties are to support weight, balance gravity and realize ambulation. The lower limb is subdivided by the hip joint, knee joint and ankle joint. In this thesis they will be analysed the hip and the knee joint implants, as these are the two most widespread joint prosthesis in medical surgery.

I.1 The Hip Joint

I.1.1 The hip joint anatomy

The hip joint is a kind of diarthrodial joint, also called a ball-in-socket joint; the hip bone socket constitutes the socket, while the head of the femur is the ball. Three different bones (the *pubis*, the *ischium* and the *ilium*) form the coxal bone during skeletal growth, since they combine to each other (see **Figure I.1** from [1]). The coxal bone can also be referred to as hip bone or *innominate* (from the Latin *innominatum*, i.e. nameless). The right and left innominates connect with each other anteriorly and posteriorly, respectively at the pubic *symphysis* and at the *sacrum*. The complete osteoligamentous ring is called the *pelvis*. The pelvis has fundamentals functions: it serves as common attachment for many large muscles of the lower limb; it transmits the weight of the upper body to the lower part during walking and standing; it also supports the organs involved with bladder, bowel and reproductive functions.

The pubis forms the foremost and average piece of the coxal bone and articulate with the contralateral pubis that shuts the front piece of the pelvis. The external surface of the pelvis has three main characteristics. The large fan-shaped *wing* (or *ala*) of the ilium forms the superior half of the innominate. Just below the wing is the deep, cup-shaped *acetabulum*. Below it, there is the

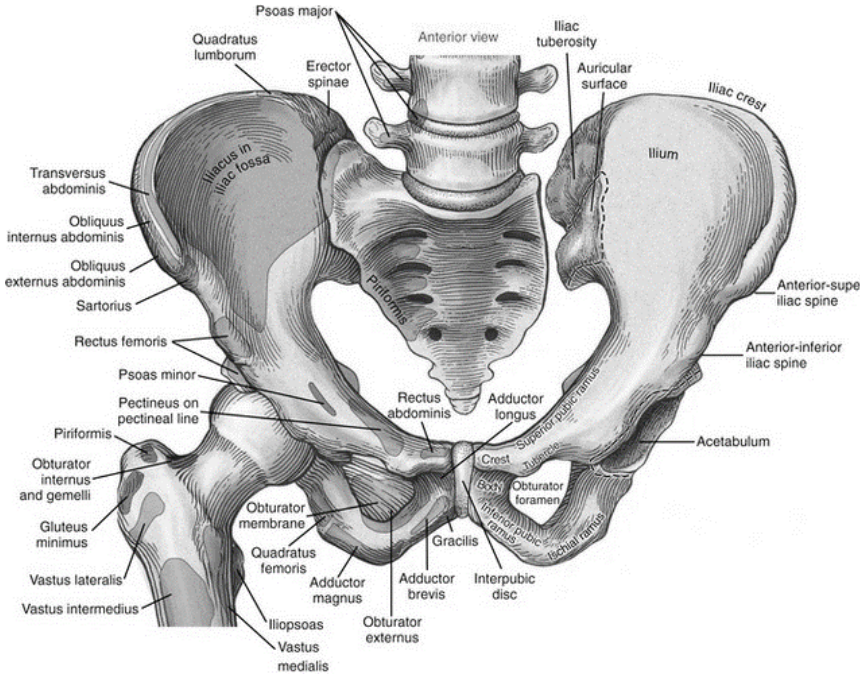

Figure I.1: *Hip joint anatomy. Proximal attachments are indicated in red, distal attachments in grey. A section of the left side of the sacrum is removed to expose the auricular surface of the sacroiliac joint.*

obturator foramen, which is the largest foramen in the body. This foramen is covered by an *obturator membrane*.

The lower and back parts of the coxal bone are framed by the ischium. The sharp *ischial spine* projects form the posterior side of the ischium. Posteriorly there is the large, stout *ischial tuberosity*. This structure serves as the proximal attachment for many muscles of the lower body.

The acetabulum forms the socket of the hip. All three bones of the pelvis contribute to the formation of the acetabulum: the ilium and ischium contribute for a 75%, whereas the pubis contributes for approximately 25%.

The femur is the longest and strongest bone of the human body. At its end the is the femoral head which articulates with the acetabulum. The femoral neck connects the head to the shaft of the bone. The neck is necessary to displace the proximal shaft of the femur away from the joint. The shaft of the femur displays a slight anterior convexity. As loaded with body weight it bows very slightly, dissipating the stresses along through compression along its posterior part and tension along its anterior part. This feature allows to sustain higher loads than if it was straight.

The hip joint backings the body and oversees the body weight. The focal point of turn of the hip is the centre of the femoral head. During standing, the centre of gravity of the body is before the second sacral vertebra. It moves

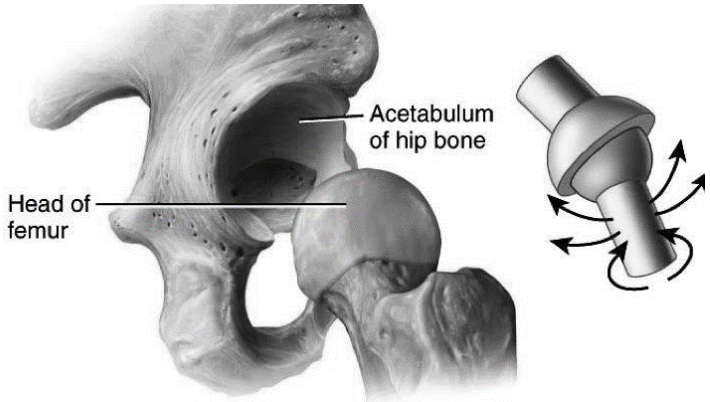

Figure I.2: *The hip joint, composed by the articulating surfaces of the femoral head and the acetabulum of the hip bone is equivalent to a ball-in-socket joint.*

distally and far from the supporting leg amid a solitary leg position; along these lines, the body weight functions as a lever stretching out from the focal point of gravity towards the focal point of revolution of the hip [2], [3].

I.1.2 Design

The hip is a ball-in-socket joint of the body (**Figure I.2**), secured within the acetabulum by a large set of connective tissues and muscles. The set of cartilage, muscles and cancellous bone in the proximal femur help reducing the large loads that act on the hip. A failure of any of these protective elements, due to diseases or traumatic reasons, often leads to a worsening of the joint structure.

I.1.2.1 Femoral head

On average, the centres of the two femoral heads, in an adult person, are 17.5 cm apart from each other. The head shapes about two thirds of a nearly perfect sphere. Its entire surface is covered by articular cartilage, except for a pit (called *fovea*) slightly posterior to the centre of the head itself. The primary blood supply to the head and neck is through the medial and lateral circumflex arteries.

I.1.2.2 Acetabulum

The acetabulum is a hemispheric cuplike socket that houses the femoral head. About 60 to 70 degrees of its rim are incomplete near its inferior pole, forming the *acetabular notch*. The contact between the acetabulum and the femoral head happens only along its horseshoe-shaped lunate surface. This surface is covered by articular cartilage, the thickest cartilage region

corresponds to the highest loaded part during walking. During walking, hip forces fluctuate from 13% to 300% of the body weight, respectively during mid-swing phase and mid stance phase (see section **IV.3** "The human gait"). During the stance phase this lunate surface flattens whereas the notch widens slightly, resulting in an increased contact area to reduce peak pressure.

I.1.3 Range of motion of the hip joint

This diarthrodial ball-and-socket articulation has three degrees of freedom expressible by the rotations on the anatomical planes (as shown in **Figure I.3**):

- ❖ flexion/extension in the sagittal plane;
- ❖ abduction/adduction in the frontal plane;
- ❖ medial/lateral rotation in the transverse plane.

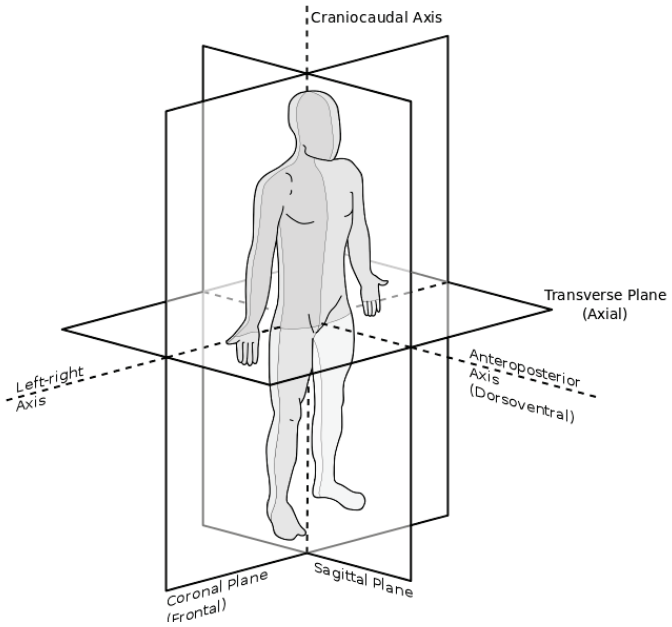

Figure I.3: *Anatomical planes*

I.1.3.1 Determination of the resultant hip force

Static loading of the hip joint could be easily approximated through a 2D analysis performed in the frontal plane. When supporting the upper body weight, the centre of gravity is centred between the two hips and the load is divided equally in both hips. Therefore, in this condition, the weight is supported equally on the femoral heads, and the resultant force vectors are vertical.

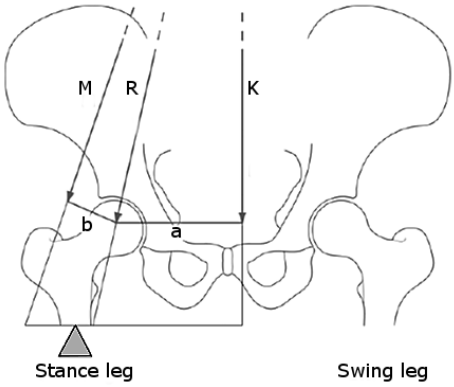

Figure I.4 *Force distribution on the pelvis-hip*

In a single leg stance, the centre of gravity moves away from the supporting leg, as the other leg is now part of the body mass. This force yields a turning motion around the centre of the femoral head, the moment is due to the body weight, *K*, and its moment arm, *a*. The muscles that resist this moment are offset by the combined abductor muscles, *M* (see **Figure I.4**).

The amplitude of the forces depends critically on the lever arm ratio, which is the ratio between the body weight moment arm and the abductor moment arm (*a/b*). Typical amplitude for the single stance phase are three times the bodyweight Therefore, anything that rises the lever arm ratio also increases the abductor muscle force required for walk and subsequently the force on the head of the femur (as shown in **Figure I.5**).

The resultant hip force can be estimated in static or dynamic conditions. The muscles in the static models are supposed to be force generators with fixed coordinates.

To estimate in a non-invasive way the dynamic hip force it is required the use of the dynamic biomechanical models. They are based on laboratory measurements with contact force plates, kinematic data of body movement

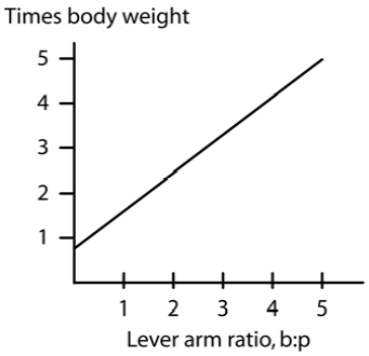

Figure I.5: *Abductor muscle force evolution with lever arm ratio.*

and inverse dynamic analysis of the moving segments, this analysis will be object of the work described in **section IV.2**. If walking generates significant load to the hip joint, jogging, running and contact sports produce significantly greater forces. To verify the amplitude of the loads made with free-body calculations, many *in vivo* measurements have been made using implants instrumented with transducer (stain-gauges). These studies results are summarized in **Table I.1**. These researches show that unexpected events such as stumbling can produce resultant forces more than height times body weight. It is important to remark that these analyses are elaborate in patients which undergone total hip replacement, thus they could not be representative of the actual physiology of a normal hip.

Table I.1 : *Peak force found with in-vitro experiments*

Activity	Typical Peak Force (BW)	Total Number of Patients	Time Since Surgery (months)	References
Walking slow	1.6-4.1	9	1-30	[4]–[7]
Walking normal	2.1-3.3	6	1-31	[5]
Walking fast	1.8-4.3	7	2-30	[4]–[7]
Jogging running	4.3-5.0	2	6-30	[6], [7]
Ascending stairs	1.5-5.5	8	6-33	[4]–[7]
Descending stairs	1.6-5.1	7	6-30	[4]–[7]
Standing up	1.8-2.2	4	11-30	[5]
Sitting down	1.5-2.0	4	11-30	[5]
Knee bend	1.2-1.8	3	11-14	[5]
Stumbling	7.2-8.7	2	4-18	[6], [8]

I.1.4 Hip joint diseases

The hip joint, as every other body joints, suffers issues which engrave with ageing. Most of these diseases lead to severe disability and chronic pain. As consequence of this people are forced to seek surgical interventions. A list [9] of the common hip diseases is presented below:

- **Osteolysis**: It is local loss of bone tissue due to wear. Destruction of bone takes place especially by bone resorption through removal or loss of calcium. Osteolysis may be evident in neoplastic, infectious, metabolic, traumatic, vascular, congenital and articular disorders.
- **Osteoarthritis**: It is worsening arthritis disease, a wearing out involving the failure of cartilage in the joints, it is one of the oldest and most common types of arthritis. Cartilage is a fundamental part of the joint and

cushions ends of the mating bones. The bones get deformed, and even small movements cause severe friction forces between the ball and the socket of the hip, causing acute pain. This disease changes the loading mode and magnitude, causing a continuous local overloading of the articular cartilage, which results in a permanent damage since its physiological nutrition cannot proceed.

- **Avascular Necrosis:** This is caused by lack of blood supply into the bone. This condition may eventually lead to bone death. If avascular necrosis progresses, bone and the surrounding joint surface may collapse.
- **Rheumatoid arthritis**: This disease concerns inflammation in the lining of the joints and/or other internal organs. RA yields chemical changes in the synovium that became thicker and inflamed. In turn, the synovial fluid destroys cartilage. Rheumatoid arthritis normally affects several joints and it is a chronic inflammatory joint disorder.
- **Fracture neck of femur**: The fracture of the neck of femur. The structure of the head and neck of femur is developed for the transmission of body weight efficiently, by proper distribution of the bony trabeculae in the neck. The occurrence of fracture neck of femur is higher in old age.
- **Developmental dysplasia**: In the hip joint, it is a condition in which the femoral head has an irregular connection to the acetabulum. It includes frank dislocation (luxation), partial dislocation (subluxation), or instability of the hip, in which the femoral head comes in and out of the socket. Radiographic abnormalities reflect inadequate formation of the acetabulum.
- **Paget's disease**: It is a metabolic bone disorder of unidentified cause. This commonly affects older people. Bone is a living tissue and is constantly being renewed, paget's disease of bone causes increased and irregular development of bone. The bone cells, which are responsible for dissolving body's old bones and replacing them with new ones, become out of control.
- **Arthrodesis (Fusion) Takedown**: Arthrodesis is the surgical fixation of joints by promoting fusion through bone cell proliferation. It provides potential of a painless, stable base of support. Most frequent complication of arthrodesis is non-union. Main causes of non-union includes bone loss, continuing infection, incomplete bone apposition, limb misalignment, and inadequate immobilization.
- **Tumour**: The surgical problems encountered with osteoid osteomas of the proximal femur are distinctive. All together surgical excision is made difficult due to the difficult definition of tumour boundaries. This can lead to extensive resection needing internal fixation or bone grafting.

I.2 The Knee Joint

I.2.1 The knee joint anatomy

The knee is the main human articulation and one of the most important one. It is composed by the end inferior of the femur, by the top end of the *tibia* and by the *patella* (or kneecap) as shown in **Figure I.6**. These extreme parts are covered by the cartilage in the zone where they touch each other, the cartilage is a hard and smooth tissue that protects bones and allows their movements.

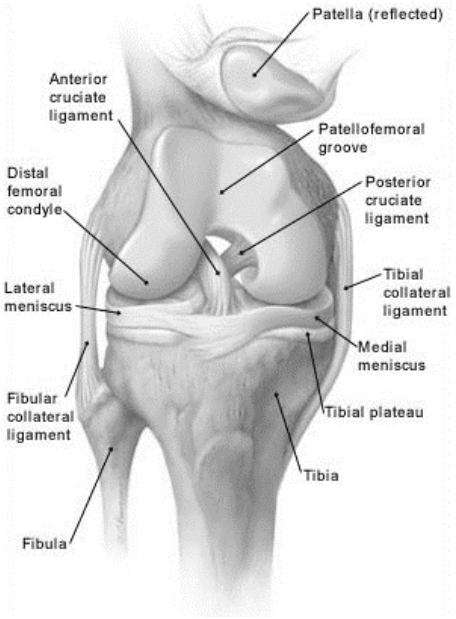

Figure I.6: *Knee joint essential anatomy.*

The *menisci* are located between the femur and the tibia and act as "seal". In term of gross anatomy, the menisci are C-shaped or semi-circular fibrocartilaginous structures with bony attachments at the anterior and posterior aspects of the tibial plateau. The Medial Meniscus (MM) is C-shaped, with the posterior horn lager than the anterior one. The anterior horn connection is mutable, and this should be considered with meniscal transplantation. The anterior horn of the MM has the largest insertion area and the posterior horn of the Lateral Meniscus (LM) the smallest. The LM has an almost circular shape. It covers a greater part of the tibial articular surface than does the MM.

The menisci are fundamental in many aspects of the knee functionality, including load sharing, shock absorption, passive stabilization, reduction in joint contact stresses, increasing contact area, restriction of extremes flexion

and extension. The MM and LM transfer respectively around 50% and 70% of the total load when the knee is extended. The improved joint congruity, which happens through the contact of the meniscus, is believed to play a role in joint lubrication and cell nutrition. In the study of Voloshin and Wosh [10] it was found a reduction of the shock absorption capacity of the knee equal to 20% after meniscectomy. As the meniscus play a fundamental role, the understanding of their function, biology and healing capacity is essential to allow proper decisions in clinical setting. [11].

The anterior cruciate ligament (ACL) and posterior cruciate ligament (PCL) are located at the centre of the human knee joint, precisely in the *intercondylar fossa*. Standing their anatomical location, both these ligaments allow for a composite functional interaction, offering rotational and translational stability to the joint. The ACL fibres are subjected to non-isometric length changes throughout the motion of the knee joint, offering varying degrees of restraint to anterior tibial translation, which represents the main ACL task. The primary function of the PCL is to limit posterior tibial translation. In different studies [12], [13] it was demonstrated that the isolated cutting of the PCL gained small increases in posterior tibial drawer near extension, but resulted in a much greater posterior instability toward flexion.

All the other parts of the knee are shielded by a thin covering called synovial membrane. This membrane releases a liquid (synovial) which lubricates the cartilage reducing the frictional forces.

I.2.2 Range of Motion of the Knee

The knee transmits loads, contributes in movements, helps in momentum conservation and offers a force couple for all the activities engaging the leg. The knee holds up high loads and moments and is located between the body's two longest lever arms – the femur and the tibia – making it exceptionally vulnerable to injuries. Even though knee motion occurs simultaneously in three anatomical planes, the motion in one of them is so great that it accounts for almost all the motion. Moreover, although many muscles produce loads on the knee, at any time one muscle group prevails, realizing a force so high that it accounts for most of the muscle force acting on the knee. Thus, simple biomechanical analyses can be realized by considering motion in one plane and only the force realized by a single muscle group but still obtaining an understanding of knee motion and a good approximation of the amplitude of the principal forces and moments acting on the joint. Advanced biomechanical dynamic study on the knee joint, involving all soft tissue elements are complicated and still object of investigation.

Joint motion can be described by rotation and translation about three orthogonal axes. In the knee joint here are three possible rotation (see **Figure I.7**):

- Flexion/Extension;

- Varus/Valgus;
- Internal/External.

In addition, there are three possible translation:

- Medial/Lateral;
- Antero/Posterior;
- Proximo/Distal.

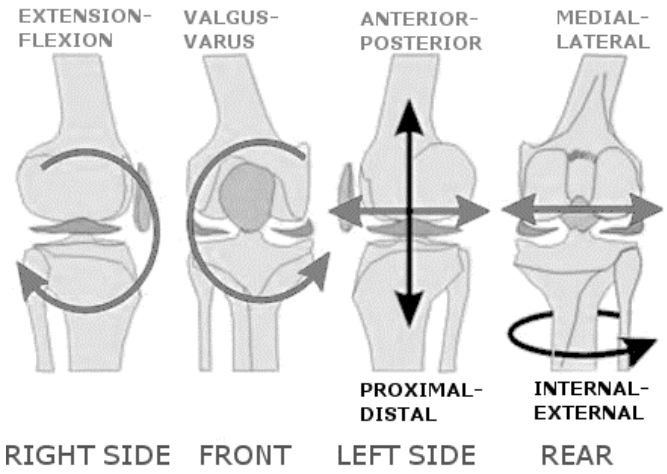

Figure I.7: *Knee joint range of motion.*

I.2.3 The knee joint diseases

The most common disease affecting the knee joint, causing pain and reducing mobility, is the arthritis. By the way, there are different kind of arthritis, the ones that causes more disability are: chronic senile osteoarthritis, rheumatoid arthritis and post-traumatic arthritis.

- **Osteoarthritis** was already described in **section I.1.3**, as it can affect joints as well as the hip. It is also common known as "wear and tear". It commonly affects people older than 50 years but can also upsets younger people. The cartilage, that normally dampens the bone contacts, get soften and consumed. Therefore, the bones slide against each other, causing pain and rigidity to the knee.
- **Rheumatoid arthritis**, also described in **section I.1.3**, is a chronic inflammatory disorder that can affect more than just the joints. In some people, the condition also can damage a wide variety of body systems, including the skin, eyes, lungs, heart and blood vessels. In this disease, the synovial membrane that surrounds the articulation becomes thicker

and inflamed. The chronic inflaming can damage the cartilage and yielding its loss, which means pain and rigidity.

- **Post-traumatic arthritis** can follow a serious knee injury. There are many traumatic injuries that can occur in the knee, from the contusions to serious fractures involving the surface of the joint or the close shafts of tibia and femur. The bone fractures or the ligaments breaks can, as time pass, damage the joint cartilage, causing pain and limiting its function. A large number of patients who sustain tibial plateau fractures (regarding the weightbearing surface of the tibia) need a surgery of knee replacement in years after the injury.
- **Osteochondral defects / Loose bodies:** sometimes "potholes" can develop on the knee surface, visible with an arthroscopic surgery when the camera is inserted into the joint. In some occasion a plug of cartilage and underlying bone can break loose, generating a crater on the surface. This carter is painful and often leads to accelerated arthritis, but the lump of bone and cartilage can be even more harmful and damaging. This could become a loose body which moves around and causes damage, as catching and locking when it becomes caught in the knee.
- **Chondromalacia** refers to the transition phase between the normal cartilage state and the "bone on bone" arthritis in which the cartilage is gone. In this phase the cartilage is soft and starts to delaminate or peel away. It's a condition that can affect also young patients and often is the first symptom of a serious arthritis, even though it is not eminent. The surgeon can advise the patients of its status after arthroscopic surgery and, in some cases, forecast the need for a knee replacement in the next years.
- **Meniscal tears:** being the meniscus a C-shaped disc that cushions and stabilizes the joint, it protects the bones from wear and tear. But a wide twist of the knee could lead to tear the meniscus: a piece of shredded cartilage breaks loose and catches in the joint, yielding to lock it up. These tears are common in patients practicing contact sports or noncontact sports that require jumps and cuts, as they can occur when a person suddenly change it direction while running, and often happens at the same time as other damages like ACL injury.
- **Anterior cruciate ligament (ACL) injury** is the tearing of the ligament. The ACL, one of the two ligaments that cross in the middle of the knee, connects the femur to the tibia. This injury happens often during sports that requires fast change of direction or suddenly stops.

II Chapter
Arthroplasty

With the word *arthroplasty* it is described the surgical procedure to restore a joint. The joint can be renovated by resurfacing the bones or by replacing it with a prosthesis. The two most widespread arthroplasties regard hip and knee, as these articulations have the duty to sustain heavier loads and to allow balance and ambulation. In this chapter these arthroplasties will be described, the main implant typologies will be illustrated, and a last section will debate their typical failures.

II.1 Hip Arthroplasty

In a total hip replacement (also known as Total Hip Arthroplasty, THA), the injured bone and cartilage is amputated and replaced with prosthetic components. The femoral head is replaced with a component made of two parts: a stem and a head. A metal stem is placed into the hollow centre of the femur. The femoral stem may be either cemented or "press fit" into the bone. A spherical element is placed on the upper part of the stem. This ball replaces the damaged femoral head removed. The cartilage surface of the socket substituted with a metal socket. Screws or cement are usually used to hold the socket in place. A polymeric, ceramic, or metal spacer is inserted between the new ball and the socket to have a smooth counter-surface.

II.1.1 Hip Arthroplasty evolution

II.1.1.1 Firsts developments

In the past, the limitation of mobility of the hip joint – i.e. morbus coxae senilis – was considered a side effect of ageing and only affect a small percent of the populace, therefore it was not considered a treatable pathology.

However, Total Hip Arthroplasty (THA) is now a sizable method that has transformed the diagnosis for osteoarthritis victims. Because of THA, patients gained a better lifestyle, as hip osteoarthrosis is not restricting their mobility. A summary of the history of THA is briefly presented.

The earliest attempts at hip replacement took place in Germany in 1891, with consequences provided on the 10th International Medical Conference. Professor Themistocles Glück supplied using ivory to replace femoral heads of sufferers whose hip joints had been ruined by means of tuberculosis. Later, surgeons experimented with interpositional arthroplasty inside the past due 19th and early 20th century, which involved placing various tissues (fascia lata, skin, pig bladders submucosa) between articulating hip surfaces of the arthritic hip. These early attempts were characterized by poor design, inferior materials, and mechanical failure.

In 1925, the American surgeon Marius Smith-Petersen created the first mould arthroplasty out of glass. This was a hollow hemisphere that can match over the femoral head and offer a brand new clean surface for motion. Notwithstanding glass being a biocompatible fabric, it didn't withstand the large forces going through the hip joint and shattered. Marius Smith-Petersen, together with Philip Wiles, later went on to trial the present-day material of desire – stainless steel – to create the primary total hip replacement that was fixed to bone with bolts and screws.

The first to apply a metal-on-metal (MoM) prosthesis on a regular basis was the English surgeon George McKee. In 1953, he started with the modified Thompson stem (a cemented hemiarthroplasty used to restore from the fracture of the femur neck) with a new cobalt-chrome socket as acetabulum. This MoM prosthesis had a good survival rate, presenting a 28 yr survival rate of 74%. But these MoM pairs became unpopular in the mid-1970's because of nearby outcomes of metal particles seen at some point of revision surgical operation for prosthetic failure [14].

II.1.1.2 John Charnley and the polyethylene prosthesis

The orthopaedic surgeon Sir John Charnley, from the Manchester Royal Infirmary, is considered the forerunner of the modern THA. He made three major contributions to the evolution of total hip replacement: 1) the idea of low friction torque arthroplasty; 2) use of acrylic cement to fix components to living bone; and 3) introduction of high-density polyethylene as a bearing material. His *low friction arthroplasty* designed in the early 1960's is identical, in principle, to the prostheses used today. His novel design included three parts: a femoral component – initially made of stainless steel –, an acetabular component that was made of polyethylene with a very high molecular weight, and a bone cement. Furthermore, synovial fluid was utilised to lubricate the replacement joint, improving the friction reduction. For sedentary patients, an alternative design included a smaller femoral head, to minimize friction. The

whole idea of Charnley was called the *low friction arthroplasty*. In their review of the first-generation of Charnley's low friction arthroplasty, Berry and colleagues [15] and Callaghan and co-workers [16] reported 81% and 77% survivorship, respectively, at 25-year follow-up, with revision of any element as the endpoint.

II.1.1.3 Recent developments and current materials

The procedure that is used for joint replacements today has progressed from Sir John Charnley's work. In the past 20 years, the low-friction arthroplasty design has become the most widespread procedure in the world for hip replacements. Total hip, femoral and acetabular components of various materials and a multitude of designs are currently available.

Presently, within the 5th decade of contemporary THA, more than 60.000 hip arthroplasty are performed every year in Italy [17], more than 75.000 in the UK. As the amount of effective operations has improved, strategies have grown to be standardised and the typical age of people receiving hip replacements has lowered. Hence presently there are an assortment of bearing (**Table II.1**) as well as methods presently utilized to find the mixture which produces probably the fewest complications and best long-term survival.

The bearing couples can be composed of several materials combinations. To summarize, they can be divided in to main groups: hard-on-soft couples and hard-on-hard couples. However, a scheme of the present couplings is presented:

Hard on Soft

- Metal or ceramic combined with polymer

Hard on Hard

- Metal on Metal (MoM) Devices
- Ceramic on Ceramic (CoC) Devices

Table II.1: *Main advantage and disadvantage of typical prosthesis couplings*

Prosthesis	***Advantages***	***Disadvantages***
Metal-on-polyethylene	Large volume of evidence to support Predictable Lifespan Cost	Polyethylene debris leading to aseptic loosening
Metal-on-metal	Potentially longer lifespan than polyethylene Larger femoral head - therefore lower dislocation rate	Metallosis Potential carcinogenic effect of metal ions

Table II.1: *Main advantage and disadvantage of typical prosthesis couplings*

Prosthesis	***Advantages***	***Disadvantages***
Ceramic-on-ceramic	Low friction Low debris particles Inert substance	Expensive Require expert insertion to prevent early damage Can produce noise on movement

Cementing the prosthesis often failed and therefore the attention was focused in the development of cementless techniques. The task of cement is to act as a sealant rather than a glue to enhance the fit of the prosthesis. Cementless prosthesis are characterized by the presence of a dedicated coating, hydroxyapatite, that allows ingrowth of bone and thus fixation of the implant.

Cementless procedures allow for simpler planning of hip revision surgery, particularly in the younger patients, with greater preservation of bone tissue. However, better short to medium-term clinical outcomes were found for cemented over cementless techniques, with no radiological differences seen.

Lytic defects have been reported with each steady as well as loose uncemented prostheses. In the late 1970s, many researchers, e.g. Willert [18], made decisive contributions to knowledge regarding the job of particles produced by joint prostheses in the pathogenesis of aseptic loosening and osteolysis. Additional histological assessment of tissue from the defects suggested that osteolysis was connected to the macrophage reaction to polyethylene debris [19]. Fragments from polyethylene wear, rather compared to cement particles, were then recognised as the main limitation to traditional full hip arthroplasty.

Polyethylene wear and debris formation lead to prosthesis loosening, osteolysis, joint instability, and synovitis. Replacement bearing surfaces, for example metal on cross linked polyethylene and hard-on-hard bearings (ceramic-on-ceramic or metal-on-metal) have been evaluated to minimize wear and boost longevity of THA procedures, particularly in younger, high demand patients. The launch of cross linking of Ultra High Molecular Weight Polyethylene (UHMWPE) was meant to deal with the problem of osteolysis and wear by decreasing the amount of submicron particles generated. Gamma irradiation of polyethylene yield cross linking, which considerably enhances wear resistance. Short-term clinical outcomes for cross linked UHMWPE indicate a decrease in wear as opposed to conventional polyethylene.

MoM bearing surfaces were initially used widely in the 1960s. Inadequate materials and designs with equatorial bearing coupled with inferior fixation condemned the prostheses to premature failure. It was also discovered that metal debris from wear caused metallosis, that had a theoretical carcinogenic risk, and was also associated with hypersensitivity reactions and prosthetic

loosening. These aspects led to temporarily abandon MoM prosthesis. Nevertheless, long term follow-up of implants with polar bearing showed small wear and very good survival rate without the issues related to polyethylene induced osteolysis. This discover led to a renewed interest in the in-vivo and in-vitro wear properties of MoM joints. Metal bearing surfaces have very low wear rates - about 0.004 mm per year, whereas polyethylene has 0.1 mm per year. Metal isn't brittle, unlike ceramic, thus it can be less thick than ceramic. Thus, for a certain acetabular shell size, a big head diameter may be used, which enhances joint stability and offers a big range of motion. Additionally, it realizes a faster sliding speed of the bearing, contributing to better lubrication. Though the bearings have generally a lower wear rate, there's apprehension about origination of metal ions (both cobalt and chromium), that are manifest. Although high quantities of cobalt and chromium ions could be observed in urine and blood, no long-term adverse consequences have yet been registered [20].

Initially released through the French surgeon Pierre Boutin throughout 1970, half of the hip arthroplasties in central Europe have ceramic heads, but there's a significantly lower use in the USA and UK (<10%). Chosen to deal with the troubles of friction and wear reported with other materials, the ceramic utilized in orthopaedics are made up of whether zirconia or alumina.

Alumina ceramics had been proposed in the 1970s. They have a minimal coefficient of friction, scratch resistant, lower wear rates, have no likely ion release, and the particulate debris is not biologically active (inert behaviour of debris compared to metal or PE). Nonetheless, ceramics have the chance to fracture due to their brittle nature. Furthermore, these hydrophilic materials realize better lubrication, therefore resulting in a lower friction coefficient. Hence CoC prosthesis are a good choice for young, active patients due to the reduced wear. Nevertheless, the cost of these implants is noteworthy and so are uncommonly used. Good short-term results are reported for both alumina-on-polyethylene and alumina-on-alumina bearings.

The danger of fracture in alumina ceramic bearings was confirmed in literature. Chipping of the surfaces yield the failure of this prosthesis, or dislocation – due to the little femoral heads – can easily cause third body wear.

Newly introduced ceramic-on-metal (CoM) bearings have been shown to considerably decrease the wear rate compared to MoM pairs: fewer particle production and smaller dimensions have been detected during in-vitro investigations [21], [22].

Gaining popularity in recent years, minimally invasive techniques are currently being developed. The use of a single-incision, less than 10 cm in length, provides soft-tissue sparing and bone conservation options. Studies have demonstrated that it gives the possibility of reduced intra-operative blood loss, shorter hospital stay, faster while not increasing complication rates or physical function post-op.

II.1.2 Composite Biomaterials

In this section it will be reviewed the evolution and the current state of the art of ceramics composites and polymers commonly used in orthopaedic field as hip joint implants. This section is extracted from the article "*Advanced biomaterials in hip joint arthroplasty. A review on polymer and ceramics composites as alternative bearings*" published on the journal Composites Part B: Engineering 83 in 2015 (pages 276-283), authors: Saverio Affatato, Alessandro Ruggiero and Massimiliano Merola.

II.1.2.1 Introduction

A biomaterial is a material that interacts with human tissue and body fluids to treat, improve, or replace anatomical elements of the human body. Clinical results in orthopaedics have demonstrated that a great need exists to find new and better biomaterials that would help to satisfy the minimum requirements for orthopaedic devices to perform correctly on a long-term basis [23].

A composite material can be defined as a combination of two or more materials that results in better properties than those of the individual components used alone. In contrast to metallic alloys, each component of the composite material retains its separate chemical, physical, and mechanical properties. In the usual bi-components composites, one material is present in a continuous or discontinuous form (such as filament or particles) and is called reinforcement, the other material is always present in a continuous phase and is called matrix. The latter gives the shape to the final element and transfers part of the mechanical loads to the reinforcement. The main advantages of composite materials are their high specific strength and stiffness, combined with low density, when compared with bulk materials, allowing for a weight reduction in the finished part [24]. Moreover composite materials allow a flexible design so that their properties can be tailored to specific applications such as lower friction coefficient and enhanced wear resistance [25], [26].

II.1.2.2 Bioceramics composites

Ceramics are non-metallic inorganic materials with a broad range of composition. Kingery [27] gave a definition of ceramics as: "the art and science of making and using solid articles which have as their essential component, and are composed in large part of, inorganic non-metallic materials". They are usually processed by mixing particles of the material together with water and an organic binder [28]. The mixture is then moulded to obtain the desired shape, dried to evaporate the water and the binder burned out by thermal treatment. The final microstructure of the ceramic is greatly dependent on the thermal process applied, the maximal temperature reached and the duration of the thermal steps. Ceramics used in orthopaedic surgery are classified as bioactive or inert according to the tissue response when

implanted in an osseous environment [29]. The bioactivity of a material can be defined as its ability to bond biologically to bone. In other words, a bioactive material influences or causes a reaction in living tissue, on the contrary the inert ceramic does not stimulate such a reaction. In clinical practice, inert fully-dense ceramics are used as bearings in total joint replacements because of their exceptional resistance to wear and their tribological properties [30]. In recent years ceramic materials have been recognised as being increasingly important for their chemical and physical characteristics, and have progressively attracted interest in the field of biomedicine [31]–[33].

Ceramic materials for total hip replacement were introduced more than 20 yrs. ago; they were introduced in orthopaedics for hip implants to solve the critical problems of polyethylene wear [34], [35]. The most used ceramic in the orthopaedic field are alumina and zirconia. **Figure II.*1*** shows a representation of such ceramics used for acetabular cups. Alumina ceramics have been widely used for their thermo mechanical and tribological properties: they show a very high hardness, wear resistance and chemical stability [36], [37].

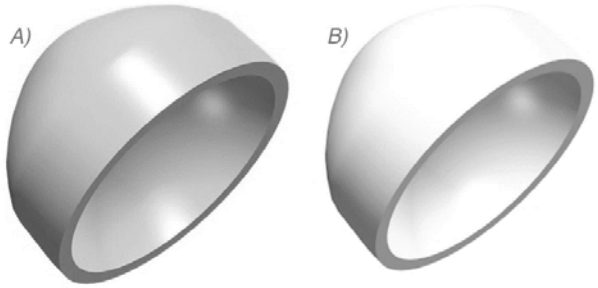

Figure II.1: *Acetabular cup in ceramic materials: a) zirconia and b) alumina.*

Zirconia ceramics have been introduced into orthopaedics as an alternative to alumina [38]. The name of the zirconium comes from the Arabic Zargon (golden in colour) which in turn comes from the two Persian words Zar (Gold) and Gun (Colour) [29]. Zirconia ceramic was introduced in the manufacture of femoral heads for total hip replacements because of its high specific strength and toughness, which would reduce the risk of fracture. Zirconia is a well-known polymorph that occurs in three forms: monoclinic (M), cubic (C) and tetragonal (T) [39]. Pure zirconia is monoclinic at room temperature. This phase is stable up to 1170°C. Above this temperature it transforms into tetragonal and then into cubic phase at 2370°C. During cooling, a T – M transformation takes place in a temperature range of about 100°C below 1070°C. A detailed phase diagram of the material transformation is shown in **Figure II.*2***. The phase transformation-taking place while cooling is associated with a volume expansion of approximately 3-4% [29] and a

significant decrease of the mechanical properties due to the production of cracks [30], [40]. Stresses generated by the expansion originate cracks in pure zirconia ceramics that, after sintering in the range 1500-1700°C, break into pieces at room temperature. The idea to combine the tribological properties of alumina and the mechanical characteristics of yttrium-stabilised zirconia allows to obtain a new class of ceramic material with improved tribological and mechanical characteristics of cubic zirconia as the major phase, with monoclinic and tetragonal zirconia precipitates as the minor phase [29]. The process of phase transformation is in any case a crucial point during manufacturing. In 2001, in fact, the Food and Drug Administration (FDA) and the Australian Therapeutic Goods Administration (TGA) recalled a series of Yttria Tetragonal Zirconia Polycrystal (Y-TZP) hip prostheses due to a rupture risk [41]. The producer ascribed the issue to an accelerated $T-M$ transformation, which generated severe micro-cracking.

The introduction of zirconia up to 25% wt into an alumina matrix results in a class of ceramic materials with increased toughness, known as Zirconia Toughened Alumina (ZTA) [42]. Alumina-Matrix Composites (AMC) had been developed to obtain a ceramic in which the biocompatibility and stability of alumina would be joined to enhanced toughness and mechanical properties [43], [44]. In the 2000s the first ZTA material introduced in clinic was a

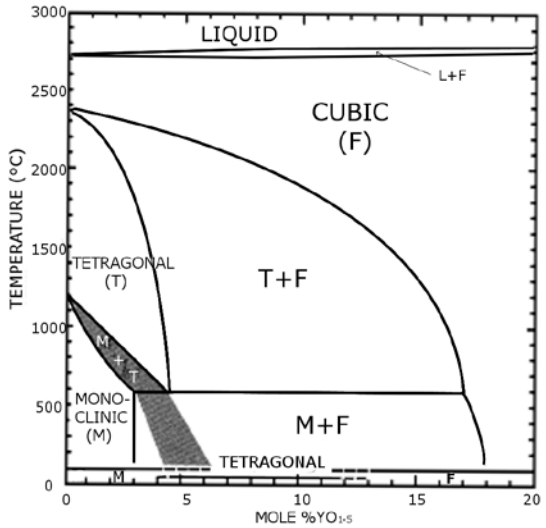

Figure II.2: *The phase diagram of the zirconia transformation.*

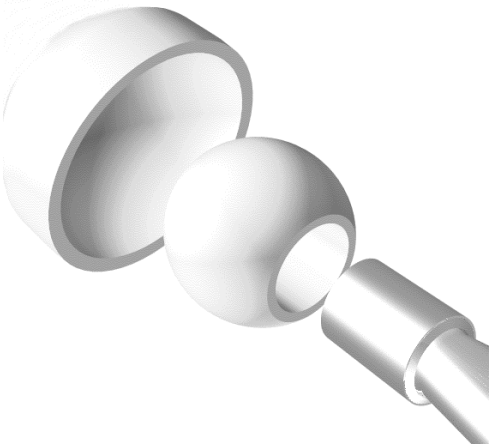

Figure II.3: *Representation of a Biolox (r) Delta hip implant pairs.*

composite known under the trade name of BIOLOX® delta [45]. BIOLOX® delta (a representation is showed in **Figure II.*3***) is obtained by chemical-physical reactions in which at the first time is increased the hardness and the stiffness of the alumina matrix. The second reaction leads to increased hardness, strength, fracture toughness, and reliability of the ceramic, due to the formation of platelets. Finally, the third reaction leads to high fracture toughness, strength and reliability, by the formation of submicron-size Y-TZP grains finely and evenly dispersed within the alumina matrix [46]. It was shown by Deville et al. [47] that Alumina Y-TZP composites can exhibit significant ageing. Even if in his tests the ageing process was much slower than usually observed for Y–TZP ceramics, and this is attributable to the

presence of the alumina as matrix component. Significant transformation level can be observed at the beginning of these ageing experiments [47]. The presence of Zirconia aggregates was identified as the main issue leading to ageing sensitivity [48]. Operating an optimal dispersion at acid pH can avoid the Zirconia aggregates formation, but when the percolation threshold level (16 vol.%) is exceeded ageing cannot be avoided. The alumina matrix composites showed enhanced wear resistance when compared to bulk alumina [49].

Hydroxyapatite ($Ca_{10}(PO_4)_6(OH)_2$), a natural calcium phosphate, builds the mineral component of the bones. Artificial hydroxyapatite forms strong bonds with hard tissues inside the body, thus is considered as bioactive, it has therefore reached considerable attention as orthopaedic implants material. Due to its low strength and fracture toughness, artificial hydroxyapatite is used only in low stress implants. Using this material to reinforce ceramic and metallic matrix make possible to apply it as loaded bearing. Nevertheless, the deleterious reaction that takes place between matrix and reinforcement inhibit the diffusion of these composites [50], avoiding this reaction requires an accurate procedure such as a super-fast consolidation technique [51].

Attempts to obtain an alumina ceramic composite reinforced with Carbon Nanotubes (CNT) with high wear resistance are subject of many researches [52], [53]. However, many difficulties are encountered or found to disperse the CNT inside the ceramic matrix due to an agglomeration effect. A possible solution to these unwanted results is the use of in situ synthesis of CNTs within the oxide powder. An alternative solution consists in an in-situ synthesization of ZrO_2 nanoparticles on the surfaces of CNTs and subsequent application to the alumina ceramics [54].

II.1.2.3 Polymers composites

Many polymers are widely used in various applications. This is mainly because they are available in a wide variety of compositions, properties, and forms, and can be fabricated readily into complex shapes and structures [55]. An effort to minimize friction and eliminate metallic wear on particles of the Co-Cr alloy implants led Charnley, in the early 1960s, to use polymers for the acetabular component [56]. He was the first that implanted the stainless steel femoral component with a mating acetabular component made of Polytetrafluoroethylene (PTFE). The PTFE has a high thermal stability; it is hydrophobic, stable in most types of chemical environments, and generally considered to be inert in the body [57]. It does not adhere to other materials and has the lowest coefficient of friction of all solids. However, clinical studies involving PTFE acetabular cups in the total hip replacement prostheses showed unacceptably high wear and distortion [58]. The wear debris resulted in extensive tissue reaction and even formation of granuloma. This elevate particles formation is attributed to its low compressive stiffness and strength,

and increased wear under high stresses during sliding. PTFE is no longer used in such load bearing applications. Subsequently acetabular cups made of Ultra High Molecular Weight Polyethylene (UHMWPE), introduced first by Charnley in November 1962, were developed and found to be successful. UHMWPE is made up of extremely long chains of polyethylene and each individual molecule adds strength to the whole structure through its length. UHMWPE is produced as a powder, which must be compacted in solid form in order to obtain the final shape, by the chemical process of polymerization, which involves usually Ziegler catalysts as titanium tetrachloride [59], [60]. Once the polymerization is completed, the UHMWPE powder needs to be consolidated into a sheet, rod or neat shaped insert. In few cases, the powder is merged directly in its final implant form, using the direct compression moulding process, without needs of further machining. Alterations during these manufacturing processes could lead to differences in physical and mechanical behaviour of the final element. Machining of UHMWPE implants consists in milling and turning operation for both roughing and finishing steps [61]. Changes to the surface roughness of the implants can affect the initial wear rate due to removal of machining marks, which will occur within the contact zone during the first stages of wear [62]. It is well known that the debris generated from the UHMWPE socket may cause adverse tissue biological reactions leading to bone loss or osteolysis. A major consequence of the debris-induced osteolysis is the loosening of the implant inside the femur or acetabular cup, which often necessitates a revision surgery.

The need for an improvement of the UHMWPE has gained considerable interest by the scientific community. Radiation crosslinking combined with thermal treatment arose in late 1990s as a technology to improve the wear and oxidation resistance of UHMWPE implants [63], [64]. The expansion of this technology during the past decade led to a series of alternative UHMWPE treatments, including irradiation and melting, irradiation and annealing, sequential irradiation with annealing, irradiation followed by mechanical deformation, and irradiation and stabilization with vitamin E. Currently, scientists have proposed alternate varieties of UHMWPE to improve the wear resistance of the polymer: the cross-linked polyethylene. This type of polyethylene, commonly abbreviated as PEX or XLPE, is a form of polyethylene with cross-links. Cross-linking represents the most exciting potential advantage in articular technology, since in this process polyethylene molecules are bonded together to result in a stronger material, of improved wear resistance. Covalent bonds are formed between the polymeric chains and therefore chain mobility, orientation, and as a result wear, are inhibited. Crosslinking can be reached by subjecting the polymer to ionizing radiation or by peroxide or silane chemistries. Silane crosslinking received limited attention and few applications [65], peroxide crosslinking reported increment of wear resistance but resulted in an oxidatively unstable material [66]. Cross-linking has been reported to improve the wear characteristics with respect to

non-cross-linked PE in clinical studies and laboratory tests [59], [67]. By inducing carbon-carbon covalent bonds between the molecules, crosslinking inhibits chain slippage and makes the PE more resistant to being tense and producing fibrils particles. The molecules of standard polyethylene are oriented parallel to the sliding direction during one part of the walking. In regular polyethylene, chains molecules may become oriented parallel to the applied stresses, yielding the material weaker in the transverse direction [68]. Therefore, during one part of the walking cycle, the crystalline lamellae, near the surface, acquire a preferred orientation, becoming more vulnerable to fracture in a crossing direction during another moment of the gait [69]. However, the reduction in the mechanical properties of polyethylene under certain methods used to produce cross-linking has been a concern. Radiation crosslinking decreases chain mobility and chain stretch; therefore, it reduces the ductility of the polymer. This entails a reduction in the elongation at break, toughness, and fatigue crack propagation resistance of the polymer [61]. These reductions could affect the device performance *in-vivo* [70]. Free radicals may take place in the manufacturing process, potentially allowing for oxidative changes in the XLPE. The ideal XLPE would be cross-linked at a correct level of radiation, and then re-melted to remove these free radicals [71].

To improve the creep resistance, stiffness and strength, and to increase long-term performance of UHMWPE acetabular cups, reinforcement as Carbon fibres (CF) has been added in the polymeric matrix [72]–[74]. For example, fibres reinforced UHMWPE has superior creep and fatigue resistance than the unreinforced UHMWPE [55]. Initial studies on carbon-UHMWPE encouraged the development of these materials for implants, legitimated by good results in terms of wear resistance, creep strain, stiffness and withstanding of compressive loads [75], [76]. Opposing evidences were found in other studies, indicating a drop in the long-term wear resistance [77], poor interfacial fibre-matrix bond strength [78] and greater fatigue crack progression rate [79]. The main concern with these implants is their release of carbon debris into the proximate tissues. It has been proved that they can provoke adverse cell response, such as collagenase synthesis [80], cell detachment and lysis [81]. Therefore, the use of these materials should be kept under inquiry unless carbon debris release is certainly avoided. The use of these composite materials in THR components has been limited, by the mechanical property mismatch between these composites and the femur bone. The idea is to develop a high strength reinforced polymeric matrix such as self-reinforced UHMWPE- or Polyether Ether Ketone (PEEK) reinforced with CF [74]. The self-reinforced UHMWPE is essentially a non-oriented matrix of UHMWPE in which reinforcement has been dispersed. The resulting polymer offers an excellent biocompatibility, increased mechanical properties and the possibility to be sterilized and cross-linked exactly as the conventional UHMWPE [74]. CF-reinforced PEEK has been proposed as an alternative for UHMWPE and it has been studied with great interest although is not currently

used in clinical practice for total hip replacement [82]–[84]. A picture of such peek is showed in **Figure II.4**. Reaching new forms of composite UHMWPE is a common aim for the scientific community. Nowadays among this class of materials we can mention UHMWPE composites reinforced with CF, polymethyl methacrylate (PMMA), nano-sized hydroxyapatite (HA) particles; nano-Al_2O_3/UHMWPE composites; UHMWPE composites filled with wollastonite fibre, nano-powder of SiO_2 fibre [85]. Even if many of these composites led to an improvement of some mechanical properties, there is still

Figure II.4: *Representation of a polymer PEEK used for acetabular cups.*

no consensus about the *in vivo* performance of these materials.

Surely, the discovery of polymer nano-composites has opened a new dimension in the field of materials science. Nano-sized wear particles are known to be highly inflammatory, leading to osteolysis, and can migrate everywhere in the body with potentially harmful effects. Therefore, introducing nanoparticles in the orthopaedic field require extensive *in-vivo* studies to predict possible long-term effects [86]. Johnson et al. [87] investigated the mechanical and wear behaviour of high density polyethylene (HDPE) reinforced with CNT evidencing that the addition of a few percentage of nanotubes positively affects stiffness, maximum load tolerance and wear resistance. The influence of CNTs in UHMWPE on wear resistance is reported to be positive. Wear factor, wear loss, or depth wear decreases between 20% and 80% with respect to standard UHMWPE [88], depending on the various test configurations and CNT concentrations, with the general trend that the wear resistance was improved as the filler content increased. Another issue relate to the carbon nano fibre reinforced UHMWPE is the fillers distribution: due to high viscosity of the polymer, this operation is generally limited to dry-mixing before compression moulding, which leads to an unpredictable dispersion. Efforts to limit this inconvenient are made by adding paraffin oil to UHMWPE powders and carbon particles prior to melt-mixing [89], which has also a positive effect on the friction and wear of the resulting composite. However, the mass production of these based functional composite materials is very difficult. Nicholas A. Kotov wrote in his review in Nature [90]: “When carbon fibres just won’t do, but nanotubes are too expensive, where can a cost-conscious materials scientist go to find a practical conductive composite? The answer could lie with graphene sheets”. Graphene is considered a two-

dimensional carbon nanofiller with a one-atom-thick planar sheet of sp^2 bonded carbon atoms that are densely packed in a honeycomb crystal lattice [91]. It is regarded as the "thinnest material in the universe" with tremendous application potential [92], [93]. Graphene is predicted to have remarkable properties, such as high thermal conductivity, superior mechanical properties and excellent electronic transport properties [94], [95], that make it suitable for thermally and electrically conducting reinforced nano-composites, electronic circuits, sensors, and transparent and flexible electrodes for displays and solar cells etc. [96]. The discovery of graphene as a nanofiller has opened a new dimension for the production of light weight, low cost, and high performance composite materials for a range of applications [97]. Addition of Graphene Oxide to UHMWPE gave evidences of good interaction and improvement of the wettability as well as enhancement of mechanical, thermal and structural properties compared to the virgin UHMWPE [98]. Besides the mechanical aspect, there are several evidences of good biocompatibility of the graphene oxide itself [99], [100] and the graphene oxide reinforced UHMWPE [101]. Tests made on UHMWPE reinforced with GO exhibited contrasting results on the increase or decrease of the friction coefficient in respect to the bulk resin. The main tribological advantage seems to be a satisfying increase of the wear resistance, as reported in [102], which registered an increment of this property equal to more than four times the virgin UHMWPE.

Another material investigated for orthopaedic implants is carbon-carbon composite. Interest in this material is recorded since 1977,when Jenkins [103] found good biocompatibility by inserting a rod of CF reinforced carbon into soft living tissue of sheep and rabbits. Furthermore, its mechanical characteristics are close to the one of the human bone, and the elastic modulus is almost the same, avoiding the "stress shielding" effect and therefore the bone absorption caused by implant materials with high elastic modulus [104]. The low diffusion of this implant composite is due to the poor bioactivity, attempt to improve this aspect are made by combining it with a substrate of hydroxyapatite or bioactive calcium phosphate [104], [105].

II.1.3 Interpositional arthroplasty

Interpositional arthroplasty was introduced in 1840 by J. M. Carnochan for using in situations of temporomandibolar articulation stiffness. It entailed remodelling the articular surfaces and interposing material to confirm articular stability. In 1860 Aristide Verneuil developed the method by using biological tissues as the interposition material rather than wood. In 1883 Louis Ollier reintroduced interpositional arthroplasty for using in the therapy of hip pathologies. Ollier's efforts paved the way for further experiments, in which surgeons tried various interposition materials.

II.1.4 Hip resurfacing replacement

In addition to the THA, it exists a less invasive alternative, which is the resurfacing technique. In this technique, the bearing couple of the total replacement implant is unvaried, even if it has larger dimensions. The process consists of positioning a cobalt-chrome cup, which is hollow and shaped like a mushroom, on the head of the femur whereas a corresponding metal cup is placed in the acetabulum (pelvis socket). This procedure replaces the articulating surfaces of the patient's hip joint and takes out very little bone if compared to a THR. It also has limited chance of dislocation as consequences of its larger femoral head, and an easier revision surgery as the surgeon has more original bone stock available, it would be even possible to realize a THR if required. The main drawbacks are aseptic loosening and femoral neck fractures

II.2 Knee Joint Arthroplasty

If the knee joint is irremediably damaged because of the arthrosis or one of the several possible traumas, it could be hard to perform even the easiest activities, as walking or climbing stairs. When the non-surgical treatments, as painkillers, infiltrations or physiotherapy, became ineffective it is possible to consider the surgery. The knee arthroplasty is an efficient and relatively safe procedure to alleviate pain, restore mobility and correct legs deformity. The first knee arthroplasty was realized in 1968. Since then, the progress in term of biomaterial and surgery techniques have strongly increased its efficacy. The total knee replacement is one of the most successful surgery of all time, the Agency for Healthcare Research and Quality in USA claims that every year this procedure is don on more than 600k patients. In Italy, between 2001 and 2005 the number of patients which underwent the TKR raised from 26793 to 44119, these data are going to increase since the average population age is growing and the life expectancy is raising.

The joint surgery consists in the resection of the deformed articular components and their replacement with artificial coatings. This coating consists of different metallic alloys coupled with a different material – mainly plastic, but in few cases ceramic – that combined gain a low coefficient of friction.

The metal components are fastened to the bone, this operation can take place using a special resin (acrylic cement surgery) or by a simple forcing that will allow a consequent anchoring. In the first case the implant is known as cemented prosthesis, in the second is non-cemented one.

The implant is made of a femoral component and a metal tibial component obtained by a metallic support plate and a polymer insert that acts as meniscus (see **Figure II.5**). The insert has the duty of allowing movement of sliding and rolling. When in use, the patellar component is made of polyethylene anchored

to a metal surface. There are two mains types of knee implants, depending on whether the disease involves the whole joint or one condyle only:

- **Partial knee replacement** or **Unicompartmental**: reconstructs only the articular portion damaged, medial or lateral (see **Figure II.6** from [106]);

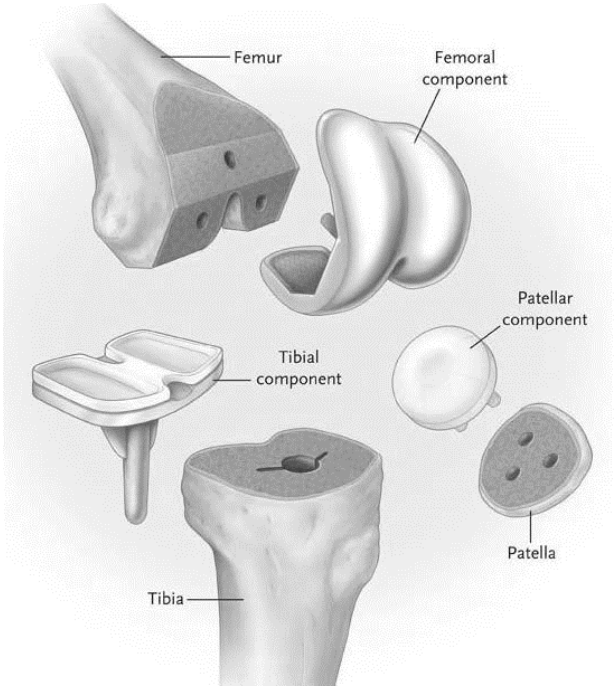

Figure II.5: *Components of a knee replacement and their fixation points on the living bones.*

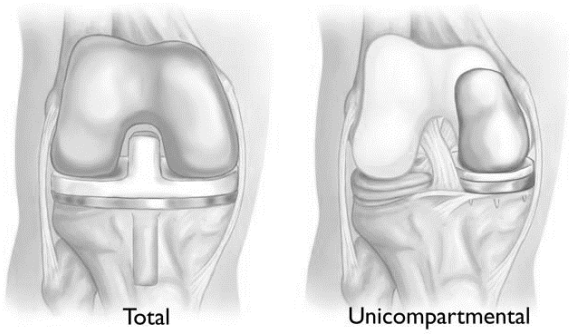

Figure II.6: *Total and Unicompartmental knee replacements.*

- **Total knee replacement** or **Tricompartmental**: reconstructs all the articular components (eventually the patellar component).

The prosthetic models among which the surgeon can carry out a choice are various. Usually, the choice is driven primarily by the experience of the

surgeon, the patient's joint anatomy and the problem encountered. The total knee arthroplasty can be divided into four categories that follow.

- Prosthesis with preservation of the posterior cruciate ligament: are appropriate for patients with a limited arthritis damage and with an intact cruciate ligament (see **Figure II.*7*a**);
- Prosthesis with posterior stability: have more stability and it can also be used in joints with more advanced damage. In some cases, the posterior cruciate ligament may get damaged after surgery, making it unstable (see **Figure II.*7*b**);
- Condylar Constraint Prosthesis: present a great stability and they are used in case the patient has poor bone quality or where are found important

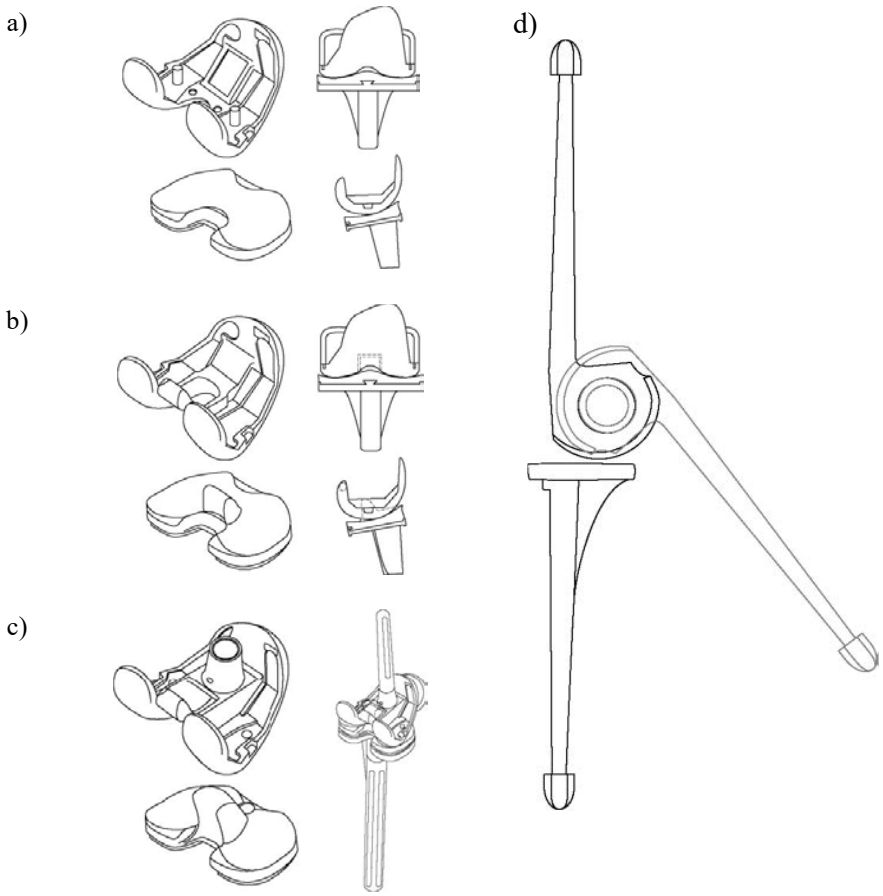

Figure II.7: *Knee prosthesis a) preservation of the posterior cruciate ligament, b) with posterior stability, c) condylar constraint, d) constrained.*

ligament injuries. They are also often used during the replanting for knee prosthesis with less bone damage (see **Figure II.7c**);

- Constrained Prosthesis: used mainly in the case of replanting or in case of severe joint instability. Present a hinge bound to longer rods intramedullary femoral and/or tibial (see **Figure II.7d**).

Moreover, the individual models may have a fixed polyethylene insert, perfectly congruent with the neo-articular surfaces, or a mobile one, to allow small rotations.

Every model is used to meet specific functional needs that vary from patient to patient. Elderly and less active patients benefit more from a total knee replacement, while younger and more active patients, often identified with this type of replacements functional deficits.

II.2.1 Biomaterial for knee joint replacement

The devices used in orthopaedic applications are designed to sustain the load bearing function of human bones for the duration of the patient's life, so the primary function of orthopaedic materials is to provide structural integrity to the human body. Structural integrity implies a combination of fracture toughness, strength, ductility, hardness, and fatigue resistance. Considering the corrosive environment of the human body, the biocompatibility and corrosion resistance are also focal requirements. Furthermore, the wear particles of the orthopaedic materials should not adversely affect the bodily environment.

II.3 Lifespan

Whereas during the early days of this procedure the target patients were mainly part of a quite old population, also characterized by moderate physical activity, the scenario changed a lot along the years. In this days, joint implants are also used to treat younger and more active people. As consequence, these implants need to be highly performing: they must cope with many years of repetitive high stresses due also to sports and excessive loading, wear and ageing effects contribute to stress out the prosthesis.

II.4 Testing

Currently, the hip joint prostheses are analysed and subjected to simulation tests before receiving the required approval for clinical use. These tests are an important phase of research and evaluation for the optimization of prosthetic materials used as well as the design of the prosthesis. These tests are performed with the aim of determine the behaviour of the prosthesis, assess the wear rate of the components and the surface finishing. However, wear tests

on a simulator are long and expensive due to the large number of cycles at low frequency that must be executed. More details are provided in **section III.6.1**.

II.5 Failures of Arthroplasty

Even if the orthoprosthesis is one of the most effective and successful surgeon in the modern medicine, around the 10% of the implanted devices will fail and will require a second surgery, called “revision”, to remove the old one and restore with new components. The revision operation is a difficult procedure which requires a long scheduling prior to surgery. The 90% of the implants will satisfy all the requirements and will be able to work fine to 10 or even 20 years in a human body. In fact, this kind of implants are mostly designated to elder persons which have a low level of activity and consequently tends to load less the joints. But, considering that more and more young patients get subjected to this surgery and old people live longer, a raising number of patients will live longer than their prosthesis. Beside this, the new biomaterials employed reach a better fixation with the bone tissues and the wear rate is modest.

The functionality of an implant is dependent on 4 important points: the supplies employed, the geometry of this prosthesis, the medical method employed as well as the psychopathological state of the surrounding cells. Unaddressed problems in any of these areas are able to lead to embed failure. The employment of biocompatible substances, which display excellent manual resistance, together with an exact medical strategy as well as the ideal option of prosthesis sort, are crucial demands for implant success. In addition to problems like septicaemia, implant failure may be related to structural issues such as corrosion, fatigue fracture, or wear, or maybe physiological phenomena resulting in mobilization of a single or maybe both prosthesis pieces.

Duration of the implant is driven by an intricate interaction between two entities: the bone, that is an intricate framework in constant evolution, and the prosthesis, whose physical system is under continuous strain from a chemic environment as well as the loading situations characterizing regular exercise. The choice of the best fixation method for the affected person can play a vital role in the lifetime of the implant.

There are several reasons for an implant failure, most of these are exposed in the following subsections.

II.5.1 Loosening

As the implants require to be fixed inside the bone, its terminal parts are joined with cement or through snap-fit. Nevertheless, due to the friction between these elements and the continuous rubbing one against another there is still production of wear particles. These debris collect nearby the

articulation. In a process called aseptic loosening, or non-infected mobilization, the body destroys the links between implant and bones in its trying to digest the wear debris. Because of this the implants became loosen, and the patient can feel pain or instability. Also, during this process, the body digest also part of the bone (phenomenon known as *lisi*). This can weaken or even fracture the bone and compromise the success of a revision operation. The aseptic loosening is one of the most frequent cause of joint implants failure.

II.5.2 Infection

The infection is another cause of failure of an implant. These big implants extraneous to the human organism made of metal or resin can act as base for bacteria where get attached and multiply. Furthermore, the tissue that covers the prosthesis and was damaged during the orthoprosthesis, will have an altered blood flux, which could be not enough to fight the infections. In these cases, the pain and the swelling will often make necessary a revision of the implant. Also, if the infection is not nursed it can weaken the patient even to the point of risking its life. The risk of getting an infection due to these kind of surgery is around 0.5%.

II.5.3 Luxation

The luxation is an unexpected migration of the prosthesis from its natural position. It is a typical problem for the hip implants, which affects one patient on 50. Some of these patients incurred in more luxation and therefor require a further surgery revision. The luxation can be consequence of the loosening, of the inadequate moving tissues, of a conflict scarring, of bad positioning of the prosthetic elements, of neurological problems (as Parkinson), or of non-conforming movements.

II.5.4 Patient's related factors

The younger and more active patients have a higher probability to be subjected to a revision surgery. The obese patients have a higher incidence of wear and loosening of the implant. The patients which have their primary operation due to the Rheumatoid Arthritis and the patients with vascular necrosis are more frequently subjected to loosening or luxation. All these conditions could lead to the revision surgery.

II.6 Diagnosis

To diagnose the failure of an implant there are different ways of investigation. The first ones are the patients' symptoms, who can feel pain or

have an unnatural walking behaviour. In second place, it could be performed an X-ray investigation. A plain radiograph could detect a different position of the implant if compared to an older radiograph, or it can show a radiolucent line between the implant and the cement or the bone, which means that the joint is degraded. X-ray can also highlight bone loss or *lisi*. Other ways of investigation are: a complete blood count (CBC), erythrocyte sedimentation rate (ESR) or a c-reactive protein (CRP) test. These analyses are useful to detect the presence of an infection. Furthermore, the synovial liquid can be extracted and analysed looking for an infection.

II.7 The Metal Transfer phenomenon

Examination of worn articulations is of primary importance to understand the damage that occurs in *in vitro* and to compare them in order to achieve a better knowledge about the wear phenomenon [107]. Unfortunately, potential complications exist using composite ceramics with possible cause of accelerated wear phenomena [108]. This can lead to the contact between the femoral head and the superolateral rim of the acetabular cup on heel strike (contact edge), thus resulting in stripe wear of the head and having significant repercussions on the wear and biomechanics of the implant, as suggested by international scientific literature [109]–[111].

An important feature of retrieved ceramic hip prostheses is the metal transfer (MT) on the femoral heads and/or on the acetabular cups, which implies an important alteration of the bearing surface. MT has been observed on revised total hip replacements as dark and metallic in colour [112]. Metallic transfer to ceramic can occur during intraoperative reduction of total hip arthroplasty (THA, i.e. if the alumina head contacts the acetabular rim) or after surgery [113]. It has been hypothesized that MT on the femoral head is associated with joint instability and subluxation/dislocation [114], [115]. Müller and co-workers [116] found that these deposits can also occur in primary THA, if there are any intraoperative difficulties in reduction or if multiple dislocation/relocation manoeuvres are needed during surgery. Chong et al. [117] also reported that the mechanisms of MT may be due to femoral head dislocation, closed reduction procedures, impingement, or third body entrapment in the articulating zone. MT markings may consist of titanium (Ti) or cobalt chromium (CoCr) alloy [118]. The presence of transferred metal on ceramic heads changes the surface properties and thus affects lubrication, friction and wear. Surface texture has, in fact, a large influence on the lubrication mechanism between two surfaces. The study of surface roughness effect in lubrication gained attention since the stochastic studies of Tzeng and Saibel [119]. Patir and Cheng [120], [121] proposed an alternative model to stochastic method, the process is based on flow factors that mainly depend on the roughness standard deviation and on the main orientation of contact areas. For textured surfaces, micro dimples can be considered as micro converging

wedges, so that a plurality of dimples could act as a set of micro bearings [122]. It has also been hypothesized that the presence of metal transfer plays a role in Ceramic-On-Ceramic squeaking [123], [124]. A correlation between this phenomenon and the squeaking was also hypothesized, as metal transfer can be the primary mode leading to fluid lubrication disruption [125].

Little is known about the morphology of MT on femoral heads. Fredette et al. [126] proposed a morphology classification of the metal tracks on the bearing surface of CoCr and ceramic femoral heads. The categorization of tracks was based on shape and orientation, they found mainly random patches and stripes for the CoCr-on-polyethylene and ceramic-on-polyethylene cohorts, and predominantly longitudinal stripes for the ceramic-on-ceramic cohort. Friction and wear of a generic bearing are strongly related to the surface characteristics of the involved materials. Primarily, the roughness of the surfaces, in direct contact or partially separated by a lubricant, affects the joint performance. Furthermore, to understand the lubrication mechanism in the bearing couple, it is necessary to combine the information of the minimum film thickness with the values of surface roughness. From this association it is possible to estimate the dimensionless parameter λ, which is an indicator of the lubrication regime: boundary, mixed or hydrodynamic [21]. Therefore, a great concern was dedicated to the analysis of the surface roughness parameters that can best reveal the tribological behaviour of bearings.

Further analysis on the tribological implication of the metal transfer will be presented in **sections III.8** and **III.9**.

III Chapter
Biotribology

In this chapter they will be depicted the main aspects to which tribology – and therefore biotribology – is based on. As this branch of engineering and physics regards friction, roughness, lubrication and wear. In the last sections of the chapter space will be given to some experimental analyses carried out during the PhD work, and that leaded to the three published articles exposed.

III.1 Introduction

Biotribology is a specific area of tribology, the science and technology of interacting surfaces in relative motion. Biotribology focuses on the tribological phenomena happening in biological system. Human beings, as well as animals, have a lot of interacting surfaces which can be also in relative motion, where friction and wear are of crucial importance.

When two bodies are in contact whit each other, they exchange a force one on the other which is responsible for the transmission of energy between the organs themselves during the motion. Tribology studies these interactions gathering together different disciplines as surfaces physic, lubricant chemistry, lubrication, viscoelasticity, thermodynamics etc. Final aim of this science is to improve the performances of the components of a machine. In other words, tribology can be defined as the science of friction, wear and lubrication applied to the surfaces in relative motion. The word tribology is based on the Greek word *tribos* (rubbing), first appeared in 1966. The literal translation would be "science of rubbing".

Tribological phenomena occur in a broad spectrum of length scales, going from common machine, instruments and tools, such as ball bearing and its race groove, cams and shafts, even to high density data storage devices, micro-machines and bio-tribological components, as synovial joints and total joint prosthesis.

Standing that the friction is the main responsible for mechanical losses – around 1/3-1/2 of the worldwide energy is lost due to friction – and that the wear defines the lifelong of a mechanism component, it is of paramount importance the understanding and correct application of the tribology principles. This importance is more evident considering that most of the damages of a machine happen in correspondence of contact surfaces between two components. Therefore, during each phase of design, implant and operation of machinery, tribology provides the tools to improve efficiency and durability.

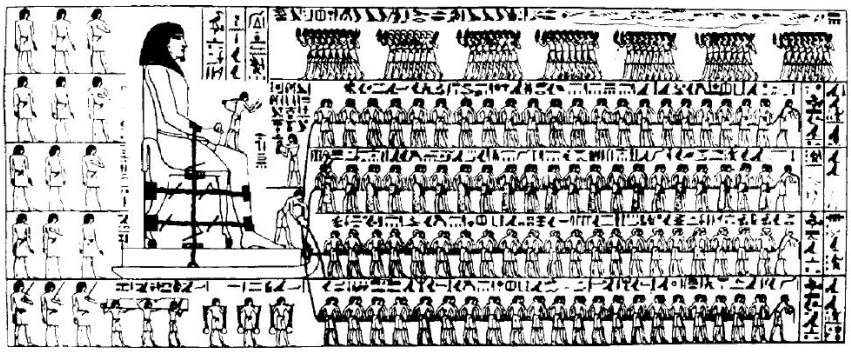

Figure III.1: *Egyptian painting showing the use of lubricant in 1880BCE*

Even in ancient times, the problem of friction was known, and our ancestors were conscious on how to reduce it. As an example: to build monuments and stone blocks they were obliged to transport heavy stones. In 3500 BCE they already knew that in order to reduce friction it was possible to use lubricants. The Egyptian painting of 1880 BCE, in **Figure III.1**, illustrates the use of sledge to transport heavy stones. The man standing on the sledge supporting the statue, can be seen pouring a liquid into the path of motion.

Tribology includes different branches that can be summarized as follows:

- study of the interaction nature that happens in the contact between mechanical components in relative motion, considering the environment where it occurs;
- study of the materials, lubricants and technological methods applied to minimize friction and wear;
- study of the lubrication mechanisms, considering the contact conditions and the working parameters (loads, velocity and temperature);
- design of mechanic units for which it is established the lifelong.

III.2 Shapes of the contact surfaces

Two solids in contact must have their surfaces cinematically conjugate in the relative motion and could lead to two types of contact, from a pure geometrically point of view: concentrated contacts and extended contacts.

In the concentrated contacts the contact area degenerate to a point (punctual contact) or to a line (linear contact). A punctual contact, for example, occurs between the spheres and the sliding track of a bearing, whereas linear contacts occur within the tooth of a gear.

It is important to underline that in a concentrated contact, due to the forces acting on the elements, the surfaces elastically deform giving back a finite contact area, which is elliptic for the punctual contact and rectangular for the linear one.

In the concentrated contact it is possible to evaluate the area of contact, through an analysis of the elastic deformation. This analysis is a problem concerning the theory of elasticity, which was mainly developed by Hertz in 1880, and is based on some hypothesis:

- the radius of curvature of the solid are well defined in the point of contact;
- the bodies are perfectly elastic, homogeneous and isotropic;
- the forces are parallel to each other and orthogonal to the plane of contact;
- the frictional forces are neglected.

The firsts three assumptions imply that $a << R$, dove a is the contact area radius and R is the effective radius of curvature of the two solids.

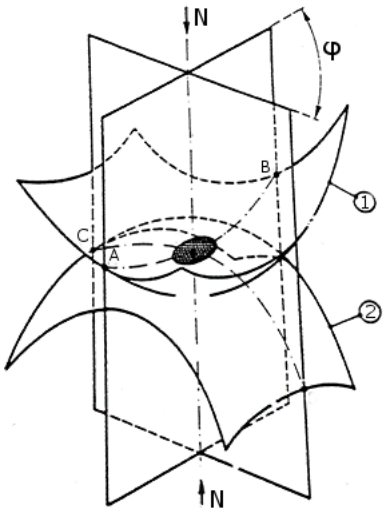

Figure III.2: *Hertzian contact.*

Considering the **Figure III.2** and called R_1, R'_1, E_1, e v_1 the radius of curvature in the contact point, the Young modulus of elasticity and the Poisson

ratio of the solid 1. Analogously, R_2, R'_2, E_2, e v_2 for the solid 2. Furthermore, called N the closure force, the contact area of the two elastically deformed bodies is an ellipse with the semi-axis, a and b, which are evaluated as follows:

$$a = m(\theta)0.908\sqrt[3]{\frac{N}{D}\frac{1}{E^*}}, \qquad (III.1)$$

$$b = n(\theta)0.908\sqrt[3]{\frac{N}{D}\frac{1}{E^*}}, \qquad (III.2)$$

where D derives from the combination of the radii of curvature of the two solids and E is the effective modulus of elasticity. They can be derived from:

$$D = \frac{1}{2}\left[\frac{1}{R_1} + \frac{1}{R'_1} + \frac{1}{R_2} + \frac{1}{R'_2}\right], \qquad (III.3)$$

$$\frac{1}{E^*} = \frac{1-\nu_1^2}{E_1} + \frac{1-\nu_2^2}{E_2}. \qquad (III.4)$$

The functions $m(\theta)$ and $n(\theta)$ of **eqs. (III.1)** and **(III.2)** are reported in **Figure III.3**, where θ is defined by the relation:

$$\theta = cos^{-1}\left(\frac{C}{D}\right), \qquad (III.5)$$

and C is:

$$C = \frac{1}{2}\sqrt{\left(\frac{1}{R_1} - \frac{1}{R'_1}\right)^2 + \left(\frac{1}{R_2} - \frac{1}{R'_2}\right)^2 + 2\left(\frac{1}{R_1} - \frac{1}{R'_1}\right)^2\left(\frac{1}{R_2} - \frac{1}{R'_2}\right)^2 cos\,2\varphi}. \qquad (III.6)$$

where φ is the angle between the planes that contain the main curvatures ($1/R_1$ and $1/R_2$) of the solids. The radius of curvature should be considered positive or negative if the corresponding centres of curvature are inside or outside the material that constitutes the bodies.

The load is distributed on the elliptic area of contact, where the Hertzian pressure varies with a semiellipsoidal law (see **Figure III.4**). The average and maximum pressure values are, respectively:

$$p_m = \frac{N}{\pi ab}, \qquad (III.7)$$

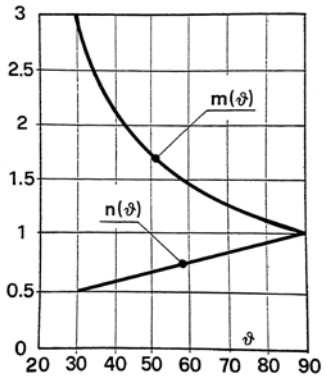

Figure III.3: *m(ϑ) and n(ϑ) functions.*

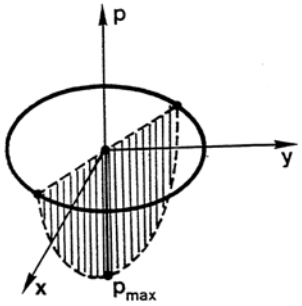

Figure III.4: *Hertzian pressure distribution.*

$$p_{max} = \frac{3}{2} p_m . \qquad (III.8)$$

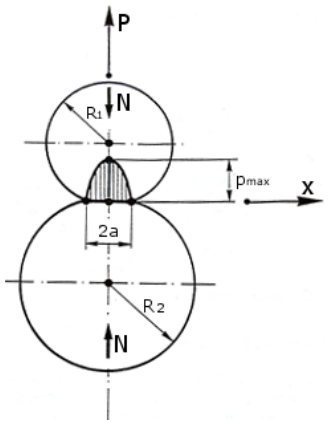

Figure III.5: *Side view of a sphere-sphere contact.*

As it will be show further (see **section III.7**), a particularly interesting application of the Hertzian theory is for the sphere–sphere contact (**Figure III.5**). Which could be easily adapted to the case sphere–plane, by considering one of the radius of curvature as infinite.

In this case the contact area is a circle, being $R_1=R_1'$ and $R_2=R_2'$, $\theta=90°$ therefore $m(\theta)=n(\theta)=1$, thus:

$$a = b = 0.908 \sqrt[3]{\left(\frac{N}{D}\right)\left(\frac{1}{E^*}\right)}. \qquad (III.9)$$

An enhancement of the Hertzian theory was obtained by Johnson et al. [127] with the JKR (Johnson, Kendall, Roberts) Theory. In the JKR-Theory the contact is assumed to be adhesive. Hence, the theory correlates the contact area to the elastic material properties plus the interfacial interaction strength. Due to the adhesive theory, contacts can arise during the unloading cycle also in the negative loading (pulling) regime. As the Hertzian theory, the JKR one is also limited to elastic sphere-sphere contacts. A more elaborate theory (the DMT theory) also considers *Van der Waals* interactions outside the elastic contact regime, which yield an additional load (see **Figure III.6**). The theory simplifies to Bradley's *Van der Waals* model if the two surfaces are not in contact and considerably apart. In Bradley's model, any elastic material deformations due to attractive interaction forces are ignored.

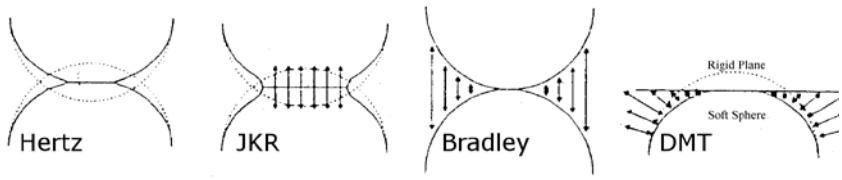

Figure III.6: *Elastic theories.*

III.3 Friction

Leonardo Da Vinci (1452-1519) was the first to systematically study friction forces. Thanks to his work, the first two laws of friction were known: the frictional resistance is proportional to load, and it is independent on the contact area of the sliding surfaces. These laws were experimentally proved by Da Vinci and later rediscovered by Amontons in 1699. Afterwards, these concepts were verified by Coulomb in 1781, who also distinguished between static and kinetic friction, being the first the force needed to start sliding and the second the one to keep sliding. The latter is usually sensibly lower than the former. Coulomb detected that kinetic friction is almost independent of the sliding speed. He declared that the friction forces were caused by the interlocking of the surfaces asperities.

The work done by frictional forces is negative, thus it causes loss of mechanical energy and a lower efficiency, and an equivalent heat generation. Actually, friction is a complex phenomenon involving multiscale factors, and it depends on the atomic interactions inside the contacts and on the macroscopic elastic and plastic deformation that influence the stress distribution within these solids.

III.3.1 Dry Friction

We speak about dry friction when a solid body, to which it is applied a normal force, moves with respect to another to which is in contact. This force, even if in many cases imply an active role in the mechanisms (e.g. breaks and clutches), in many others it implies a negative work and many undesirable and damaging effects. For this reason, it comes the necessity to reduce its action by different methods, as lubrication or a more appropriate design of material. Of course, a complete dry friction can be obtained only in theory, as the surfaces are mostly covered by substances that fill the surrounding environment. Therefore, dry friction refers to the cases where there was no intentional separation of the surfaces with other elements. On the other hand, when there is a substrate that avoids the direct contact between the surfaces, the pair is lubricated (this condition is described in **section III.5.1**).

One of the most common friction condition happens when there are two bodies sliding on each other, this case is referred to as *sliding friction.* In the sliding friction, it is possible to distinguish between two situations, depending on the force applied to the body, if it is enough or not to induce motion. When the tangential force (see **Figure III.7**) is lower than a value $|F_{app}| = \mu_s N$, than the frictional force in the interface of the bodies is equal and opposite to the f_s thus, it prevents the relative motion and the friction is known as *static friction*.

On the contrary, when the tangential force is higher than f_s there is relative motion and the friction is defined as *kinetic friction* or *dynamic friction*. As

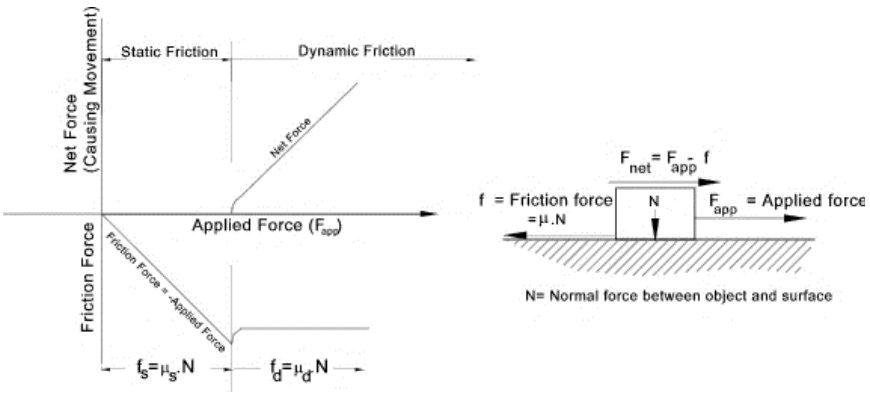

Figure III.7: *Sliding friction conditions: static and dynamic cases.*

the motion starts, the force necessary to maintain it, is equal to $f_d = \mu_d N$, generally lower than f_s. In fact, for metallic materials the static friction coefficient μ_s is higher than the dynamic one μ_d; whereas, for polymeric materials it can be the contrary.

III.4 Roughness

In any cases is very difficult to obtain really flat surfaces, even after being polished the surface will present peaks and valley on the microscale which will be bigger than the size of a molecule. If two solids are in contact, the upper surface will be sustained by the top of asperities, therefore, a great part of the area will be separated through a distance which is higher than the molecular range of action [128]. For instance, in most of the engineering problem the real area of contact between two surfaces is probably less than 1% of their nominal area [129].

Estimating the contact pressure between two bodies in contact, requires the knowledge of macro and micro features of the bodies. In the macro-scales, there are two types of contact: conforming contact and non-conforming contact. The former contact involves two bodies which surfaces fit exactly or closely together without deformation. The latter contact regards two bodies which surfaces have enough dissimilarities to gain, without load, a single point of relative contact. In other words, the contact area is small compared to the sizes of the bodies, therefore the stresses are highly focused in this area. It is possible to evaluate the pressure acting on the contact area through the Hertzian Theory (see **section III.2**).

In the meso and micro scales, the definition of the contact area changes. In fact, if observed through a magnification lens, the surface of every object is characterized by a series of peak and valleys, which constitute its roughness. This surfaces roughness reduces the contact points between the bodies, as shown in **Figure III.8**. Therefore, only some of the higher homologous peaks are in contact with each other. Because of this, the real contact area A differs

from the nominal area A_n, producing a different pressure distribution and intensity.

The **Figure III.8** represents an example of a 2-D profile, but a 3-D surface has a different statistic. It has been proved that they can be related to each other basing on a random process theory. A distinguish is necessary between a *peak* on a profile and a *summit* on a surface. The profile shows only few peaks than actually exist on the surface.

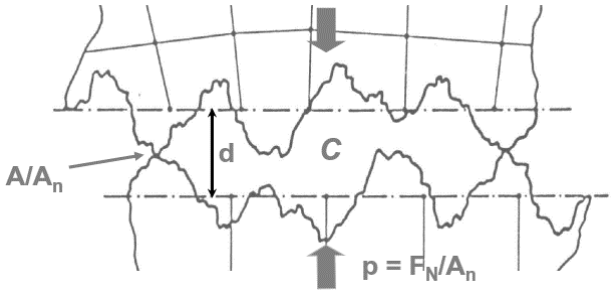

Figure III.8: *Apparent and real contact areas.*

Consider a rough surface and call *z(x,y)* the height above a plane reference, where z is a random variable and x and y are the Cartesian coordinates. Assuming that the surface is homogeneous, its statistical description is invariant with respect to translation. It is possible to define the autocorrelation function as:

$$R(x,y) = \lim_{\substack{L_1\to\infty \\ L_2\to\infty}} \frac{1}{4L_1L_2} \int_{-L_1}^{L_1} \int_{-L_2}^{L_2} z(x,y) \times z(x_1+x, y_1+y)\, dx_1\, dy_1. \qquad (III.10)$$

The Fourier Transform of R is called the Power Spectral Density (PSD):

$$\Phi(k_x, k_y) = \frac{1}{4\pi^2} \iint_{-\infty}^{\infty} R(x,y)\, e^{-i(xk_x+k_y)}\, dx\, dy, \qquad (III.11)$$

where k_x and k_y are the components of a wave-vector $\boldsymbol{k}$. The three moments of the PSD are:

$$m_n = \int_{-\infty}^{\infty} \Phi(\boldsymbol{k})\boldsymbol{k^n}\, d\boldsymbol{k} \qquad n=0,2,4 \qquad (III.12)$$

and the Root Mean Square (RMS) roughness is given by $\sigma = \sqrt{m_0}$.

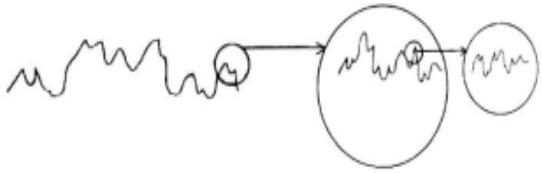

Figure III.9: *Self-affinity of rough surface.*

Surface roughness could be viewed as a fractal image, as shown in **Figure III.9**. In fact, each asperity can be further enlarged, resulting in another rough profile. This self-affinity of rough surfaces leaded to the fractal description of roughness. The asperity distribution of a real surface can be determined by the theory of Greenwood and Williamson [130]. An inverse FFT from a given spectrum generates the height field.

A first assumption to solve frictionless contact problem involving roughness, is to consider an equivalent contact problem. In practice, when the contact is between two elastic rough surfaces it is possible to reduce one of the surface to a rigid rough surface, and the other to a smooth linear elastic half-plane with modified Young's modulus (see **Figure III.10**). The modulus can be estimated through:

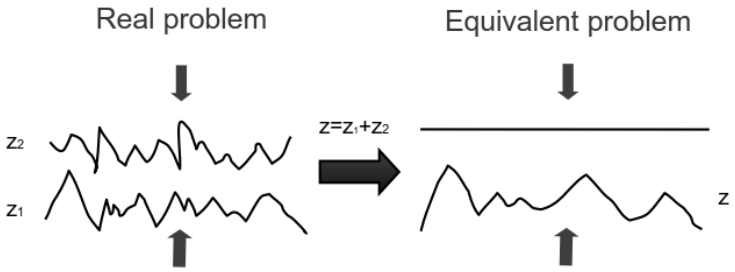

Figure III.10 *Combination of the two surfaces in an equivalent problem.*

$$E^{-1} = \frac{1-\nu_1^2}{E_1} + \frac{1-\nu_2^2}{E_2}. \qquad (III.13)$$

One way of solving the overcited problem and evaluate the load-displacement behaviour of rough surfaces, are the micromechanical contact models. These methods have the big advantage of yielding a semi-closed form solution. Furthermore, the possibility of including the elastic interaction between the asperities was introduced in the work of Ciavarella et al. [131]. Main limit is the approximate assumption of the asperities as hemispheres.

Another way of solution is Finite Element Methods (FEM), which can analyse the real shape and distribution of the asperities without any simplified assumptions. Also, the interaction between asperities is totally included. Main drawback is the expensive discretization of the surface in term of numerical computation.

Great effort has been made on study of roughness influence on hip joint contact, in term of pressure distribution and contact area, as well as the wear evolution in a rough head-cup pair. In the work of Ilinic et al. [132] a combination of FE and BE methods was applied to find the influence of roughness wavelength on the contact pressure. Finite elements were used to evaluate the pressure distribution in macroscopic scale, whereas boundary elements were applied to the rough surfaces.

The surface characteristic was created by applying the following formulae:

$$z(x,y) = \frac{A}{4}\left[1 + cos\left(\pi\varphi\left(\gamma;\frac{2x}{L}\right)\right)\right]\left[1 + cos\left(\pi\varphi\left(\gamma;\frac{2y}{L}\right)\right)\right], \qquad (III.14)$$

where A is an amplitude and φ a phase. By the variation of γ it was possible to simulate different asperities shapes, as shown in **Figure III.11**. They found that the maximum contact pressure increased with increasing of clearance (difference in head and cup radius) and decreasing roughness wavelength for all the three asperity shapes.

A hip joint prosthesis is immersed in the synovial fluid; therefore, the roughness needs to be related with the minimum film thickness. This film thickness ratio, $\lambda = \frac{h_{min}}{\sigma}$, allows to discriminate the lubrication mechanism in mixed (λ = 3.0—1.0) and full fluid film (λ higher than 3), more details on the lubrication regimes will be presented in **section III.5.1**. Further efforts are thus needed to achieve the complete understanding of the relationship between roughness and lubrication in hip joint bearing. As an example, the work by Zhu and Hu [133] proposed a method to solve the Reynolds equation in both the hydrodynamic region and the contact region, considering in this way the presence of asperities on the surfaces.

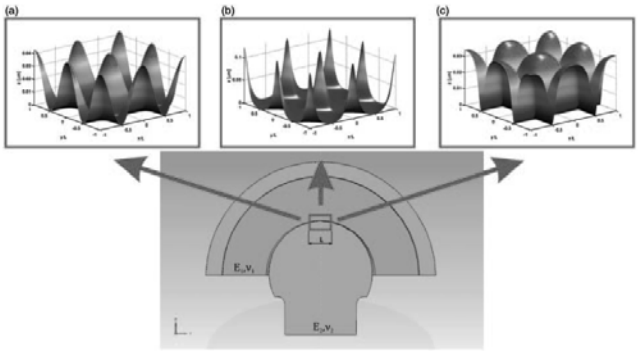

Figure III.11: *Asperity models of the cup-head problem. a) intermediate γ=1; b) sharp γ=4; c) blunt γ=1/4.*

III.4.1 Roughness measurement

By "measurement" we mean something more than inspection. Measurement is a process which give, or could give, quantitative information on single or average surface heights. It is therefore excluded from the measurements an optical examination.

There are several aspects which influences the choice of the right instrument to measure roughness on a surface: cost, ease of operation, size and robustness. Don't forgetting the issue of whether a measurement is comparative or absolute. It is also necessary to choose whether the instrument should go in physical contact with the surface, whether it should measure an area or a section or even a profile. Finally, it should be selected the right vertical range and resolution.

Many roughness measuring instruments, as stylus instruments, give absolute measurement of local heights. Other instruments, e.g. glossmeters, give average values of some surface parameters, which depends on material characteristics. These instruments require to be calibrated against an absolute instrument under the same conditions. This yield a more restricted traceability than the former instrument. Vorburbger and Teague [134] classified these instruments as "profiling" and "parametric" techniques.

Sectional measurements are usually quick and can be used to define the roughness of a surfaces. In fact, all current roughness standards are written in term of sectional roughness. For many practical purpose sectional measurements are acceptable and this way should be chosen. By the way, actual contact happens against two areas, therefore it comes the necessity to describe the areal roughness of a surfaces.

One useful way to describe the range of work of a measuring roughness instrument is due to Stedman (1987) who plotted the horizontal range and resolution of an instrument as an envelope in a 2-D space. Defined z_{max} and z_{min} the maximum and minimum heights that can be measured by the instrument, and λ_{max} and λ_{min} the longest and shortest wavelengths, this will describe a rectangle in z-λ space. Outside this rectangle the instrument will not be capable of measuring. Nevertheless, the instrument will be also limited by its steepest slope θ_{max} it can measure and the sharpest curvature C_{max} which it follows. To represent these conditions in z-λ space it is necessary to assume some simplifications on the shape of the surface. For an easy mathematical fit Stedman assumes a sinusoidal surface:

$$z = R_p \, sin\left(\frac{2\pi x}{\lambda}\right), \qquad (III.15)$$

where R_p is the amplitude. Slope and curvatures are:

$$\theta = \left(\frac{2\pi R_p}{\lambda}\right) cos\left(\frac{2\pi x}{\lambda}\right), \qquad (III.16)$$

$$C = -\left(\frac{4\pi^2 R_p}{\lambda^2}\right) sin\left(\frac{2\pi x}{\lambda}\right). \qquad (III.17)$$

To find the maximum of these functions it is necessary to impose the trigonometric function to unity, therefore taking the logarithms yields to:

$$log\, R_p = log(\theta_{max}/2\pi) + log\, \lambda\,, \qquad (III.18)$$

$$log\, R_p = log\left(\frac{C_{max}}{4\pi^2}\right) + 2\, log\, \lambda\,. \qquad (III.19)$$

On a logarithmic plot these equations are lines of slope 1 and 2, respectively. In **Figure III.13** the so obtained Stedman diagram is shown.

Considering the simplification assumed, the area described by the Stedman diagram should be considered as a maximum working envelope, where not all the may be available to the same instrument. Furthermore, this diagram refers to an instrument and not to the specific technique. For instance, it is possible to realize stylus instruments on quite different scales.

To obtain a brief description of the working conditions it is possible to represent a Stedman diagram for the different topographical measurement

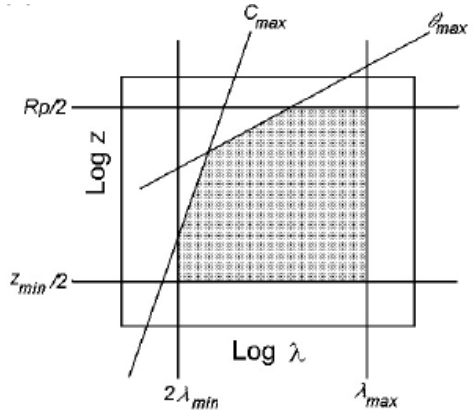

Figure III.12: *Stedman diagram.*

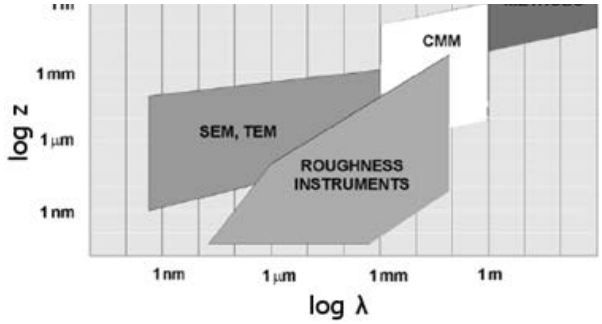

Figure III.13: *Comparison of different instruments on Stedman diagram* [245].

techniques, (see **Figure III.12**). Even though, this representation is far from complete – for simplicity, many techniques are ignored – it gives the idea that there is a large area of investigation that is not covered by any instruments.

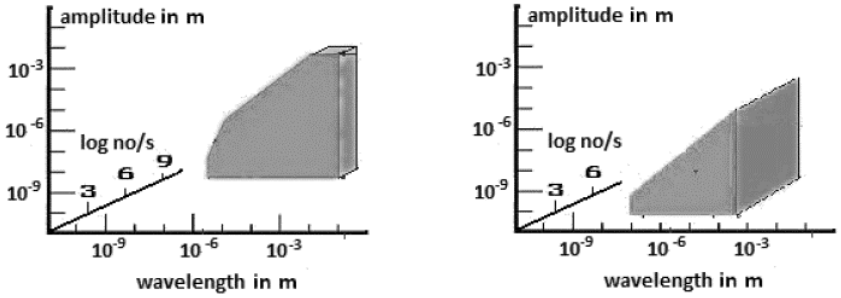

Figure III.14: *Modified Stedman diagram.*

Jones and Leach [135] proposed the introduction of a third parameter, along with z and λ, which was the velocity. Whereas, Rosén et al. [136] highlight the importance of the speed of data acquisition. These third dimension turns the diagram into a volume, applying a similar rule: the larger the volume, the more powerful the instrument (see **Figure III.14**).

III.4.1.1 Roughness measure of joint implants

Converging to the roughness analysis of prosthetic joint implants [137], several techniques can be used: conventional contact instrument [138], [139], the atomic force microscope (AFM) and optical techniques [140], [141]. The most widespread instrument used for this purpose is the stylus profilometer, in which the main components are a stylus and his diamond pin. The radius of the diamond pin, the pressure applied and the material hardness strongly influence the measurement [142]. Furthermore, the stylus can damage and modify the surface during its transit, especially when soft materials are under examination. On the other hand, optical techniques have the advantage of being contactless. Therefore, there is no risk to damage the surface under investigation. Optical methods have higher acquisition speed, and can measure 3D profiles in one single measurement, whereas stylus profilometers need multiple measurements to cover an area. Main drawbacks in optical techniques, compared to contact profilometer, are higher costs of the machine, more complex algorithm and more meticulous setups. On some very fine surfaces, a substantial divergence in value between an optical and a stylus method is recorded. Regularly, the optical methods give larger values than the stylus ones. This is because the stylus method tends to integrate, whereas the optical method differentiates e.g. it enhances edges [143].

There are interests about the best techniques usable to characterize surface parameters of a joint prosthesis. Vorburger et al. [144] compared optical and stylus methods to measure profiles of periodic grating standards and random roughness standards, on precision reference specimens (with different range

of roughness). These authors found prominent discrepancies for the Ra values between 100 and 200 nm, that seemed unrelated to the specific instrument, specimen shape and profile randomness. Durakbasa and co-workers [145], in his analysis of flat surface samples with periodic and random profiles, found optimal matching for the Ra measurements obtained by stylus profilometer and optical instruments based on focus variation. Demircioglu et al. [146] compared the roughness data observed on steel and aluminium flat samples with periodic and random profiles of different roughness classes. He used a stylus measurement and two optical methods, observing that the three devices gave comparable results for good reflective surfaces. Durakbasa et al. [147] exanimated steel samples with spherical surfaces – manufactured by surface grinding and lapping –, and he found considerable differences of R_z values between the stylus and the non-contact optical profiler. He claimed that the stylus incompetence "was due to its geometrical form comparing to a light beam", which causes lacking in lateral resolution and impossibility to detect the extreme values of profile (e.g. scratches, cracks).

III.4.2 Roughness values

There are many parameters which define the surface roughness, they can be divide in amplitude parameters and spacing (or texture) ones [148]. The former are used to measure the vertical characteristic of the surface deviations. The latter measure the horizontal characteristics of the surface deviations. The profile roughness parameters are using the *R* prefix, but these have equivalent image roughness parameters using the *S* prefix and often calculated in the same way. For example, R_a is the arithmetic mean deviation of the heights on a profile, like S_a is the arithmetic mean deviation of heights on an image.

III.4.2.1 Main amplitude parameters

To gain numerical values of roughness it is necessary first to define a referring line within the profile and thus evaluating the deviation from it. The arithmetic average height parameter, known as the centre line average (CLA), is the most used one for quality control. It defines the absolute of the mean deviation of the irregularities from the mean line, over a sampling length. It is defined as follows:

$$R_a = \frac{i}{l}\int_0^l |y(x)|dx \ .$$

Root mean square (RMS) parameter is the standard deviation of the distribution of surface heights. This results to be more sensitive than R_a to large deviation from the mean line. It is evaluated as:

$$R_q = \sqrt{\frac{1}{l}\int_0^l \{y(x)\}^2 dx} \ .$$

Ten-point height is a more sensitive parameter to occasional high peaks or deep valleys than R_a. According to the ISO standard, it is defined as the

difference in height between the average of the five highest peaks and the five deepest valleys. Whereas, the German DIN standard defines it as the average of the summation of the five highest peaks and the five deepest valleys. This parameter can be evaluated by:

$$R_{z(ISO)} = \frac{1}{n}\left(\sum_{i=1}^{n} p_i - \sum_{i=1}^{n} v_i\right),$$

$$R_{z(DIN)} = \frac{1}{2n}\left(\sum_{i=1}^{n} p_i + \sum_{i=1}^{n} v_i\right),$$

where *n* is the number of samples along the assessment length.

The maximum height of peaks above the mean line is indicated as R_p. In the same way, R_v is the maximum depth of the profile.

The maximum height of the profile is defined as the vertical distance between the highest peak and the lowest valley along the assessment length. It is indicated by R_t.

The *skewness* parameter (R_{sk}) is the third central moment of profile amplitude probability density function. It is a useful indicator of the profile symmetry about the mean line. The sign of R_{sk} indicates the predominance of peaks (i.e. $R_{sk}>0$) or valleys structures ($R_{sk}<0$) over the surface. For instance, a symmetric profile has a skewness equal to zero. It is useful in specifying honed surfaces and monitoring different types of wear conditions [149]. Its formula is:

$$R_{sk} = \frac{1}{R_q^3}\left(\int_{-\infty}^{\infty} y^3 p(y) dy\right).$$

R_{ku}, is the *kurtosis* parameter. It measures the *peakedness* (or flatness) of the height's distribution and it is descriptive of the extent to which the surface height variance is a result of sporadic acute deviations. For reference, a surface roughness described by a Gaussian height distribution is characterized by a skewness of zero and a Kurtosis of 3. A surface that has kurtosis larger than 3 is characterized by an asperity height distribution with wide wings and a narrow central peak, whereas a kurtosis smaller than 3 is an indicator of a broad surface height distribution. Skewness and kurtosis are generally suitable parameters in characterizing respectively the surface capacity of trapping the lubricant and the geometry of the contact interface [150]. It is calculated with the following expression:

$$R_{ku} = \frac{1}{R_q^4}\left(\int_{-\infty}^{\infty} y^3 p(y) dy\right).$$

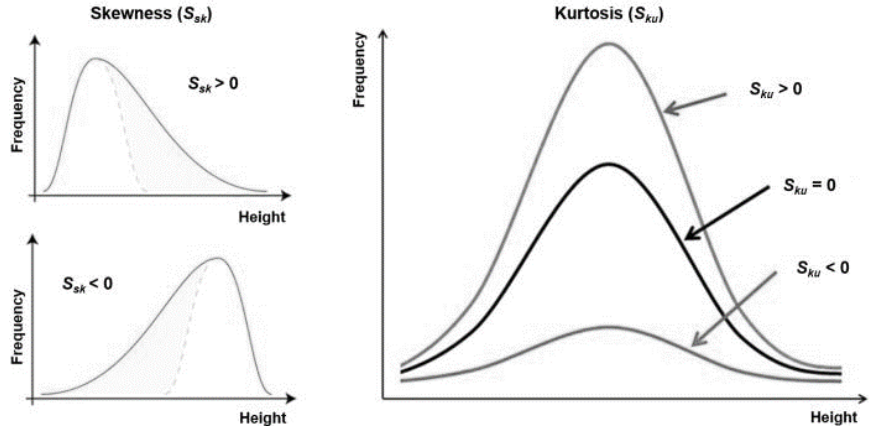

Figure III.15: *Illustration of the skewness and kurtosis values and how they correlate with the shape of the height distribution function (HDF).*

III.4.2.2 Main spacing parameters

These are very important in some manufacturing operations, as pressing steel, where to obtain a good lubrication during pressing, avoid scoring and prevent the appearance of surface texture it is necessary to evaluate the spacing parameters.

The high spot count (HSC) is defined as the number of peaks above the mean line or above a line parallel to the last one, per unit length along the assessment length.

The Peak count (P_c) parameter is defined as the number of local peaks, which is projected through a selectable band above and below the mean line by the same distance.

Mean spacing of adjacent local peaks (s) is the average spacing of adjacent local peaks of the profile measured along the assessment length. A local peak is defined as the highest part of the profile measured between two adjacent minima and is only measured if the vertical distance between those peaks is higher or equal to 10% of the R_t of the profile.

Mean radius of asperities (r_p) is defined as the average of the principle curvatures of the peaks within the assessment length. The radius of curvature for a peak (r_{pi}) can be evaluated from the following equation:

$$r_{pi} = \frac{2y_i - y_{i-1} - y_{i+1}}{l^2},$$

where y_i is the height of the peak at which its radius of curvature (r_{pi}) is going to be evaluated, y_{i-1} the height of the preceding peak, and y_{i+1} the height of the next one. The mean peak radius (r), thus can be evaluated by:

$$r_p = \frac{1}{n-2}\sum_{i=1}^{n-2}\frac{1}{\rho_{pi}}.$$

The Density of Summits, S_{ds}, is the number of local maximums per area:

$$S_{ds} = \frac{Number\ of\ local\ maximums}{(M-1)(N-1)\delta x \delta y}.$$

III.4.2.3 Main hybrid parameters

S_{sc} is the Mean Summit Curvature for the various peak structures. Peaks are found as described above for the summit density. S_{sc} is the average of the principal curvature of the local maximums on the surface, and is defined as:

$$S_{sc} = \frac{-1}{N} \iint_{Summit-Area} \left(\frac{\partial^2 z(x,y)}{\partial x^2}\right) + \left(\frac{\partial^2 z(x,y)}{\partial y^2}\right) dxdy \ .$$

The Root Mean Square Gradient, S_{dq}, is the RMS-value of the surface slope within the sampling area, and is defined as:

$$S_{dq} = \sqrt{\frac{1}{A}\int_0^{Lx}\int_0^{Ly}\left(\frac{\partial Z(x,y)}{\partial x}\right)^2 + \left(\frac{\partial Z(x,y)}{\partial y}\right)^2 dydx} \ .$$

III.5 Lubrication

As tribology investigates on every aspect concerning interacting surfaces, involving mainly friction and wear, the lubrication is of paramount importance. It can intensely decrease the frictional forces acting on two surfaces in relative movements.

III.5.1 Regimes of lubrication

There are four regimes of lubrication, that rules the friction condition within two coupled surfaces under relative motion. The Stribeck Curve (see **Figure III.16**) show the different regimes as function of the viscosity, the relative velocity *v*, and the normal pressure *p* [151].

In dry condition there is no lubricant between the surfaces, only the oxide top coating on each body separate them. In this case the frictional force is high, and this occurrence is limited to few cases regarding industrial application.

In the limit condition of lubrication – known as *boundary lubrication* – the two surfaces are separated by a limited number of monomolecular layers of lubricant. These layers constitute an extremely thin film, that stays anchored to each surface thanks to a complex mixture of physical-chemical phenomena, as the adsorption, the polarity properties of the molecule, the surfaces tension, etc.

The lubricant film is not thick enough to admit the separation of the surface asperities, that in many points get in contact to each other causing wear phenomena. Thus, the lubricant has the main function of limiting these points of contact and therefore the micro-welding, reducing the frictional force and the wear of the body coupled.

This lubrication is generally applied where the involved machine members are slow and subjected to high loads, but also in lubricated system when the supply is limited (as for drop oiler).

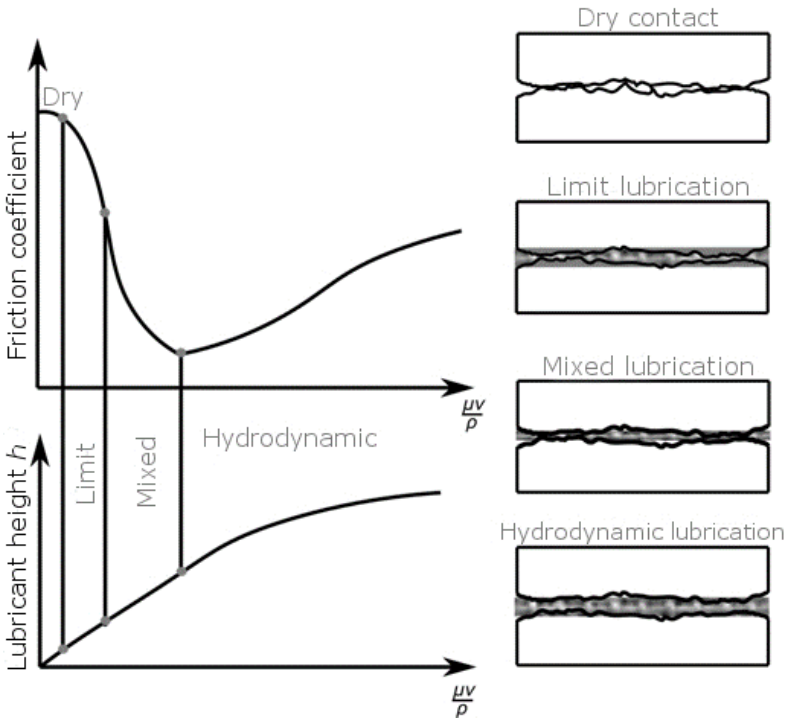

Figure III.16: *Stribeck curve.*

The *fluid film lubrication* – called *hydrodynamic lubrication*, in case of uncompressible fluids – is defined by the presence of a continuous film of lubricant that completely separate the bodies. This separation is allowed by the higher pressure that is realized inside the fluid than that of the environment. This pressure difference is due to the tensional state within the moving lubricant that is strictly connected to the viscosity of the fluid.

To obtain this lubrication regime it is necessary that, during the motion, it is realized a fluid film sensibly higher than the average roughness height of the coupled surfaces.

The *mixed lubrication* is the most frequent condition when there are low velocities and small loads. In this regime the surface peaks are under lubricated condition whereas the valleys are fulfilled with fluid. The frictional forces are mild.

III.5.2 Governing Equations of Hydrodynamic Lubrication

To have a first understand of the lubrication mechanism between two elements sliding against each other, it is necessary primary to obtain the governing equations of the fluid film. Even if the theory of Reynolds can totally explain this mechanism, its application in real project can be quite hard.

In fact, its solution is difficult to obtain in an analytic way. Therefore, approximations or numerical analysis are needed.

As first step to obtain the governing equations, there is the need to define the characteristic of the motion of the fluid. The stress acting on a generic surface of the fluid is constant and normal to it; this stress is called pressure. In a real fluid, there are also frictional forces, which makes necessary to consider also the deformation stresses. The deformation of the fluid can be assumed equal to an expansion along three lines, called *principal axes*, the related stresses are called *principal stresses*.

The fundamental condition that must be respected is the continuity equation, it can be expressed, referring to **Figure III.17**, in the following way:

$$\frac{\partial \rho}{\partial t} + \frac{\partial}{\partial x}(\rho u) + \frac{\partial}{\partial t}(\rho v) + \frac{\partial}{\partial t}(\rho w) = 0 \qquad (III.20)$$

Where ρ is the density of the fluid, u, v and w the velocities in x, y and z directions, t the time.

If the motion is stationary, this becomes:

$$\frac{\partial}{\partial x}(\rho u) + \frac{\partial}{\partial t}(\rho v) + \frac{\partial}{\partial t}(\rho w) = 0 \qquad (III.21)$$

If the fluid is incompressible (ρ = constant), then the equation is:

$$\frac{\partial u}{\partial x} + \frac{\partial v}{\partial t} + \frac{\partial w}{\partial t} = 0 \qquad (III.22)$$

For a compressible fluid, it is possible to obtain the motion equations, which are referred to as *Navier-Stokes equations*. Considering an equilibrium of forces (Newton's law), on an infinitesimal parallelepiped element of fluid, we obtain the following equations system:

$$\rho \frac{D\boldsymbol{U}}{Dt} = \rho \boldsymbol{F} - \nabla p - \frac{2}{3}\nabla(\eta \nabla \cdot \boldsymbol{U}) + 2(\nabla \cdot \eta \nabla))\boldsymbol{U} + \nabla \times (\eta(\nabla \times \boldsymbol{U})) \qquad (III.23)$$

where **U** = (u,v,w) velocity vector;
F = (f_x,f_y,f_z) body forces;
p is hydrostatic pressure;
η is the dynamic viscosity, which can also be related to the kinematic viscosity $\nu = \eta/\rho$.

Considering that in most of the cases the temperature variations are limited, the viscosity can be considered constant.

The Navier-Stokes equations present enormous difficulties to be solved, therefore some approximations are needed. To do so, it must be considered the magnitude order of its terms. The equations terms can be scaled according to the following assumptions:

$$X = \frac{x}{l_0} \qquad Z = \frac{z}{h_0} \qquad T = \frac{t}{\left(\frac{l_0}{u_0}\right)} \qquad \bar{u} = \frac{u}{u_0}$$

$$\bar{w} = \frac{w}{w_0} \qquad \bar{\eta} = \frac{\eta}{\eta_0} \qquad \bar{\rho} = \frac{\rho}{\rho_0} \qquad P = \frac{p}{(\eta_0 u_0 l_0 / h_0^2)}$$

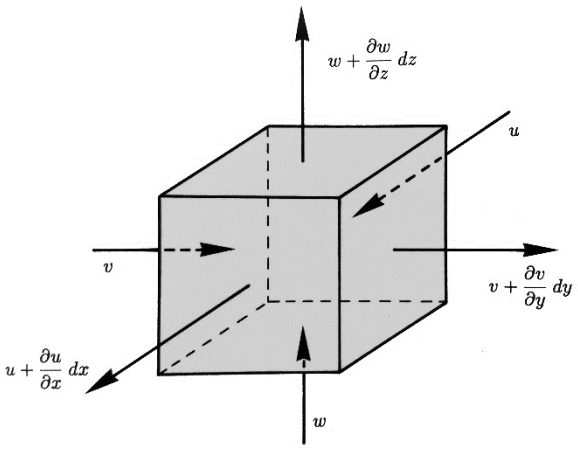

Figure III.17: *The control volume.*

It is possible to rewrite the equations in non-dimensional form as follows:

$$x: \quad \bar{\rho}\left(\frac{\partial \bar{u}}{\partial T} + \bar{u}\,\frac{\partial \bar{u}}{\partial X} + \frac{w_0}{u_0}\bar{w}\frac{\partial \bar{u}}{\partial Z}\right) = \frac{l_0}{u_0^2}\bar{\rho}f_x - \frac{\eta_0}{\rho_0 u_0 l_0}\left(\frac{l_0}{h_0}\right)^2\frac{\partial P}{\partial X} - \frac{2\eta_0}{3\rho_0 u_0 l_0}\frac{\partial}{\partial X}\left(\bar{\eta}\left(\frac{\partial \bar{u}}{\partial X} + \left(\frac{w_0}{u_0}\right)\left(\frac{l_0}{h_0}\right)\frac{\partial \bar{w}}{\partial Z}\right)\right) + \frac{2\eta_0}{\rho_0 u_0 l_0}\frac{\partial}{\partial X}\left(\bar{\eta}\frac{\partial \bar{u}}{\partial X}\right) + \frac{\eta_0}{\rho_0 u_0 l_0}\left(\frac{l_0}{h_0}\right)^2\frac{\partial}{\partial Z}\left(\bar{\eta}\left(\frac{\partial \bar{u}}{\partial X} + \left(\frac{w_0}{u_0}\right)\left(\frac{h_0}{l_0}\right)\frac{\partial \bar{w}}{\partial X}\right)\right) \qquad (III.24)$$

$$z: \quad \bar{\rho}\left(\frac{\partial \bar{w}}{\partial T} + \bar{u}\,\frac{\partial \bar{w}}{\partial X} + \frac{u_0}{w_0}\frac{h_0}{l_0}\bar{w}\frac{\partial \bar{w}}{\partial Z}\right) = \frac{h_0}{u_0^2}\frac{1}{\varepsilon^2}\,\bar{\rho}f_z - \frac{\eta_0}{\rho_0 u_0 l_0}\left(\frac{l_0}{h_0}\right)^4\frac{\partial P}{\partial Z} - \frac{2\eta_0}{3\rho_0 u_0 l_0}\left(\frac{l_0}{h_0}\right)^2\frac{\partial}{\partial Z}\left(\bar{\eta}\left(\frac{\partial \bar{u}}{\partial X} + \left(\frac{w_0}{u_0}\right)\left(\frac{l_0}{h_0}\right)\frac{\partial \bar{w}}{\partial Z}\right)\right) + \frac{2\eta_0}{\rho_0 u_0 l_0}\left(\frac{l_0}{h_0}\right)^3\frac{\partial}{\partial Z}\left(\bar{\eta}\frac{\partial \bar{u}}{\partial Z}\right) + \frac{\eta_0}{\rho_0 u_0 l_0}\left(\frac{l_0}{h_0}\right)^2\frac{\partial}{\partial X}\left(\bar{\eta}\left(\frac{\partial \bar{u}}{\partial Z} + \left(\frac{w_0}{u_0}\right)\left(\frac{h_0}{l_0}\right)\frac{\partial \bar{w}}{\partial X}\right)\right) \qquad (III.25)$$

And introducing the parameters:

$$\varepsilon = \frac{h_0}{l_0} \quad and \quad Re = \frac{u_0 l_0}{\nu}$$

$$x: \quad \varepsilon^2 Re\bar{\rho}\left(\frac{\partial \bar{u}}{\partial T} + \bar{u}\,\frac{\partial \bar{u}}{\partial X} + \frac{w_0}{u_0}\bar{w}\frac{\partial \bar{u}}{\partial Z}\right) = \varepsilon^2 Re\,\frac{l_0}{u_0^2}\bar{\rho}f_x - \frac{\partial P}{\partial X} - \frac{2\varepsilon}{3}\frac{\partial}{\partial X}\left(\bar{\eta}\left(\varepsilon\frac{\partial \bar{u}}{\partial X} + \left(\frac{w_0}{u_0}\right)\frac{\partial \bar{w}}{\partial Z}\right)\right) + 2\varepsilon^2\frac{\partial}{\partial X}\left(\bar{\eta}\frac{\partial \bar{u}}{\partial X}\right) + \frac{\partial}{\partial Z}\left(\bar{\eta}\left(\frac{\partial \bar{u}}{\partial X} + \left(\frac{w_0}{u_0}\right)\varepsilon\frac{\partial \bar{w}}{\partial X}\right)\right) \qquad (III.26)$$

$$z: \quad \varepsilon^4 Re\bar{\rho}\left(\frac{\partial \bar{w}}{\partial T} + \bar{u}\,\frac{\partial \bar{u}}{\partial X} + \frac{w_0}{u_0}\varepsilon\bar{w}\,\frac{\partial \bar{w}}{\partial Z}\right) = \varepsilon^3 Re\,\frac{h_0}{u_0^2}\bar{\rho}f_z - \frac{\partial P}{\partial Z} - \frac{2\varepsilon}{3}\frac{\partial}{\partial Z}\left(\bar{\eta}\left(\varepsilon\frac{\partial \bar{u}}{\partial X} + \left(\frac{w_0}{u_0}\right)\frac{\partial \bar{w}}{\partial Z}\right)\right) + 2\varepsilon\frac{\partial}{\partial Z}\left(\bar{\eta}\frac{\partial \bar{u}}{\partial Z}\right) + \varepsilon^3\frac{\partial}{\partial X}\left(\bar{\eta}\left(\frac{\partial \bar{u}}{\partial Z} + \left(\frac{w_0}{u_0}\right)\varepsilon\frac{\partial \bar{w}}{\partial X}\right)\right) \qquad (III.27)$$

Considering that the term ε is small, the equations reduce to:

$$x: \quad \frac{\partial p}{\partial x} = \frac{\partial}{\partial z}\left(\eta\frac{\partial u}{\partial z}\right) \qquad (III.28)$$

$$z: \quad \frac{\partial p}{\partial z} = 0\,, \qquad (III.29)$$

The second equation means that the pressure is constant in the *z* direction.

If the fluid is Newtonian, which means that the viscosity does not change with the shear rate, it is possible to integrate the first equation along the *z* direction and thus find the velocity profile:

$$u(x,z) = \frac{z^2}{2\eta}\frac{dp}{dx} + C_1(x)z + C_2(x)\,. \qquad (III.30)$$

C_1 and C_2 can be found by imposition of the boundary conditions, $u(x,0) = u_1$ and $u(x,h) = u_2$:

$$u(x,z) = \frac{1}{2}\frac{dp}{dx}(z^2 - zh) + (u_2 - u_1)\frac{z}{h} + u_1\ . \qquad (III.31)$$

By the integration of $\rho \cdot u$ between *0* and *h* it will be found the mass flow:

$$q(x) = -\frac{\rho h^3}{12\eta}\frac{dp}{dx} + \frac{u_1+u_2}{2}\,\rho h\,. \qquad (III.32)$$

Standing the conservation of the mass $\frac{\partial}{\partial x}\big(q_x(x,y)\big) + \frac{\partial}{\partial y}\Big(q_y(x,y)\Big) + \frac{\partial(\rho h)}{\partial t} = 0$, it brings to:

$$\frac{\partial}{\partial x}\left(\frac{\rho h^3}{12\eta}\frac{\partial p}{\partial x}\right) + \frac{\partial}{\partial y}\left(\frac{\rho h^3}{12\eta}\frac{\partial p}{\partial y}\right) = \frac{(u_1+u_2)}{2}\frac{\partial(\rho h)}{\partial x} + \frac{(v_1+v_2)}{2}\frac{\partial(\rho h)}{\partial y} + \frac{\partial(\rho h)}{\partial t}\,. \qquad (III.33)$$

Known as the **Reynolds Equation** in 2-D. The *h* parameter is the film thickness, it is a known parameter, fully described by these terms:

$$h(x,y) = h_0 + h_1(x,y) + \delta(x,y,t)\,, \qquad (III.34)$$

where h_0 is the load balance component, h_1 the initial geometry and δ is the deformation due to pressure, if an elastic model is considered.

As already stated the solution of the Reynolds equation, for complex shapes, is not easy to obtain, therefore numerical analysis becomes necessary, using a finite difference discretization.

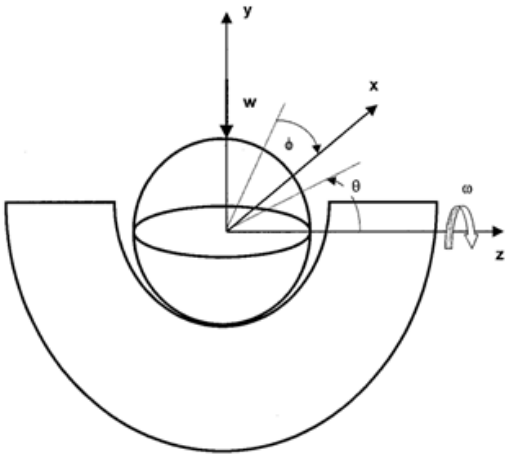

Figure III.18: *A ball-in-socket model for lubrication analysis.*

Lubrication in joint prostheses plays a fundamental role for the mobility and friction, therefore it affects the long-term successful function. To understand the lubrication behaviour, it will be necessary to compare the minimum film thickness to the roughness of the counter-bodies. Several studies report to use the minimum film thickness formulae developed by Hamrock and Dowson [152]. Nevertheless, numerical approach could also be used to solve the governing equation and obtain the minimum fil thickness. The hip joint can be considered as a ball-on-socket joint, therefore the governing Reynolds equation should be written in spherical coordinate, as follows [153]:

$$sin\,\theta\,\frac{\partial}{\partial\theta}\left(h^3\,sin\,\theta\,\frac{\partial p}{\partial\theta}\right)+\frac{\partial}{\partial\phi}\left(h^3\,\frac{\partial p}{\partial\phi}\right)=6\eta R_2^2\omega\,sin\,\theta^2\,\frac{\partial h}{\partial\phi}\,, \qquad (III.35)$$

where θ and Φ are the angular coordinates as explained in **Figure III.18**, ω is the angular velocity

The film thickness is a combination of the gap and the elastic deformation, due to hydrodynamic pressure:

$$h=e\left(1-\varepsilon_x\,sin\,\theta\,cos\,\phi-\varepsilon_y\,sin\,\theta\,sin\,\phi\right)+\delta\,, \qquad (III.36)$$

where e is the radial clearance, difference in radius of sphere and socket, ε is the eccentricity ratio e/c and δ is the elastic deformation.

The boundary conditions for this problem are:

$p=0$ at the limit of the internal surface of the cup;

$\frac{\partial p}{\partial\phi}=\frac{\partial p}{\partial\theta}=0$ cavitation boundary condition.

Furthermore, the load imposed must be balanced by the integration of the pressure:

$$f_x = R_2^2 \int_{\phi_1}^{\phi_2} \int_{\theta_1}^{\theta_2} p \sin\theta \cos\phi \sin\theta \, d\theta d\phi = 0 ,$$
$$f_y = R_2^2 \int_{\phi_1}^{\phi_2} \int_{\theta_1}^{\theta_2} p \sin\theta \sin\phi \sin\theta \, d\theta d\phi = w ,$$
$$f_z = R_2^2 \int_{\phi_1}^{\phi_2} \int_{\theta_1}^{\theta_2} p \cos\theta \sin\theta \, d\theta d\phi = 0 . \qquad (III.37)$$

Finite difference method must be applied to solve these governing equations. The domain on the cup (Φ and θ from 0 to π), would be divided in number of uniform grids ($m \times n$). Whereas, the elastic deformation can be achieved through finite element method, due to the complex geometry of the model.

III.6 Wear

When materials are in contact with each other and undergo relative motion, wear of the surfaces occurs. As the reason for performing a joint replacement is to get motion without pain it is not surprising that all implants are affected by wear.

According to DIN 50 320, wear is the progressive removal of material from a surface in sliding or rolling contact against a countersurface. As described in many textbooks, e.g. Zum Gahr (1987) and Hutchings (1992), different types of wear may be identified by examining the material removal mechanisms, the wear mechanisms, that cause the wear on a microscopic level. There can be found many ways of classifying wear by wear mechanisms, but a frequently accepted classification discriminates between *adhesive wear*, *abrasive wear*, *wear caused by surface fatigue*, and *wear due to tribochemical reactions*. Over a longer sliding distance, either one mechanism alone, or a combination of several of these mechanisms, causes a continuous removal of material from the coupled surfaces, and thereby also adds to the friction force that opposes the relative movement. Such continuous, steady-state wear and friction conditions may be quantified in terms of wear rates, i.e. removed material mass or volume per sliding distance or time, or its inverse, the wear resistance, and in terms of friction forces or friction coefficients.

Often, the wear process undergoes several phases as sliding advances; at least three stages are usually identified: the wear starts with what could be

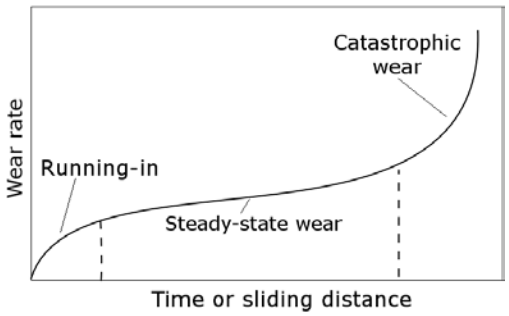

Figure III.19: *Typical wear stages appearing over longer service times in sliding contacts.*

called a *run-in stage*, during which steady-state conditions are building up (**Figure III.19**). The running-in period could be crucial for some sliding systems, as for many types of bearings and gears. During this stage the mating surfaces conform to each other in such a way that the load is more positively distributed over the surfaces. During the early running-in stages, the wear rates may be relatively high; running-in should, however, be short compared to the whole lifetime of the component. *Steady-state conditions* with low wear rates and stable friction values should prevail for most of the lifetime of the system, but low steady-state wear rates will eventually alter clearances or surface properties to the extent that components fail, during a brief, final, *catastrophic stage* during which wear rates are high and severe surface damage occurs.

The clinical consequences of wear of joint replacements are threefold. First, as wear proceeds, the tolerances between the bearing surfaces become altered. This may lead to changes in the biomechanics, function, and range of motion of the joint (which may be increased or decreased), impingement, subluxation, or dislocation. Second, wear may subsequently alter the physicochemical properties of the bearings, surface coatings, and other treatments. Third, wear of the materials generates particulate debris which may lead to a chronic synovitis, foreign body, and chronic inflammatory reaction, periprosthetic osteolysis, loosening, or pathologic fracture.

Prosthetic by-products due to wear may have both local and systemic consequences. With a metal-on-plastic articulation such as a knee joint, progressive wear may compromise the biomechanics of the joint such that sliding occurs in addition to rolling. Patients may complain of the knee suddenly giving way or feeling unstable. Although wear may have mechanical consequences, in a metal-on-polyethylene articulation, hundreds of thousands of polyethylene particles around 0.5±5 μm in size are generated with every step [154].

Figure III.20: *Station of multiple hip joint simulators.*

III.6.1 Wear analysis

The most important challenges in joint replacement surgery today is the construction of a joint replacement that will last a lifetime. Currently the artificial joints are investigated and subjected to specific simulation tests before receiving the required approval for clinical use. Moreover, simulation tests of implants are an important phase of research and assessment for the optimization of prosthetic materials as well as for the design of the prosthesis. These tests are performed with the aim of find the behaviour of the prosthesis and subsequent assessment of the wear of the prosthetic components and the level of surface finish to establish the efficacy of the system or, alternatively, provide useful values to improve its performance.

III.6.1.1 Joint Simulators

Wear joint simulators (**Figure III.20** and **Figure III.21**) allow testing of materials used as prosthetic components by reproducing as closely as possible the real physiological conditions in the articulation and providing the loads

Figure III.21: *Station of multiple knee joint simulators.*

and micro-motion to mimic the exact movement of the prosthesis. However, wear tests on a simulator are long and expensive due to the large number of cycles at low frequency that must be executed.

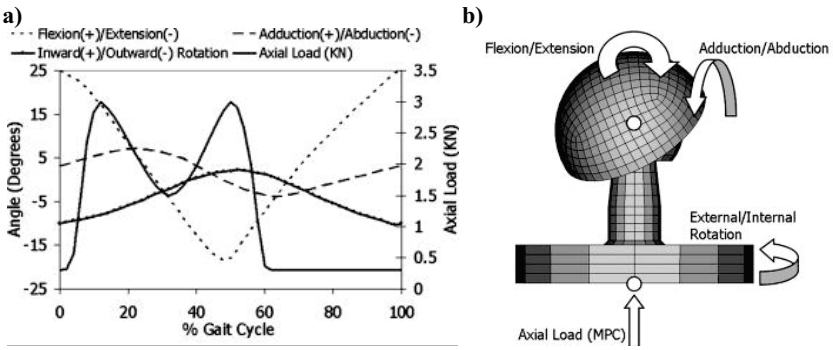

Figure III.22: *Hip joint in-vitro test specification: a) ISO movement and axial load for DC method; b) direction of movements and load.*

The ISO 14242 and ISO 14243 defines those which are the criteria and methods used for the *in-vitro* simulations performed to test hip and knee replacement respectively. These standards define the loads and motions that the simulator must reproduce on artificial prosthesis to imitate the normal activity of the level walking. At present this statement defines two simulation techniques: the force control (FC) and the displacement control (DC). For both methods, the level walking is the only activity considered. Regards the hip joint simulator, the DC provides the movements of flexion/extension, adduction/abduction and inward/outward rotation and the axial load (see **Figure III.22**).

Regards the knee simulator, the FC technique indicates, according to the flexion/extension movement performed by the joint, what are the forces and moments which this joint is subjected to. The norm provides the values of the Axial Load (F_z), of the Anterior/Posterior Load (F_y) and the values of the Axial Moment (M_z) during the activity of walking. The DC technique, defines, according to the movement of flexion/extension performed by the knee, the

a)

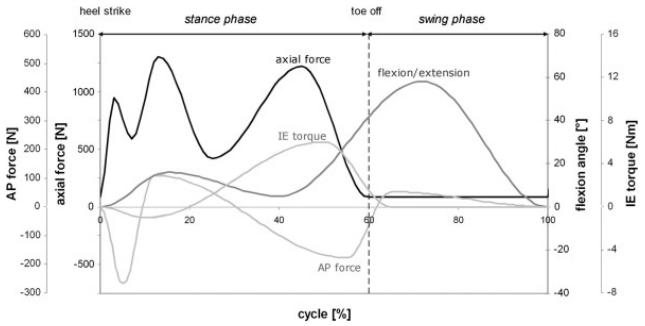

b)

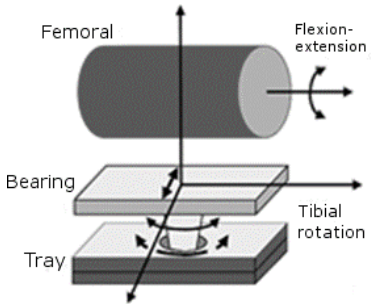

Figure III.23: *Knee joint* in-vitro *test specification: a) ISO movement and axial load for DC method; b) direction of movements and load.*

movements for the other degrees of freedom; it provides the values for the internal/external rotation, the anterior/posterior motion and the value of the Axial Load (F_z) (see **Figure III.23**).

III.6.1.2 Standard Tribometers

Apart from this high-level wear simulators, there is the possibility to study the tribological behaviour of coupled materials through standard tribometers. They can be distinguished basing on two different criteria, by the nature of the relative motion, or by the operative conditions. There are more parameters that should be considered in the selection of the right tribometer to use:

- velocity and type of relative motion: in many cases there is the need to find a critical velocity for which a certain condition is verified, for this purpose an instrumental apparatus with continuous variation control on the velocity is required; for the type of motion there are two possibilities: unidirectional and reciprocatory;
- geometries of the coupled system: for the conventional apparatus the main geometries are sphere vs sphere, cylinder vs cylinder, plan vs plane and cylinder vs plane.

There are several types of tribometers, which can be used to replicate a wide variety of operative conditions. The most widespread can be summed up as shown in **Figure III.24**:

- block-on-ring;
- pin-on-disk or ball-on-disk;
- reciprocator, as ball-on-flat or pin-on-flat;
- four ball.

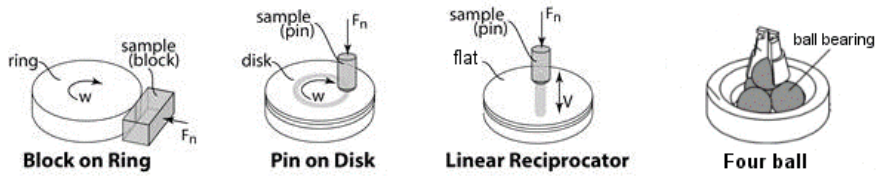

Figure III.24: *Standard tribometers*

The tribometers can replicate, in a controlled environment, the real conditions in which the coupled materials will be in action. Thus, allowing the study of the frictional and wear behaviour of the paired materials.

III.6.2 Comparison across wear tests using a hip simulator

The *in vitro* tests using a hip simulator were performed on ceramic and polyethylene materials. International literature on alumina and/or zirconia reports the effects on wear of different ceramic composites. In particular, in the 2001, Affatato and co-workers [155] tested two new types of mixed-oxide ceramics (alumina and yttria-stabilised zirconia) femoral heads and acetabular cups containing different ratios of alumina and zirconia. These components were compared with pure commercial alumina in terms of wear behaviour in a hip joint simulator. After 10 million cycles the pure alumina acetabular cups showed an average volumetric wear rate of 0.01 $mm^3/10^6$cycles whereas the experimental mixed-oxides acetabular cups exhibited an average volumetric wear rate of 0.02 $mm^3/10^6$cycles. In another experimental wear test, new nano-mixed-oxides ceramics for orthopaedic field were developed and tested onto a hip simulator for seven million cycles as reported by Affatato et al. [156]; these new composites materials showed a wear rate comparable with the pure alumina tested in the same experiment. No statistically significant differences were observed between the wear behaviours of the three sets of cups at a 95% level of confidence. Williams et al. [157] compared the wear behaviour of ZTA and alumina femoral head against CoCrMo acetabular cups in normal and severe conditions, claiming the impossibility to evaluate the wear rate of the ceramic components due to the low mass loss. He found, instead, a steady-

state wear rate of the metallic cups equal to 0.023±0.005 and 0.623±0.252 $mm^3/10^6$ cycles, in normal and severe condition respectively. In a more recent study, Affatato et al. [158], analysed some ceramics prostheses (heads and cups) explanted after a mean follow-up of 9 year in situ. They were considered the three generations of the world-wide implanted ceramics (Biolox® ***vs***. Biolox® Forte ***vs***. Biolox® Delta). Fluorescence measurements suggested different wear mechanisms in the three sets of retrievals. Micro-cracking was predominant in Biolox, while in Biolox® Forte and Biolox® Delta a wider range of residual stress values was observed upon wear. Raman spectroscopy of Biolox® Delta femoral heads showed a progressive improvement in material composition (i.e. progressive decrease of the monoclinic zirconia content).

The influence of the wear behaviour of different conventional and cross-linked Polyethylene sterilised with different methods was analysed by Affatato et al. [159]. After 5 million cycles, significant differences ($p=0.05$) were observed between all the polyethylene cups. Wang et al. [160] tested reinforced UHMWPE against CoCrMo femoral head in a hip simulator with bovine serum and reported a reduction of the wear rate as the content of Bovine Bone Hydroxyapatite (BHA) powders increases. The reduction from the pure UHMWPE to the reinforced acetabular cup was equal to 46%, with a concentration of 30% of the filler. For higher values of the concentration filler, the wear rate seemed to reach a stable value. Ge et al. [161] found a decrease in the severity of adhesive wear for UHMWPE acetabular cup reinforced with natural coral (NC). The wear test executed on the hip simulator leaded, after one million running cycles, to a cumulative mass loss of the UHMWPE reinforced with 30% NC reduced by 70% in respect to neat polymer. Brockett et al. [162] tested in a hip wear simulator five 36mm diameter Biolox Delta heads paired with extruded CFR-PEEK cups. The wear of a novel ram-extruded CFR-PEEK cup, articulating with a Biolox Delta ceramic head was assessed through 10 million cycles in experimental wear study. The mean wear rate over the period of the study was very low, with less than $1mm^3/Mc$ measured and was comparable with reported wear rates for 36mm diameter hard-on-hard bearings configurations.

Adelina Borruto [163] carried out a wear test on an alternative bearing surface in the field of total hip replacements. More in depth, the material is composed of a polymer composite polyether-ether-ketone (Peek) as the matrix and a carbon fibre as reinforcement Peek material. The wear tests (ASTM 99G) have been performed with a pin on disc tribometer in an air environment, under the following conditions: dry, water lubrication using demineralised water as a lubricant and human serum. The results of this test emphasized that the wear tests on Peek reinforced with carbon fibres demonstrates a very low wear and therefore an extremely low quantity of debris produced, in water and human serum lubrication and even under dry conditions. For this author, it

seems clear that Peek reinforced by carbon fibres is an excellent material to use for prosthetic applications.

Therefore, this willing to obtain composite material with better characteristic have a strong impact on the biomedical field. Combination of multi-phased composite aim at improving mechanical and tribological behaviours of the currently widespread hip joint prostheses. Before CNTs and graphene reinforced composites can achieve their whole potential in hip arthroplastic applications, there is the need of a better investigation on the cytotoxicity of these nano-fillers, which is still a matter of apprehension [88].

The complex nature itself of these materials, which involves combination and interaction of the multi-phase components, limits the prediction on the friction and wear behaviour. Mainly, these characteristics are evaluated through the means of tribotests that are strongly influenced by the experiment configuration, such as the geometry, the environment, the lubricant and the relative velocity, not mentioning that they are time and money consuming.

III.7 Experimental investigation on biological tribopairs

In this section it will be shown the results of a wide experimental analysis on the tribological behaviour of typical tribopairs for joint implants. This section is extracted from the article "*Experimental comparison on tribological pairs UHMWPE/TIAL6V4 alloy, UHMWPE/AISI316L austenitic stainless and UHMWPE/AL2O3 ceramic, under dry and lubricated conditions*" published on the journal Tribology International 96 in 2016 (pages 349-360), authors: Alessandro Ruggiero, Roberto D'Amato, Emilio Gomez, Massimiliano Merola.

III.7.1 Introduction

Due to its several excellent properties, Ultrahigh Molecular Weight Polyethylene (UHMWPE) has been used as a bearing material for total joint replacement for over 60 yrs. Since 1962, when it was introduced to replace polytetrafluoroethylene (PTFE) for its biocompatibility, low friction and high wear resistance, it is the material of choice for total joint arthroplasty bearings, mostly implanted in the hip and the knee of a human body. As the service life of artificial joints prolongs, the lubrication mechanisms in the normal human joints and the problems of friction and wear in the prosthesis have been addressed by many authors [164]–[167] due to its importance in the performance of these devices. Currently, the hip and the knee joints surgical implants undergo degradation after 10–15 years of use [168]. The mechanical resistance, friction and wear are not the only properties to be considered as for chosen materials regarding the head and the cup of the prosthesis but also biocompatibility and corrosion resistance. Therefore, it is inevitable to improve the above mentioned properties by combining in the best way the

UHMWPE for the cup Total Hip Replacements (THR) and for the tibial bearings Total Knee Replacements (TKR) and alumina, stainless steel or titanium alloy for the head in the hip implants and for femoral condylar components in TKR [169]. Another very important aspect to consider for improving the lubrication of the prosthesis is the choice of a proper lubricant fluid that simulates the behavior of the joints in vivo [170]. Several studies reveal that the effects on friction and wear of the various components of the synovial fluid (SF) depend on the presence of Hyaluronic Acid (HA) and Albumin. In fact, the HA is responsible for the high value of viscosity and albumin enhances the boundary lubrication of the joint [171]–[173]. Accordingly, the purposes of this study are to clarify the tribological properties, under dry and lubricated condition, of UHMWPE sliding faces against AISI316L austenitic stainless steel, against TiAl6V4 alloy and against Alumina (Al_2O_3) by using a pin-on-flat reciprocatory tribometer. In case of lubricated condition, a biological model fluid has been used: sodium hyaluronate (Hyalgan®). In order to measure the friction coefficient and the wear several load conditions and several frequencies conditions have been simulated to investigate on the tribological behaviour of the above-mentioned couplings. The worn surface of the UHMWPE specimens was analysed by a 3D Optical Surface Metrology System Leica DCM 3D, which provided three-dimensional scans of the tribometer tracks on UHMWPE surfaces.

III.7.2 Material and methods

III.7.2.1 Materials

TR-Bio 282 pin-on-flat reciprocatory DUCOM tribometer was used to measure the friction and wear properties of three following coupling materials: UHMWPE (GUR 1050) against AISI316L austenitic stainless steel, UHMWPE against TiAl6V4 alloy and UHMWPE against Alumina (Al_2O_3-99.5%). The main mechanical properties of the materials are shown in **Table III.1**.

Table III.1: Some main properties of the materials

Material	Young's Modulus (GPa)	Poisson's ratio	Hardness
TiAl6V4	114	0.34	28-42 HRC
AISI 316L	193	0.27	25–39 HRC
Al_2O_3	370	0.22	1440*
UHMWPE	0.690	0.46	48**

* (kg/mm^2)
** D scale

Polyethylene has been cut and polished from two different tibial inserts in square-shaped $10\times10\times5$ mm^3. Calorimetric studies on both tibial inserts of two different prostheses have been conducted to make sure we were in the presence of UHMWPE of some characteristics. The differential scanning calorimetry (DSC) measurements were carried out using a DSC-823^e METTLER-Toledo of the Polymer Technology Lab at the ETSIDI – Technical University of Madrid.

Both samples for the DSC analysis have been cut into pieces of 12.200 mg for the specimen A and 11.900 mg for the sample B. All the dynamic scans were registered between 25 and 180 ºC (heating), 180-25 ºC (cooling) to eliminate thermal histories and between 25-180 ºC (heating) for the analysis (**Figure III.25**) [174].

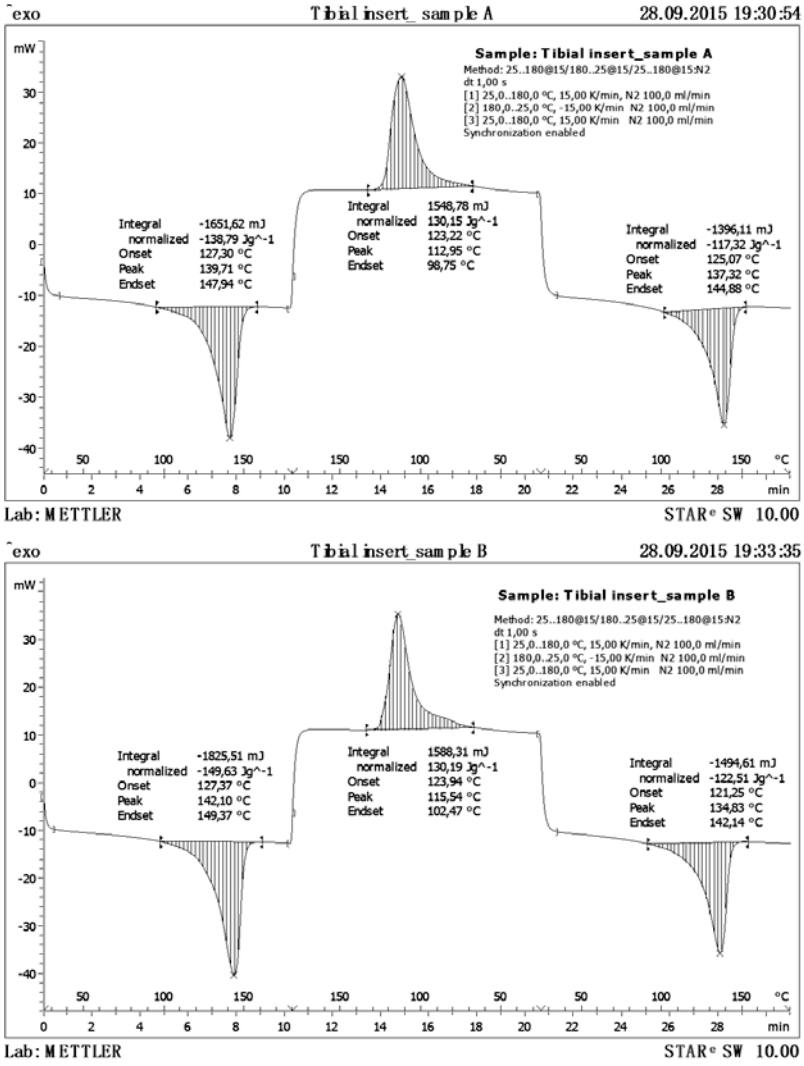

Figure III.25*: Differential scanning calorimetry DSC-823^e METTLER-Toledo*

The melting point (T_m) was measured as the maximum temperature of the endotherm in a dynamic scan. The degree of crystallinity, X_c (%), of the UHMWPE was also calculated as the area under the endotherm (ΔH) divided by the enthalpy of fusion of a 100% crystalline ($\Delta H_{100\%}$) UHMWPE, which was taken to be 293,6 J/g [175]: $X_c(\%) = \frac{\Delta H}{\Delta H_{100}} * 100$. The melting point and the crystallinity of both samples are reported in **Table III.2**.

Table III.2*: The melting point and the crystallinity of both UHMWPE samples*

Sample	Melting point (ºC)	Crystallinity (%)
A	137.2	39.96
B	134.83	41.72

From the **Table III.2** it is possible to note that the values of the obtained melting temperature in DSC test result to be just like those related to UHMWPE [98]. The austenitic stainless steel AISI 316L pin and Al_2O_3 pin were sphere-shaped with a diameters of 3 mm, 6 mm and 10 mm while for the TiAl6V4 alloy pin was sphere-shaped with a diameters of 3 mm and 6 mm. **Figure III.26** shows: a) Polyethylene cuts from a tibial insert in square-shaped and an example of the assembly schema spheres of steel in its bracket, b) TR-Bio 282 pin-on-flat reciprocatory DUCOM tribometer of the Applied Mechanics Lab of the Department of Industrial Engineering – University of Salerno – , c) and d) the assembly of the pin and flat in the tribometer.

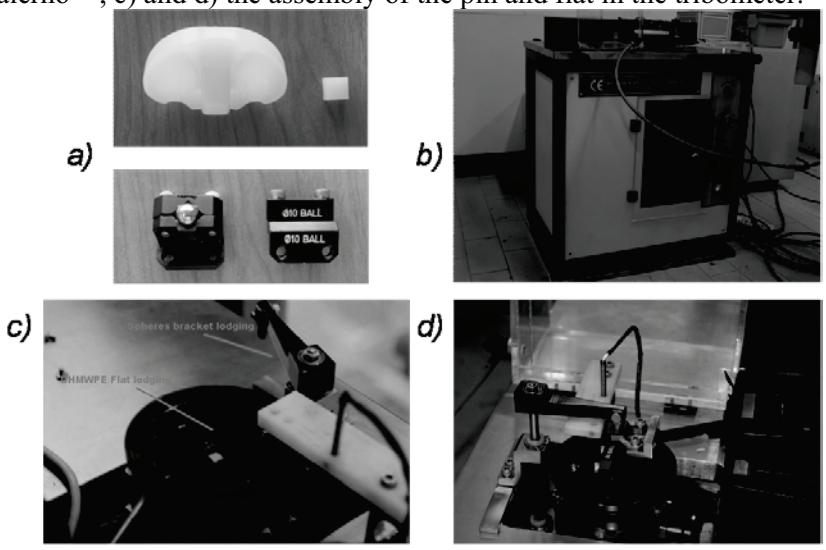

Figure III.26: *a) Polyethylene cuts and an sphere of steel in its holder, b) TR-Bio 282 DUCOM tribometer, c) and d) the assembly of pin-flat under operative condition.*

A pharmaceutical fluid, similar in consistency and in the properties to normal synovial fluid, called *Hyalgan*® was chosen for the test in lubricated conditions. This one contains a large amount of sodium hyaluronate and it is used as intra articular injection in arthritic joints induces a normalization of the viscoelasticity of the synovial fluid and an activation of tissue repair processes at the level of the articular cartilage [176].

III.7.2.2 Tribological tests

Reciprocatory pin-on-flat friction tests have been carried out at controlled room temperature and humidity (T=20ºC and H=55±5%). The parameters of the test that must be set are: frequency, time and load. In fact, the tribometer can apply a contact loads from 1 N to 20 N and it can operate within a wide range of frequencies from 5 Hz to 60 Hz. In this study, the selected frequency is 10 Hz to avoid vibrations of the plate and undesirable vertical motions, the chosen time is 120 minutes and the stroke used is 2 mm. Regarding the choice of the load to apply to the tribometer, we must keep in mind that the materials selected for testing come from knee prosthesis. Cerniglia et al. [177] in their study calculate that the contact force between the tibia and femur, during walking, is equal to three times the weight of the human body. By considering the human body weight P = 70 kg, the calculated normal load will be about 2000 N. In another experimental study, Zach et al. [178] calculate, through a FEM analysis and the using of pressure sensitive film, the contact area between two given bone elements for several loading forces. In our case, a load of 2000 N corresponds to a value in the contact area equal to 75,8 mm^2 [178]. Contact pressure to be used to calculate normal loads for different pins' diameters to be employed in tribological test will be $p = \frac{2000(N)}{75.8(mm^2)} = 27MPa$. Therefore, by using the Hertz's contact theory it is possible to calculate the applied normal load for each kind of materials and for each kind of sphere diameters. As known, it is the case to underline that by using Hertz theory, the error for small curvatures (conforming contact) is notable because of the Hertz assumption that the contact area is small with respect to component dimensions. The error for nonconforming contact (our case) is due to the nonlinear behavior of the UHMWPE. Agreement, where it occurs, seems to be due to a coincidental combination of the two effects (conformity and nonlinear material behavior). Therefore, although the Hertz theory is generally not applicable for the study of polyethylene stresses, in our case, the main purpose of the use of Hertz theory is the assessment – not the evaluation of an exact value – of a typical normal load to be applied to the investigated tribo-system. Considering that typically, the contact pressure in prosthesis is largely variable, the calculation of the contact stress during testing, based on Hertzian ball-on-flat contact mechanics, could be accurate in many cases [179].

As the tribometer provides an implementation system of the applied load with a weight variation of 0.5 kg, the calculated values for the applied normal loads in the tests were approximated as shown in **Table III.3**.

Table III.3: *Diameter Spheres and Normal load for each kind of materials*

Pin Materials	Diameter Spheres (mm)	Calculated Normal Load (N)	Imposed Normal Load (N)
TiAl6V4	3	1.006	1
	6	4.019	4
AISI 316L	3	1.021	1
	6	4.055	4
	10	11.231	11
Al_2O_3	3	1.011	1
	6	4.037	4
	10	11.181	11

About the evaluation of wear mass loss, it has not been possible to evaluate it with gravimetric methods by using a balance with an available accuracy of 0.1 mg. Therefore, with the purpose of comparing the wear rates of the three tribological pairs under study, the worn surfaces of the UHMWPE specimens, after the tests, were analysed by 3D Optical Surface Metrology System Leica DCM 3D of the LIMIT Lab at the ETSIDI –Technical University of Madrid, only in the case in which the pins' diameter was of 6 mm. By knowing the density of UHMWPE (0.93 g/cm^3) [21], it was possible to estimate the wear mass loss by measuring the groove volume left by the pin on the specimens during the tests. For the tests carried out under lubricated conditions it was no possible to evaluate the wear mass loss because, as it will be detailed in results section, most of tests have led to the breaking of the lubricant fluid film on both the UHMWPE samples (A and B).

III.7.3 Results

III.7.3.1 Tribological test under dry conditions

The **Figure III.27**, **Figure III.28** and **Figure III.29** show the evolution of the friction coefficients during the test under dry condition in the TiAl6V4-UHMWPE, AISI316L-UHMWPE and Al_2O_3-UHMWPE respectively.

a)

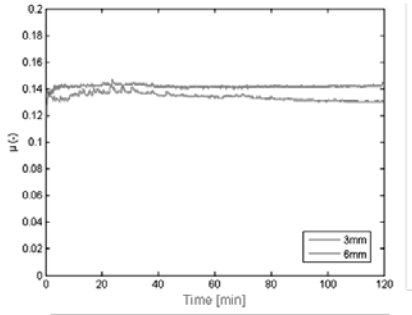

Diameter [mm]	μ	STD	μ_r	STDr
3	0.141	0.0037	0.142	0.0035
6	0.133	0.0039	0.134	0.0028

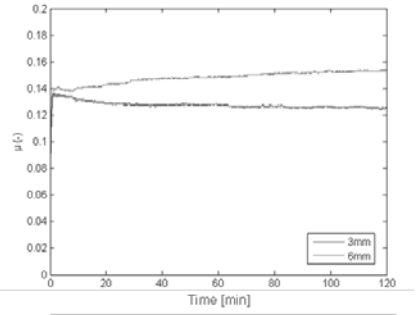

Diameter [mm]	μ	STD	μ_r	STDr
3	0.127	0.0042	0.127	0.00098
6	0.147	0.0065	0.149	0.0028

b)

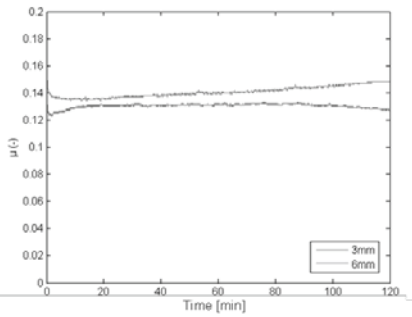

Diameter [mm]	μ	STD	μ_r	STDr
3	0.129	0.0028	0.131	0.0011
6	0.139	0.0047	0.142	0.0035

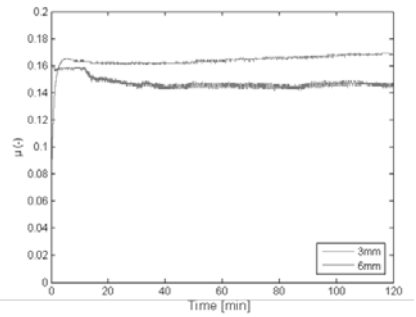

Diameter [mm]	μ	STD	μ_r	STDr
3	0.147	0.0048	0.146	0.0015
6	0.164	0.0067	0.165	0.0024

Figure III.27: *The evolution of the friction coefficient under dry conditions in: a) TiAl6V4-UHMWPE sample "A" contact, b) TiAl6V4-UHMWPE sample "B" contact.*

a)

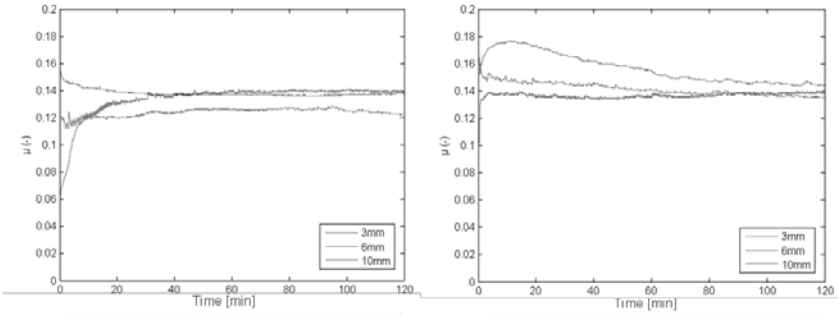

Diameter	μ	STD	μr	STDr
3	0.135	0.0073	0.138	0.0025
6	0.122	0.0094	0.125	0.0019
10	0.18	0.0037	0.137	0.00073

Diameter	μ	STD	μr	STDr
3	0.137	0.0038	0.137	0.0015
6	0.141	0.0051	0.141	0.0034
10	0.156	0.011	0.153	0.0082

b)

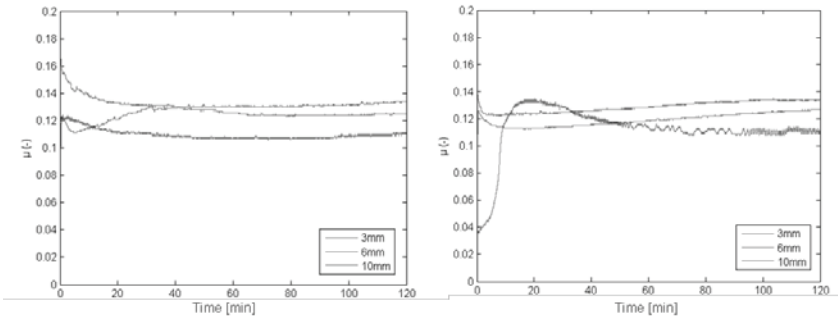

Diameter	μ	STD	μr	STDr
3	0.111	0.0042	0.109	0.0013
6	0.132	0.0051	0.131	0.0011
10	0.124	0.0051	0.126	0.0021

Diameter	μ	STD	μr	STDr
3	0.112	0.0187	0.115	0.0071
6	0.129	0.0045	0.131	0.0034
10	0.119	0.0055	0.121	0.0043

Figure III.28: *The evolution of the friction coefficient under dry conditions in: a) AISI316L -UHMWPE sample "A" contact, b) AISI316L - UHMWPE sample "B" contact.*

a)

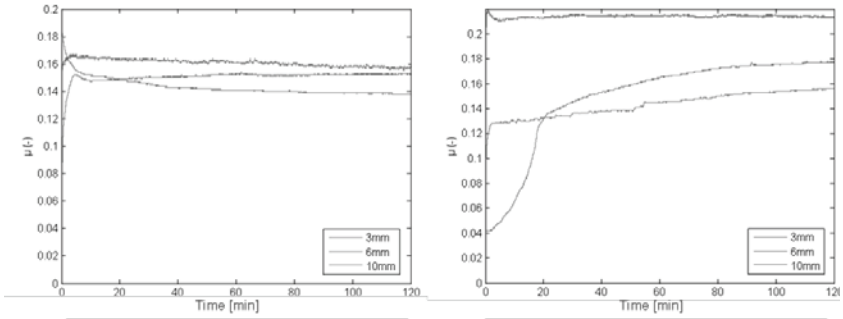

Diameter	μ	STD	μr	STDr
3	0.161	0.0041	0.161	0.0021
6	0.151	0.0061	0.151	0.0011
10	0.143	0.0066	0.141	0.0026

Diameter	μ	STD	μr	STDr
3	0.211	0.0047	0.214	0.0007
6	0.149	0.038	0.165	0.012
10	0.143	0.0099	0.146	0.0074

b)

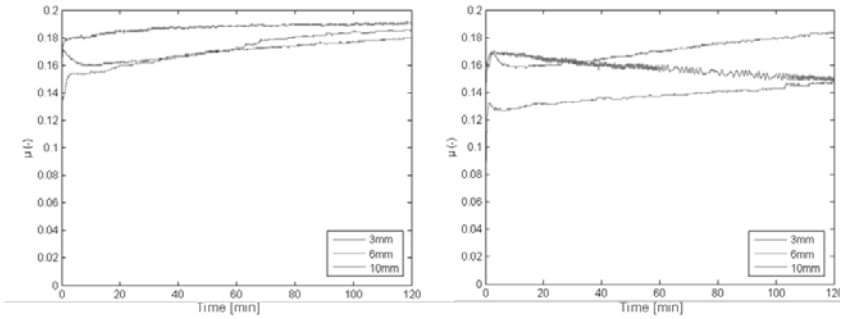

Diameter	μ	STD	μr	STDr
3	0.187	0.0052	0.188	0.0017
6	0.171	0.0088	0.172	0.0052
10	0.176	0.0093	0.168	0.0054

Diameter	μ	STD	μr	STDr
3	0.158	0.0067	0.156	0.0044
6	0.171	0.0088	0.172	0.0072
10	0.137	0.0068	0.139	0.0044

Figure III.29: *The evolution of the friction coefficient under dry conditions in: a) Al2O3 -UHMWPE sample "A" contact, b) Al2O3-UHMWPE sample "B" contact.*

There are two pairs of graphs for each figure. The first one is for the rubbing contact against UHMWPE sample "A" for two tests under same working conditions (Figs.a), and the second one for the rubbing contact against UHMWPE sample "B" for two tests under same working conditions (Figs.b). Under each graph a summary of the results for the mean values of the friction coefficient and its standard deviation in continuous (μ, *STD*) and after the initial transient (first 20 minutes) is shown (μ_r, STD_r). The friction coefficients of all rubbing pairs were low at the initial stage, but rapidly increased and stabilized with time sliding. No immediate correlation can be identified between the pins' diameters (loads) and the friction coefficients. **Figure III.30a** and **b** show the histogram of the friction coefficients in all rubbing pairs for the UHMWPE sample "A" and for UHMWPE sample "B" respectively. It is possible to note that in each test, the maximum value of the friction coefficient corresponds to the couple Al_2O_3-UHMWPE.

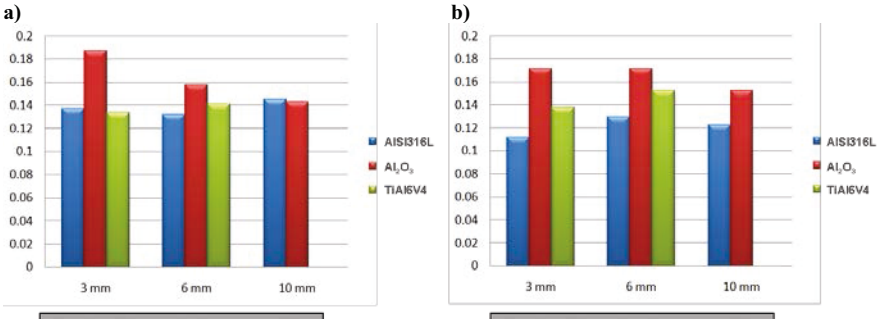

Material	Diameter [mm]	μr	STDr
TiAl6V4	3	0.134	0.0022
	6	0.141	0.0028
AISI316L	3	0.137	0.0021
	6	0.132	0.0026
	10	0.145	0.0077
Al_2O_3	3	0.187	0.0013
	6	0.158	0.0011
	10	0.143	0.0051

Material	Diameter [mm]	μr	STDr
TiAl6V4	3	0.138	0.0013
	6	0.153	0.0029
AISI316L	3	0.112	0.0041
	6	0.131	0.0022
	10	0.123	0.0031
Al_2O_3	3	0.172	0.0031
	6	0.172	0.0062
	10	0.153	0.0049

Figure III.30: *Average values of the friction coefficient for each kind of materials under dry conditions in contact with: a) UHMWPE sample "A", b) UHMWPE sample "B".*

This effect is probably due to its high hardness and its wear resistance properties [36], [37]. **Figure III.31** shows the qualitative analysis of the UHMWPE surfaces (samples A) after the test under dry conditions for pins' diameter of 6mm in the case of materials of pins were: a) TiAl6V4; b) AISI316L; c) Al_2O_3. After a metrological characterization of the worn surfaces during the tribological tests, it was possible to calculate the groove volume left by the pin on the UHMWPE samples. **Table III.4** shows the results for the wear mass loss for each kind of tribological couple.

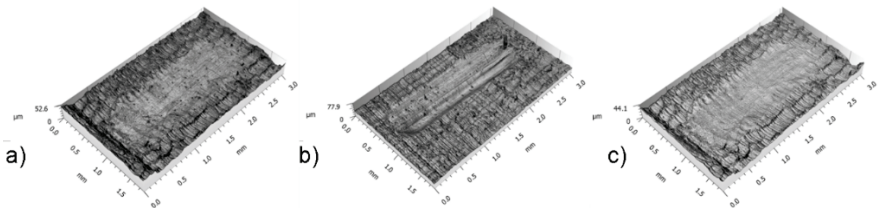

Figure III.31: *3D Optical Surface Metrology System Leica DCM 3D and qualitative analysis of the UHMWPE (samples A) surfaces after the test under dry conditions for pins' diameter of 6mm in the case of: a) TiAl6V4; b) AISI316L; c) Al2O3.*

Table III.4: *The wear mass loss in the test under dry conditions for pins' diameter of 6mm in UHMWPE samples A*

Tribological Pair	Groove Volume (mm^3)	Wear mass loss (g)
TiAl6V4-UHMWPE	$0.79*10^{-2}$	$0.74*10^{-5}$
AISI316-UHMWPE	$0.61*10^{-2}$	$0.57*10^{-5}$

Table III.4: *The wear mass loss in the test under dry conditions for pins' diameter of 6mm in UHMWPE samples A*

Tribological Pair	Groove Volume (mm^3)	Wear mass loss (g)
Al_2O_3-UHMWPE	$1.02*10^{-2}$	$0.95*10^{-5}$

From the analysis of results, congruence between the value of the wear mass loss and the friction coefficient can be easily inferred. In fact, for the pins' diameter of 6 mm, a maximum value of the friction coefficient corresponds to a maximum value of the wear mass loss (**Table III.4**) followed by TiAl6V4 and ultimately by AISI316. Through the observing of the UHMWPE worn surfaces samples in all rubbing pairs, plastic deformations producing grooves aligned with sliding direction were found. Probably, these phenomena are due to adhesive wear mechanisms.

III.7.4 Tribological test under lubricated conditions

Figure III.32, **Figure III.33** and **Figure III.34** show the evolution of the friction coefficients during the test under lubricated conditions in the contacts AISI316L-UHMWPE, TiAl6V4-UHMWPE and Al_2O_3-UHMWPE respectively. Obviously, the introduction of the lubricating fluid tends to decrease the values of the friction coefficient. In contrast to the dry tests, the graphs show that the phase of initial transient expires after 10 minutes after which it remains for a time that varies depending on the conditions of each test. Only in two tests, the friction coefficients remain stable after the initial transient for all pins' diameter: TiAl6V4-UHMWPE sample "B" (**Figure III.32b**) and Al_2O_3-UHMWPE sample "B". In the contacts TiAl6V4-UHMWPE sample "A" (**Figure III.32a**), AISI316L-UHMWPE (**Figure III.33a** and **b**) and in Al_2O_3-UHMWPE sample "A" (**Figure III.34a**) the lubricant meatus breakage occurs by causing an increase of the value of the coefficient of friction for the pins' diameters: 3 mm, 6 mm and 10 mm respectively. Notably, such a phenomenon occurs because of the viscosity of the lubricant which, if added to a combination of applied loads and set speeds, might cause distinct and several lubrication mechanisms such as boundary or transient lubrication. Consequently, such a critical inquiry needs future experimental developments.

a)

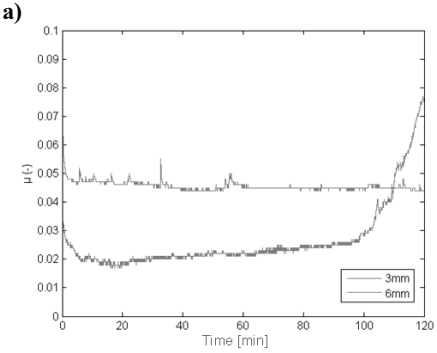

Diameter	μ	STD	μ_r	STD_r
3	0.266	0.0117	0.0221	0.0023
6	0.465	0.0017	0.0454	0.0011

b)

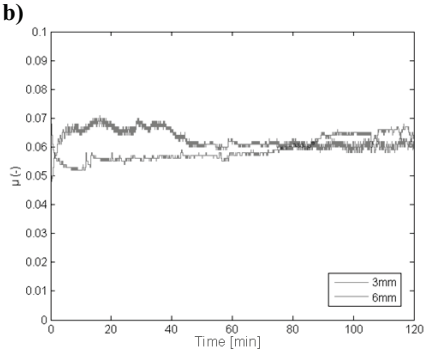

Diameter	μ	STD	μ_r	STD_r
3	0.0625	0.0036	0.0626	0.0031
6	0.0589	0.0041	0.0593	0.0038

Figure III.32: *The evolution of the friction coefficient under lubricated conditions in: a) TiAl6V4-UHMWPE sample "A" contact, b) TiAl6V4-UHMWPE sample "B" contact*

a)

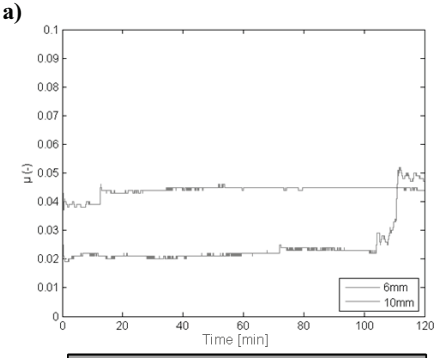

Diameter	μ	STD	μr	STDr
6	0.0241	0.0074	0.0218	0.0012
10	0.0441	0.0019	0.0441	0.0011

b)

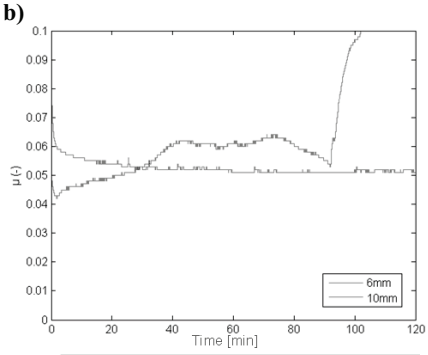

Diameter	μ	STD	μr	STDr
6	0.0586	0.029	0.0574	0.0051
10	0.0527	0.0024	0.0521	0.0011

Figure III.33: *The evolution of the friction coefficient under lubricated conditions in: a) AISI316L -UHMWPE sample "A" contact, b) AISI316L -UHMWPE sample "B" contact*

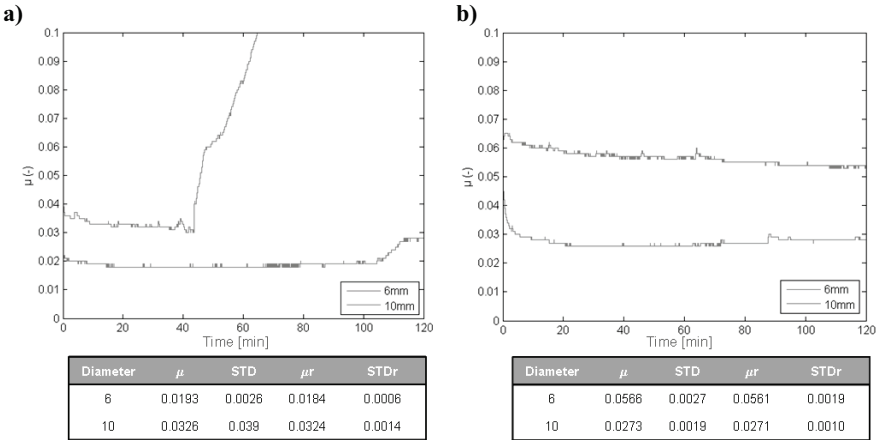

Diameter	μ	STD	μr	STDr
6	0.0193	0.0026	0.0184	0.0006
10	0.0326	0.039	0.0324	0.0014

Diameter	μ	STD	μr	STDr
6	0.0566	0.0027	0.0561	0.0019
10	0.0273	0.0019	0.0271	0.0010

Figure III.34: *The evolution of the friction coefficient under lubricated conditions in: a) Al2O3 -UHMWPE sample "A" contact, b) Al2O3-UHMWPE sample "B" contact*

For this reason, the average values of the friction coefficient and its standard deviation in steady operation, shown in the histograms of **Figure III.35**, were calculated between 10 and 110 minutes in the contact TiAl6V4-UHMWPE sample "A" with a pin diameter of 3mm (**Figure III.32a**). In the contact AISI316L-UHMWPE sample "A" with a pin diameter of 6 mm (**Figure III.33a**) the friction coefficient and its standard deviation in steady operation were calculated between 10 and 105 minutes, whereas they were evaluated between 10 and 90 minutes in the contact AISI316L-UHMWPE sample "B" with a pin diameter of 6 mm (**Figure III.33b**). Ultimately, the friction coefficient and its standard deviation in steady operation were estimated between 10 and 40 minutes in the contact Al_2O_3-UHMWPE sample "A" with a pin diameter of 10 mm (**Figure III.34a**) and between 10 and 110 minutes in the contact Al_2O_3-UHMWPE sample "A" with a pin diameter of 6 mm (**Figure III.34b**).

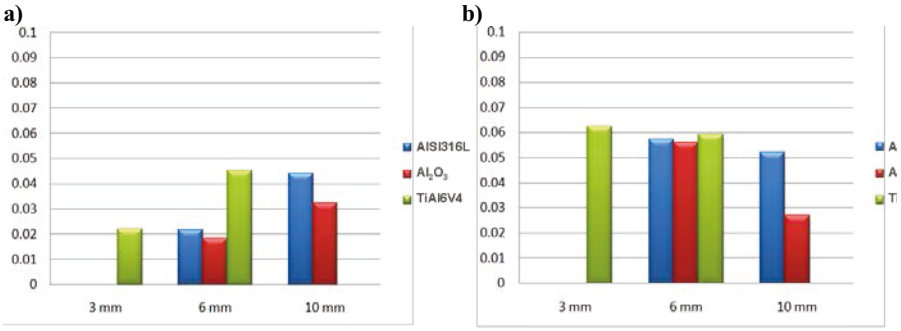

Material	Diameter [mm]	μr	STDr
TiAl6V4	3	0.0221	0.0023
	6	0.0454	0.0011
AISI316L	6	0.0218	0.0012
	10	0.0441	0.0011
Al_2O_3	6	0.0184	0.0006
	10	0.0324	0.0014

Material	Diameter [mm]	μr	STDr
TiAl6V4	3	0.0626	0.0031
	6	0.0593	0.0038
AISI316L	6	0.0574	0.0051
	10	0.0521	0.0012
Al_2O_3	6	0.0561	0.0019
	10	0.0271	0.0010

Figure III.35: *Average values of the friction coefficient for each kind of materials under lubricated conditions in contact with: a) UHMWPE sample "A", b) UHMWPE sample "B".*

III.7.5 Conclusion

In this work a tribological experimental study was performed to obtain the friction coefficients of UHMWPE against TiAl6V4 alloy, against AISI316L steel and against Al_2O_3. The tests were performed under dry and lubricated conditions. As lubricants, the Authors used a commercial drug containing the sodium hyaluronate fluid: Hyalgan®. Tests were conducted by using a reciprocating pin on flat tribometer with several load conditions for 120 minutes. The loads have been chosen considering the actual pressure and using the Hertz's Theory for all the three materials. The flat specimens have been cut, cleaned and prepared by two different knee prostheses. The differential scanning calorimetry (DSC) has been employed to compare the two UHMWPE samples.

The results of the tribological performances show that the AISI316L austenitic stainless steel and TiAl6V4 alloy yield lower values in the friction coefficient – and in frictional forces – under dry conditions. Findings are aligned with those involved in the analysis of the worn surfaces at the microscope and with the subsequent evaluation of the wear mass loss (**Table III.4**). When the friction coefficient is monitored along larger time under dry conditions it increases quickly independently of the pair and of the loading conditions. The increasing rate is not reproducible as well as the final value of the friction coefficient, which normally stays in the range 0.11–0.18 after a sliding time larger than 20 min (**Figure III.27a**, **Figure III.28a** and **Figure**

III.29a). Low values of the friction coefficient are ascribable to the UHMWPE transfers to the counter face that mould a polymeric film as self-lubricant [180]. As expected, in all tests under lubricated conditions the friction coefficient was much lower than in dry-sliding conditions. The final value of the friction coefficients for the tests carried out under lubrication varied in the range 0.018–0.06 after a sliding time larger than 10 mins, independently of the pair and the loads (**Figure III.32b**, **Figure III.33b** and **Figure III.34b**).

III.8 Metal Transfer: roughness characterization

In this section it will be shown the results of a roughness investigation on 35 retrieved ceramics femoral heads with evidence of metallic dark lines. Roughness values were acquired using both a stylus contact profiler and an optical non-contact profilometer. This section is extracted from the article "*On the tribological behavior of retrieved hip femoral heads affected by metallic debris. A comparative investigation by stylus and optical profilometer for a new roughness measurement protocol*" published on the journal Measurement 90 in 2016 (pages 365-371), authors: Massimiliano Merola, Alessandro Ruggiero, Jonathan Salvatore De Mattia and Saverio Affatato.

III.8.1 Aim

Aim of this study was twofold:

- validate a new protocol to measure surface roughness on retrieved femoral heads, by using two different acquisition techniques;
- investigate the hypothesis that such metal transfer retrieved ceramic femoral head is associated with increased surface roughness.

III.8.2 Materials and Method

III.8.2.1 Process of selection

Ceramic femoral heads were explanted during revision arthroplasty at our institution (Rizzoli Orthopaedic Institute, Bologna, Italy) and catalogued in a Register of Orthopaedic Prosthetic Explants (REPO). All patients in this study gave their informed consent. Two independent observers (JSDM and SA) with experience in evaluating damage on ceramic implants qualitatively assessed the patterns of damage on the retrieved femoral heads, selecting only the components with evidence of MT (a picture of this phenomenon is shown in **Figure III.36**).

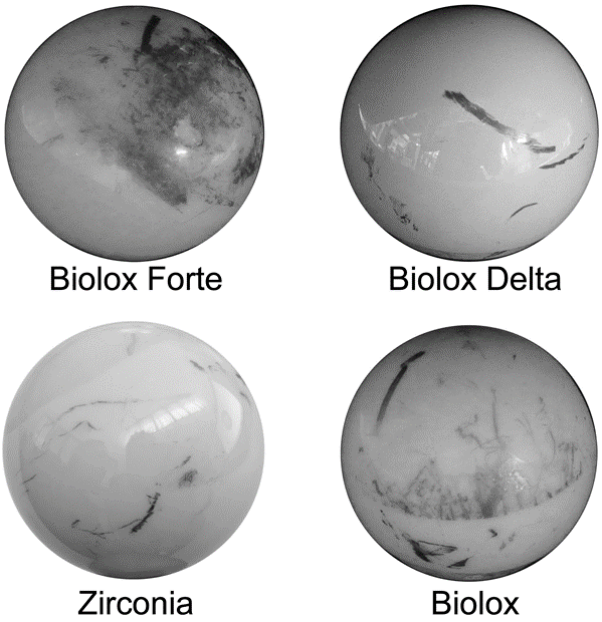

Figure III.36: *Four femoral head of ceramic materials affected by MT.*

35 ceramics femoral heads were selected including five zirconia femoral heads (removed from five patients after a mean of 6.6 years in situ), 18 Biolox® Delta femoral heads (removed after a mean of 2.3 years in situ), 6 Biolox® and 6 Biolox® Forte femoral heads (explanted after a mean of 13.5 and 5.2 years, respectively). The femoral heads were cleaned by submersion in an enzymatic detergent and wiped with acetone before being observed. Major details are shown in **Table III.5**.

Table III.5: *Patients details sorted by increasing follow-up.*

Sample Number	Gender	Follow Up (years)	Implant Side	Material	Age at Surgery
PZ_14	M	0.1	Right	Biolox®	74
PZ_15	M	0.1	Right	Biolox®	56
PZ_20	M	0.1	Left	Biolox®	83
PZ_22	M	0.1	Right	Biolox®	78
PZ_27	M	0.1	Left	Biolox®	70
PZ_17	F	0.2	Right	Biolox®	61
PZ_23	F	0.2	Left	Biolox®	77
PZ_24	M	0.2	Right	Biolox®	49
PZ_18	F	0.4	Right	Biolox®	67
PZ_26	M	0.5	Right	Biolox®	68
PZ_28	F	1	Right	Biolox®	72
PZ_13	M	1.2	Left	Biolox®	78
PZ_21	M	1.3	Left	Biolox®	48
PZ_25	M	1.6	Right	Biolox®	67

Table III.5: *Patients details sorted by increasing follow-up.*

Sample Number	Gender	Follow Up (years)	Implant Side	Material	Age at Surgery
PZ_29	M	1.9	Left	Biolox®	56
PZ_19	F	2.4	Right	Biolox®	62
PZ_32	M	3.1	Right	Zirconia	59
PZ_16	M	3.7	Right	Biolox®	69
PZ_4	F	4	Right	Biolox®	35
PZ_31	F	4.6	Left	Zirconia	67
PZ_30	F	5.4	Right	Biolox®	68
PZ_12	F	6.6	Right	Biolox®	61
PZ_34	F	6.6	Right	Zirconia	63
PZ_8	F	6.7	Left	Biolox®	27
PZ_33	M	6.8	Left	Zirconia	65
PZ_11	F	7.6	Right	Biolox®	59
PZ_7	M	9.1	Left	Biolox®	61
PZ_9	M	10.2	Right	Biolox®	61
PZ_6	F	10.5	Left	Biolox®	48
PZ_35	M	11.9	Right	Zirconia	56
PZ_2	M	12.5	Left	Biolox®	53
PZ_3	M	14.9	Left	Biolox®	54
PZ_1	F	16.7	Right	Biolox®	58
PZ_10	M	19.8	Right	Biolox®	67
PZ_5	F	22.1	Right	Biolox®	64

III.8.2.2 Surface roughness characterization

The surface roughness and topographic analyses were performed on all the retrieved specimens. To allow comparison, two areas of interest were selected: a portion of surface affected by the MT phenomenon ("Affected Area") and a portion of surface without the presence of MT ("Unaffected Area"). For both Affected and Unaffected Areas the topography acquisition was focused on a surface of 2.25 mm^2 (1.5 mm x 1.5 mm).

To characterize the roughness of the specimens, four main indicators were considered: S_a, S_t, S_{sk} and S_{ku} (described in **section III.4.2**).

Roughness analyses were performed by two different operators using two different techniques. The post-process procedure followed the same procedure by applying the Gaussian filter (ISO 11562:1996) on the entire area of 2.25 mm^2. The λ_c, cut-off sample length, was chosen according to the ISO 3274:1996 standard, and corresponded to 0.25 mm. The direct contact roughness measurement, was performed using a contact profilometer Hommel Tester T8000 machine (Hommel Werke, Luedinghausen, Germany) following a consolidated protocol [138], [167]:

- diamond stylus tip (radius 0.020 mm);
- tracing length of 1.5 mm;

- travel speed of 0.15 mm/s;
- resolution of 10 nm.

The 3D topographic surface acquisitions were performed using a PLu Neox profilometer (Sensofar, Terrassa, Spain), which collects three-dimensional images, operating either as confocal microscope or white light interferometer, with a resolution of less than 1 nm. A confocal objective, with 20× magnifications, was selected, with an acquisition length – along the Z-axis – equal to 100 µm. The acquisition's process followed an established procedure [181]. An interpolated tracking of the focus was selected for the stitching procedure, which was necessary due to the roundness of the surfaces. All the specimens underwent the same preparation: before the acquisition, the surface was cleaned with acetone and dried in a controlled ambient, at room temperature.

III.8.2.3 Statistical analysis

The measured roughness values were analysed using a nonparametric Mann-Whitney (M-W) test and a least significance difference as post hoc test. Statistical significance was set at $P < 0.05$. The analyses were, at first, performed comparing the unaffected *vs.* affected zones for each ceramic material and for both contact and optical method of acquisition. To assess the agreement of the two procedures of measurement, the statistical analysis, was performed comparing contact *vs.* optical roughness results.

III.8.3 Results

In **Figure III.37**, two topographical images are shown, as exemplificative results obtained through the 3D optical profilometer. In this picture**,** the Biolox Delta #4434 femoral head is considered. Differences in surface characteristic appear, as an evidence of the MT phenomenon, between the Affected and Unaffected areas.

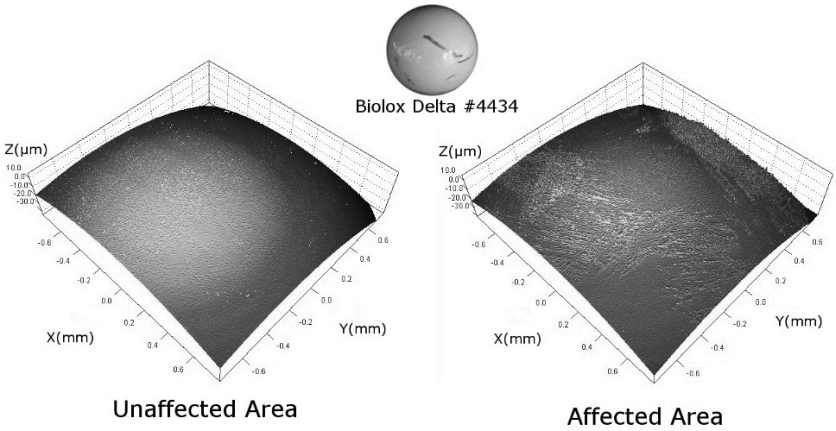

Figure III.37: 3D *topographies of a Biolox Delta femoral head. Evidences of MT phenomenon are visible in the right topography.*

In **Figure III.38**, a summary of the roughness analysis results is shown, presenting a histogram for each roughness parameter. Each bar indicates the mean value of all the measures obtained on the specimens belonging to a single ceramic material. These values were evaluated in the Affected and Unaffected areas for both optical (dashed bars) and contact (blank bars) techniques. These results confirmed the expected divergence for the roughness mean values in the affected and unaffected zones. Some differences between the values obtained from the two described methods were also found. This variance appears more evident for the S_t, S_{sk} and S_{ku} parameters. As expected, and already mentioned [143], the confocal microscope technique gained larger values. The huge dissimilarity for the S_t and S_{ku} parameters acquired on the Biolox heads can be ascribed to the limited number of samples available. In this case, it is worth noting that the main dissimilarities are found on the Affected areas.

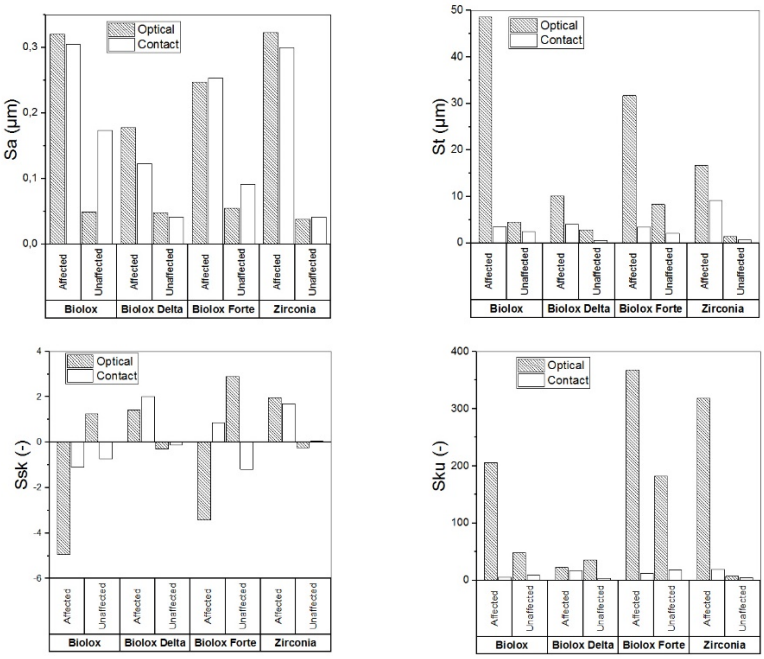

Figure III.38: *Summary of the roughness analysis results is shown, presenting a histogram for each roughness parameter.*

III.8.3.1 Statistical results

Results of nonparametric Mann-Whitney (M-W) test for affected ***vs.*** unaffected areas for each ceramic head category are shown in **Table III.6**. These results show how the two different techniques can differentiate between MT affected areas and pristine areas. In details, regarding Biolox® samples the contact technique cannot effectively detect differences between the areas, while with respect to Biolox® Forte samples differences stand out only through the parameter Sa. Overall, cases of statistical significance mainly relate to the optical technique even though as regards Zirconia samples both techniques highlight remarkable differences with regard to all measured parameters.

Table III.6: *Results of Mann-Whitney test for unaffected vs. affected areas. Cases with significant differences in distribution are highlighted in bold.*

Ceramic material	CONTACT				OPTICAL			
	Sa	**St**	**Ssk**	**Sku**	**Sa**	**St**	**Ssk**	**Sku**
Biolox	.180	.180	.699	.818	**.002**	**.002**	.180	.310
Biolox Delta	**.002**	**.000**	**.000**	**.000**	**.000**	**.000**	**.004**	.265
Biolox Forte	**.026**	.240	.132	.485	**.004**	**.041**	.240	.818
Zirconia	**.016**	**.016**	**.016**	**.032**	**.016**	**.016**	**.016**	**.032**

Table III.7*: Results of Mann-Whitney test for contact vs. optical acquisition method. Cases with significant differences in distribution are highlighted in bold.*

Ceramic material	UNAFFECTED				AFFECTED			
	Sa	**St**	**Ssk**	**Sku**	**Sa**	**St**	**Ssk**	**Sku**
Biolox	.065	.240	.180	.240	1.000	**.002**	.589	.065
Biolox Delta	**.008**	**.000**	.171	**.000**	**.033**	**.000**	.393	.426
Biolox Forte	.485	**.009**	.093	**.004**	.818	**.002**	.394	**.026**
Zirconia	1.000	.056	.151	.095	1.000	.486	1.000	.486

In **Table III.7** the results of the M-W tests for contact ***vs.*** optical method are shown.

In both Affected and Unaffected areas the S_a distribution yields a good agreement, except for the Biolox Delta samples. S_t distribution is the most influenced by the roughness acquisition technique, thus producing two results in the unaffected case and three in the affected one. S_{sk} distribution appears to have no substantial differences. In the end, S_{ku} distribution brought significant differences for the Biolox Forte in both Affected and Unaffected cases and for the Biolox Delta in the Unaffected one.

III.8.4 Discussion

Wear complications remain a major cause of revision following THA, and the surface roughness of the prosthetic femoral head plays an important role

in generating polyethylene wear debris after total hip arthroplasty [31]. Metal transfer has been observed on retrieved femoral head components and it is well known that the adherence of third-body particles to the femoral head increases its surface roughness [117]. MT today remains a concern because some studies have correlated this phenomenon with an increase in the surface roughness of femoral heads and this results in an increased wear rate of the conventional polyethylene counterface [182], [183]. An increase in surface roughness and wear as a result of transferred metal debris may be an explanation for the sporadic cases of excessive wear of alumina-on-alumina bearings [184].

In the current study, we inquire whether metal transfer observed on 35 retrieved alumina femoral heads was associated with changes in the surface roughness. The findings of our study confirmed the hypothesis that a visual dark metallic smear on ceramics femoral heads correlates with increased surface roughness, about the S_a and S_t parameters. The statistical analysis showed dissimilarities for most roughness parameters' distribution in the comparison between affected ***vs***. unaffected areas. Neither the contact nor the optical technique gained a trend for the S_{sk} term. S_{ku} parameter led to mean values always higher than 3, for every ceramic material. About the optical *vs.* contact acquisition technique comparison (**Table III.7**), the M-W Test highlights that no deviation was found for S_{sk} parameter, showing that statistical significance (*p-value*) always exceeds the threshold value 0.05.

Eberhardt et al. [185], analysing CoCr and ZrO_2 Femoral Heads, found R_a values of an order of magnitude greater than the control values, whereas R_{sk} values were negative for control heads and positive for the transfer specimens. Kim et al. [112] confirmed the hypothesis that a dark metallic smear on a ceramic femoral head correlates with increased surface roughness of the head and increased polyethylene wear. Despite improved scratch resistance of ceramic-bearing surfaces [186], irregularities introduced by metallic deposition after recurrent dislocation can damage a highly cross-linked polyethylene liner. It has also been highlighted that surface roughness affects wear rates and lubrication mechanism in total artificial joints [187]–[189].

Obviously, this study has some limitations due to the small number of Biolox® and zirconia femoral heads. Overall, this study confirmed that femoral components show substantial differences as regards the roughness characteristic on the areas affected by metal transfer and the unaffected areas. The two acquisition procedures confirmed a satisfying agreement, even considering the obvious resolution difference. The roughness profile of ceramic hip femoral heads' surface is characterized by a very smooth profile, with not too pronounced peaks and valleys, except for sporadic cases of excessive wear. This is a characteristic inherently due to the type of material and the type of application which ceramic femoral heads are designed for. In this context, the use of optical techniques to acquire micro-morphological

features allows for more accurate measurements [185]. However, S_a and S_{sk} distribution showed the same trend for the two aforementioned techniques.

III.8.5 Conclusions

This study has investigated two useful techniques to analyse the surfaces roughness of MT-affected hip femoral heads, offering additional knowledge for the choice of the best technique in analysing the surface roughness. Understanding the morphology of metal transfer may help to realistically re-create metal transfer effect using hip joint simulators, and to determine the relationships between surface characteristics and patients' variables.

Further studies are needed to better understand the morphology of metal transfer not only from the surface roughness point of view but also to determine the relationships between patients' characteristics as for shape, position, cause and amount of MT on hip femoral heads.

III.9 Metal Transfer on three Biolox® generations

In this section it is presented a study on the metal transfer, investigating its dependency on the femoral head material. This section is extracted from the article "*Does Metal Transfer Differ on Retrieved Biolox® Delta Composites femoral heads? Surface Investigation on three Biolox® generations from a biotribological point of view*" published on the journal Composites Part B: Engineering 113 in 2017 (pages 164-173), authors: Saverio Affatato, Alessandro Ruggiero, Massimiliano Merola, Silvia Logozzo.

III.9.1 Introduction and Aim

Previous studies about MT characterization consisted of visual observations, semi quantitative scoring, and surface roughness measurements [112], [113], [185], [190]. To the authors' knowledge, no more reports are available in literature about "general grading system" of metal transfer on AMC bearing surfaces. Chen and co-workers [191] proposed a "subjective grading system" to better assess the metal transfer on retrieved hip ceramics. Elpers et al. [192] graded each head of the 27 ceramic Delta studied, based on the number of distinct occurrences of metal transfer, the intensity, and the surface area of the femoral head involved. Even though these studies raised some relevant issues about metal transfer in THA, they don't provide an objective way to classify MT patterns. Affatato and co-workers [193] proposed a novel classification of MT taking into account the extension of this phenomenon.

The aim of this study was multiple:

1. propose a metrological technique to better characterize the MT phenomena on three generations of ceramic Biolox®;

2. compare the outcome of the MT on a novel composite material and on standard ceramic femoral heads used in hip arthroplasty;
3. investigate whether the MT extension (the areal coverage) on the femoral heads is correlated to the *follow-up* of the implants;
4. propose a new technique to better distinguish between MT and surgical signs due to surgical instruments during the revised operation.

III.9.2 Materials and methods

In this study the authors examined 24 retrieved femoral heads from three generation of ceramic heads: Biolox® Delta, Biolox® Forte and Biolox®. The Biolox® Delta is a composite of Zirconia Toughened Alumina (ZTA), the other two are Al_2O_3 based ceramics. Main physical and mechanical properties are summarized in **Table III.8**. These were removed from 24 patients, after a mean of 6.9 years *in situ* (range from 1.1 to 22.1 years). The patients had undergone a primary THA at our hospital (Rizzoli Orthopaedic Institute, Bologna-Italy) between 1990 and 2014; there were 12 women and 12 men with an average age of 60 years (ranging from 27 to 83) at revision. In most cases, the cause of failure was aseptic loosening of the acetabular component. Aseptic loosening of joint implants is a disabling condition that can affect patients and it can be the result of inadequate initial fixation, mechanical loss of fixation over time, or biologic loss of fixation caused by particle-induced osteolysis around the implant [194]. In this study, two independent observers (AR and SA), experienced in evaluating damage on ceramic implants, qualitatively assessed the patterns of damage on the retrieved femoral heads. To this purpose, the authors aim a classification for the MT phenomenon, based on the evaluation of the morphology of the MT area on the retrieved specimen as previously proposed [193]. The authors classified the MT phenomenon considering three different patterns:

1) "**Linear Scratch MT**": typical of specimens with single or multiple thin lines of MT with similar macro-directionality.

2) "**Areal MT**": typical of specimens accompanied by extended MT of undetermined pattern localized in a macro-area of the femoral head (including also multiple thin lines).

3) "**Stain MT**": typical of samples with MT distributed over a wide area of the head.

Table III.8: *Highlights on the three generation of ceramics.*

		Biolox®		**Biolox® Forte**		**Biolox® Delta**	
		mean	*variance*	*mean*	*variance*	*mean*	*variance*
Density	g/cm^3	3.95	0.23	3.97	0.00	4.37	0.01

Table III.8: *Highlights on the three generation of ceramics.*

		Biolox®		**Biolox® Forte**		**Biolox® Delta**	
		mean	*variance*	*mean*	*variance*	*mean*	*variance*
Grain dimension	µm	4	0.23	1.750	0.076	0.560	0.036
Young Modulus	GPa	410	1	407	1	358	1
Hardness HV	GPa	20	-	20	-	19	-
Flexion resistance	MPa	500	45	631	38	1384	67

III.9.2.1 3D shape acquisition and surface area calculation

To measure the MT extension on the femoral heads, a new set-up and procedure were implemented. The extension of MT was performed by using an innovative 3D optical non-contact scanner that gives the evaluation of percentage of surface covered by metal (hereinafter called "areal coverage") with respect to the entire surface of the retrieved femoral heads.

The scanner used in this research is Go!SCAN 20 by Creaform (Creaform Inc. - Lévis – Québec). This is a portable optical non-contact 3D scanner for a wide range of industrial applications, including metrology. Both resolution and accuracy are within 0.1 mm and it works according to the principles of structured light imaging, by projecting white QR coded light patterns on the scene. This device allows real time coloured 3D reconstructions. In this work, the 3D scanner was used exclusively to quantify the areal coverage of metal transfer and not to measure local differences in surface topography. The scanning procedure was performed by using three different types of positioning references: physical targets, virtual targets provided by surface's natural features and geometrical comparison frame by frame. The device was used to perform 3D coloured scanning of the femoral heads to detect the effective amount of metal transfer related to the different implant material.

Scanned models were processed by using mesh editing and 3D modelling software: 3D Systems – Geomagic Studio 2014.2.0 and Creaform – VXModel 4.0 SR1 2015. Before acquiring the 3D coloured model of the femoral heads, the femoral heads were wiped with acetone to remove any dust collected during storage. Subsequently, a proper setup was prepared by positioning physical targets on a black rotary table where the femoral heads could be put on and scanned. In the case of femoral heads, the physical targets were necessary as the geometry of the head is spherical and the texture of the surface has not enough characteristic features to allow the scanner to recognise the coloured pixels as natural targets. The targets were put on the rotary table

and not on the femoral head to avoid procedures of artificial reconstruction of textures operated by specific scanning algorithms. Therefore, the acquired coloured 3D digital model of any head represents its real surface. **Figure III.39** shows the setup with one of the scanned femoral heads. The targets on the surface of the head showed in **Figure III.39-b)** are not physical targets but virtual targets provided by the natural features of the texture of the head itself, while the whiter oval area in the reconstructed head image (**Figure III.39-d**) represents the base hole generated by trimming the sphere on a plane. In fact, as explained below, the mesh resulting from the scanning procedure was approximated as a perfect sphere, with the diameter of the fitting sphere equal to the nominal diameter of the femoral head. Then the sphere was trimmed by a base plane to reproduce the real shape of the head. The scanner can perform a real time 3D coloured reconstruction of the head's surface by acquiring 550000 measurements/s. Each frame can be captured at different focal points and digitally stacked to achieve an extended depth of field.

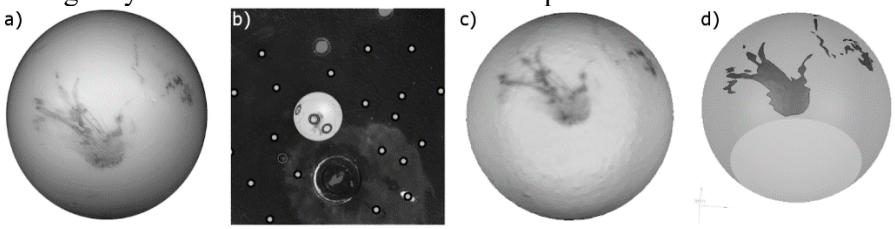

Figure III.39: *Set-up used to characterize the extension of metal transfer. Part a) original femoral head; Part b) physical and virtual targets; Part c) digital reconstruction of the femoral head; Part d) selection of the area affected by the Metal Transfer phenomenon*

After the acquisition, the 3D digital model of each head was processed according to the following steps:

1. The non-coloured mesh was optimised, as in common practice, by using isolated patches, spikes, noise and redundancy removing tools;
2. The colours were displayed onto the mesh and the MT areas were trimmed and separated from the rest of the mesh;
3. The rest of the mesh was approximated as a perfect sphere with the diameter of the fitting sphere equal to the nominal diameter of the femoral head. Then the sphere was trimmed to reproduce the real shape of the head.

The areas of MT on the femoral heads were calculated by using consolidate software algorithms.

III.9.2.2 Microscopic examination

Measurements of roughness and topography of the heads were taken from both worn and unworn areas using a non-contact profiler. The surface

acquisitions were performed using a PLu Neox profilometer (Sensofar, Terrassa, Spain), already described in **section III.8.2.2**. A confocal objective, with 20× magnifications, was selected. The acquisition length – along the Z-axis – was varied according to the surface curvature. Sampling lengths (tracing length 1.5 mm) were taken using a cut-off of 250 mm. All the specimens underwent the same preparation: before the acquisition, the surface was cleaned with acetone and dried in a controlled ambient, at room temperature according to a consolidated protocol [26], [138], [167], [195].

The area of interest was selected to cover not only the surface affected by the phenomenon but also a portion of the unaffected zone to permit comparison with reference values. For this analysis, three of the most used roughness parameters [167], [196], [197] were taken into account: S_a, S_t, S_{sk}, and S_{ku} (described in **section III.4.2**).

III.9.2.3 Surface characterization

Scanning electron microscope (SEM, ZEISS EVO 50EP, Cambridge, UK) operating at 20 kV was used to characterize the surface of the retrievals with evidence of MT. All the specimens were observed in an environmental pressure mode of 70–90 Pa in chamber, so there was no need for surface coatings. In addition, energy dispersive spectroscopy (EDS) X-ray analysis (Inca Energy-200, Oxford Instruments, UK) was used to analyse their chemical composition on all different ceramic heads in order to better characterize each element and so discriminate between MT and metal scars provoked by surgical instruments.

III.9.2.4 Statistical analysis

A statistical comparison between affected and unaffected areas was performed. Considering the complexity of the MT and its influence on roughness parameters, a Wilcoxon signed-rank test (matched pairs) was used to compare changes in the measures of roughness for both affected and unaffected surfaces. A difference was considered statistically significant at a p-value of < 0.05. Therefore, Pearson Correlation test was used to investigate the correlation ***i)*** between these roughness measurements and the *follow-up* and ***ii)*** between the percentage of area affected by MT (areal coverage) and the *follow-up* of the implant.

III.9.3 Results

None of the 24 ceramic heads analysed in this study had any gross damage or irregularity on the surface. MT varied widely across the bearings from the areas classified as *Linear Scratch* (n. 11 femoral heads) to the areas classified as *Areal* (n. 8 femoral heads), and the areas classified as *Stain* (n. 5 femoral heads). More details are shown in **Table III.9**.

Table III.9: *Selected patient details. The values are sorted by increasing values of metal transfer typology classification.*

Heads	*Years at Surgery*	*FU (years)*	*Gender*	*Implant Side*	*Material*	*MT Typology*	*Failure*
Pz_#01	*54*	*14.9*	*F*	*Right*	*Biolox®*	*Areal*	*Aseptic Loosening*
Pz_#04	*53*	*12.5*	*F*	*Right*	*Biolox®*	*Areal*	*Aseptic Loosening*
Pz_#11	*27*	*6.7*	*M*	*Right*	*Biolox® Forte*	*Areal*	*Periprostheti c Fracture*
Pz_#12	*59*	*7.6*	*F*	*Right*	*Biolox® Forte*	*Areal*	*Aseptic Loosening*
Pz_#13	*59*	*7.6*	*F*	*Right*	*Biolox® Forte*	*Areal*	*Aseptic Loosening*
Pz_#14	*62*	*2.4*	*F*	*Right*	*Biolox® Delta*	*Areal*	*Aseptic Loosening*
Pz_#15	*56*	*1.6*	*M*	*Right*	*Biolox® Delta*	*Areal*	*Aseptic Loosening*
Pz_#23	*61*	*2.1*	*F*	*Right*	*Biolox® Delta*	*Areal*	*Aseptic Loosening*
Pz_#02	*58*	*16.7*	*F*	*Right*	*Biolox®*	*Linear Scratch*	*Aseptic Loosening*
Pz_#03	*61*	*6.6*	*F*	*Left*	*Biolox®*	*Linear Scratch*	*Aseptic Loosening*
Pz_#05	*61*	*10.2*	*M*	*Left*	*Biolox®*	*Linear Scratch*	*Aseptic Loosening*
Pz_#08	*61*	*9.1*	*M*	*Left*	*Biolox® Forte*	*Linear Scratch*	*Stem fracture*
Pz_#09	*64*	*22.1*	*M*	*Left*	*Biolox®*	*Linear Scratch*	*Periprostheti c Fracture*
Pz_#10	*67*	*19.8*	*F*	*Right*	*Biolox® Forte*	*Linear Scratch*	*Aseptic Loosening*
Pz_#17	*78*	*2.8*	*M*	*Right*	*Biolox® Delta*	*Linear Scratch*	*Aseptic Loosening*
Pz_#18	*49*	*1.1*	*M*	*Right*	*Biolox® Delta*	*Linear Scratch*	*Aseptic Loosening*
Pz_#19	*68*	*1.2*	*M*	*Right*	*Biolox® Delta*	*Linear Scratch*	*Aseptic Loosening*
Pz_#22	*69*	*3.7*	*M*	*Right*	*Biolox® Delta*	*Linear Scratch*	*Aseptic Loosening*
Pz_#24	*77*	*1.1*	*F*	*Left*	*Biolox® Delta*	*Linear Scratch*	*Aseptic Loosening*
Pz_#06	*48*	*10.5*	*M*	*Right*	*Biolox® Forte*	*Stain*	*Aseptic Loosening*
Pz_#07	*35*	*4*	*F*	*Left*	*Biolox® Forte*	*Stain*	*Aseptic Loosening*
Pz_#16	*83*	*2.3*	*M*	*Left*	*Biolox® Delta*	*Stain*	*Aseptic Loosening*
Pz_#20	*56*	*1.9*	*M*	*Left*	*Biolox® Delta*	*Stain*	*Aseptic Loosening*

Table III.9: *Selected patient details. The values are sorted by increasing values of metal transfer typology classification.*

Heads	*Years at Surgery*	*FU (years)*	*Gender*	*Implant Side*	*Material*	*MT Typology*	*Failure*
Pz_#21	*68*	*5.4*	*F*	*Right*	*Biolox® Delta*	*Stain*	*Aseptic Loosening*

III.9.3.1 Macroscopic results

Table III.10 shows the results of the new digital procedure proposed in this paper for the measurement of the metal transfer areal coverage. The MT covered an area between 29.6 and 573.6 mm^2. In particular, we measured: 41.1 and 573.6 mm^2 (min and max extension) for the ***Areal*** classification; 48.1 and 308.8 mm^2 (min and max extension, respectively) for the ***Stain*** classification, and 1.2 and 160.9 mm^2 for the ***Linear Scratch*** classification (min and max extension, respectively). A slightly difference was found by comparing the mean values of the MT percentage relative to the different materials, finding more extended MT on the Biolox® Forte. The composite Biolox® Delta did not show a greater nor a littler MT affection than the common ceramics.

3D coloured acquisition and digital reconstruction of the metal transfer phenomenon was performed on all the femoral heads. In **Figure III.40** three femoral heads are showed (one for each typology of classification). The MT is mostly located on the superior portion of the heads, at the centre or on a side.

Table III.10: *Measurements of the metal transfer observed on Biolox® Delta, Biolox® and Biolox®Forte femoral heads. The values are sorted by increasing values of metal transfer area.*

Heads number	**Material composition**	**Heads Area (mm^2)**	**Metal Transfer Area (mm^2)**	**Metal Transfer areal coverage (%)**
Pz_#13	Biolox® Delta	3418.4	41.1	1.2
Pz_#20	Biolox® Delta	3398.2	48.1	1.4
Pz_#24	Biolox® Delta	2146.3	29.6	1.4
Pz_#14	Biolox® Delta	3392.9	85.8	2.5
Pz_#17	Biolox® Delta	4024.5	106.9	2.7
Pz_#19	Biolox® Delta	3199.4	85	2.7

Pz_#10	Biolox® Forte	2764.6	89.6	3.2
Pz_#7	Biolox®	2764.6	95.1	3.4
Pz_#2	Biolox®	2824.9	95.3	3.4
Pz_#3	Biolox® Forte	2804.8	88.1	3.5
Pz_#23	Biolox® Delta	3392.9	127.9	3.8
Pz_#18	Biolox® Delta	3235.1	138.2	4.3
Pz_#8	Biolox® Forte	2804.8	126.5	4.5
Pz_#21	Biolox® Delta	4024.1	219.3	5.4
Pz_#22	Biolox® Delta	2816.7	153.7	5.5
Pz_#5	Biolox® Forte	2804.8	160.9	5.7
Pz_#12	Biolox® Forte	3415.5	234.5	6.9
Pz_#1	Biolox®	2804.8	238.7	8.5
Pz_#4	Biolox®	2804.8	286.1	10.2
Pz_#15	Biolox® Delta	4019.9	573.6	14.3
Pz_#16	Biolox® Delta	2143.1	308.8	14.4
Pz_#11	Biolox® Forte	2764.6	411.8	14.9

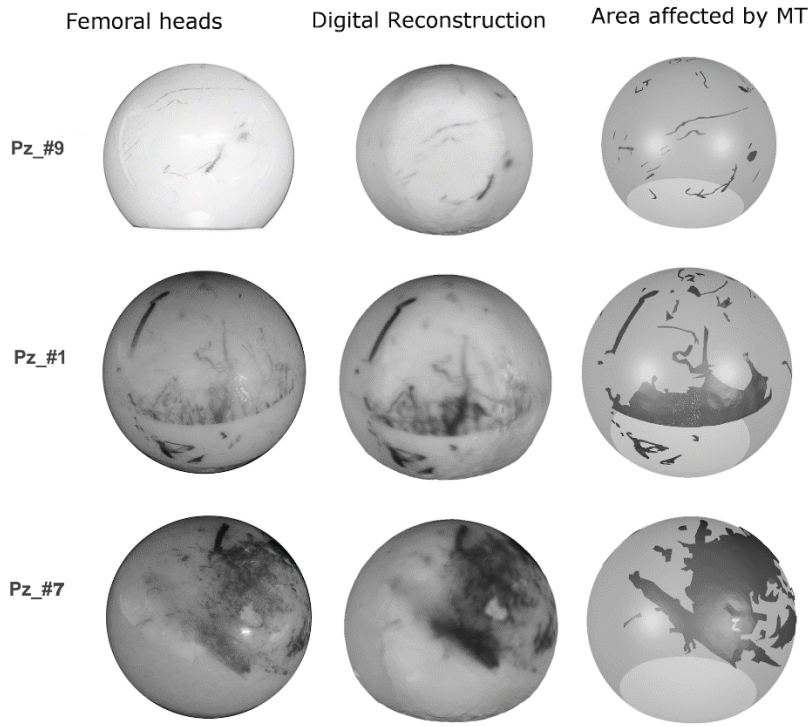

Figure III.40: *Characterization of the metal transfer on the three femoral heads: digital reconstruction and the area affected by Metal Transfer are showed.*

III.9.3.2 Microscopic results

By observing the obtained data collected in **Table III.11** it is possible to underline that the mean values of S_a and S_t parameters were different between the Affected Zone (S_a = 0.3 ± 0.1 µm; S_t = 33.2 ± 18.6 µm) and Unaffected Zone (S_a = 0.03 ± 0.01 µm; S_t = 22.1 ± 12.1µm). In contrast, the measurement of S_{sk} parameter was not statistical significant for both affected and unaffected areas (p = 0.388). By analysing the correlation of the surface roughness alteration and the MT areal coverage with the *follow up* of each femoral head no significant correlation was found. The S_a roughness value of the affected zone did not present sensible variances on the different materials. Regarding *St* instead, the Biolox® Delta femoral heads showed the lowest mean value (11.92 ± 9.09 µm). Biolox® and Biolox® Forte on the other hand had higher mean values (30.70 ± 29.10 µm and 44.72 ± 29.06 µm, respectively), suggesting that MT phenomenon caused higher peak and/or lower valleys on the surface of common ceramic implants. Regarding the S_{sk} parameter, its mean value is positive for the composite Delta and negative for the two

ceramics. This remark indicates a large occurrence of peaks rather than valleys on the composite ceramic, highlighting the coverage of metal particles on the implant surface. S_{ku} was way higher in the two ceramics than on the Biolox® Delta, corresponding to 250 and 281 for Biolox® Forte and Biolox®, whereas it was just 25 for Biolox® Delta, indicating a broader height distribution of the asperities on the composite ceramic.

Table III.11: *Roughness values for all the analysed specimens. The values are sorted by increasing values of S_a*

	Unaffected Area				Affected Area			
Heads	**Sa (µm)**	**St (µm)**	**Ssk**	**Sku**	**Sa (µm)**	**St (µm)**	**Ssk**	**Sku**
Pz_#4	0.04	1.54	-0.75	6.10	0.32	23.97	-1.34	13.78
Pz_#8	0.04	3.03	0.96	54.73	0.56	18.29	1.49	7.18
Pz_#24	0.04	0.97	-0.31	3.86	0.06	4.37	3.79	52.48
Pz_#9	0.04	5.88	0.00	0.08	0.08	14.91	0.00	0.04
Pz_#23	0.04	2.74	0.29	17.21	0.06	3.49	-0.36	14.11
Pz_#12	0.04	5.64	8.15	158.98	0.08	10.92	-2.57	129.87
Pz_#5	0.05	6.97	1.08	144.70	0.12	40.74	-14.94	923.64
Pz_#13	0.05	1.05	-0.68	4.88	0.06	1.52	0.13	5.50
Pz_#11	0.05	8.88	7.83	376.58	0.26	6.46	1.32	9.03
Pz_#15	0.05	0.89	-0.57	4.40	0.32	13.27	3.78	33.66
Pz_#19	0.05	2.18	-1.02	9.53	0.17	11.46	1.14	12.10
Pz_#18	0.05	4.92	0.64	25.48	0.05	4.38	-0.99	9.74
Pz_#20	0.05	10.83	1.51	267.39	0.35	22.00	3.36	42.30
Pz_#22	0.05	3.00	-0.03	15.44	0.29	9.80	-0.04	3.89
Pz_#1	0.05	3.86	2.99	54.68	0.73	90.88	-3.78	76.46
Pz_#21	0.05	0.80	-0.43	3.82	0.56	35.76	1.99	36.18
PZ_#2	0.05	1.79	-0.13	5.40	0.08	20.91	1.57	184.52
Pz_#14	0.05	1.12	-1.15	6.71	0.09	11.67	2.42	51.13
Pz_#17	0.05	1.25	-0.27	3.90	0.19	9.46	-0.76	8.71
Pz_#16	0.05	2.47	-0.52	4.67	0.17	5.46	0.84	7.09
Pz_#6	0.05	6.80	-1.63	50.37	0.40	89.82	-20.53	815.64
Pz_#3	0.06	9.64	-3.33	128.54	0.30	76.88	1.31	488.98
Pz_#7	0.06	7.38	6.96	173.93	0.32	50.98	-5.60	141.90
Pz_#10	0.09	15.60	2.71	231.14	0.17	36.92	-7.19	646.21

Figure III.41 shows the surface topography and the Abbott-Firestone curve acquired through the 3D optical non-contact scanner for the three generations of ceramic femoral heads (Biolox® Delta, Biolox® Forte, and Biolox®, respectively). The Abbott-Firestone curve represents the cumulative probability density function of the surface profile's height and it is calculated by integrating the profile trace, thus allowing a good characteristic for assessing functional properties of surfaces and their possible exploitation. It can be distinguished between different surfaces with the same value of Sa, or other height characteristics [198]. In **Figure III.41** the sample of Biolox Delta has the highest inclination of the central part which indicates a the greatest R_k (Kernel roughness) value [199].

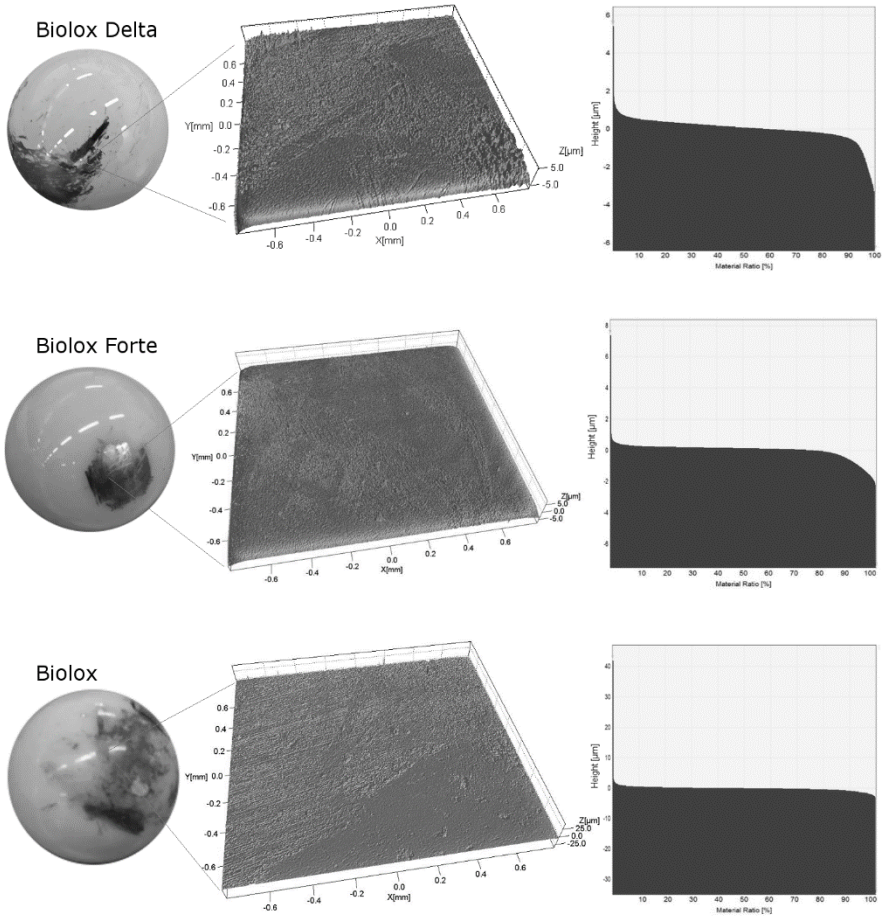

Figure III.41: *Surface topography and Abbott-Firestone curve of the affected zone for the three generations of ceramics heads.*

III.9.3.3 Surface pattern results

As a representative example, in **Figure III.42** and **Figure III.43** the pictures of the microanalyses performed on two femoral heads are showed, where the differences between the metal transfer and the signs attributable to a surgical instrument – usually made of stainless steel – during the revision of such implants are emphasized.

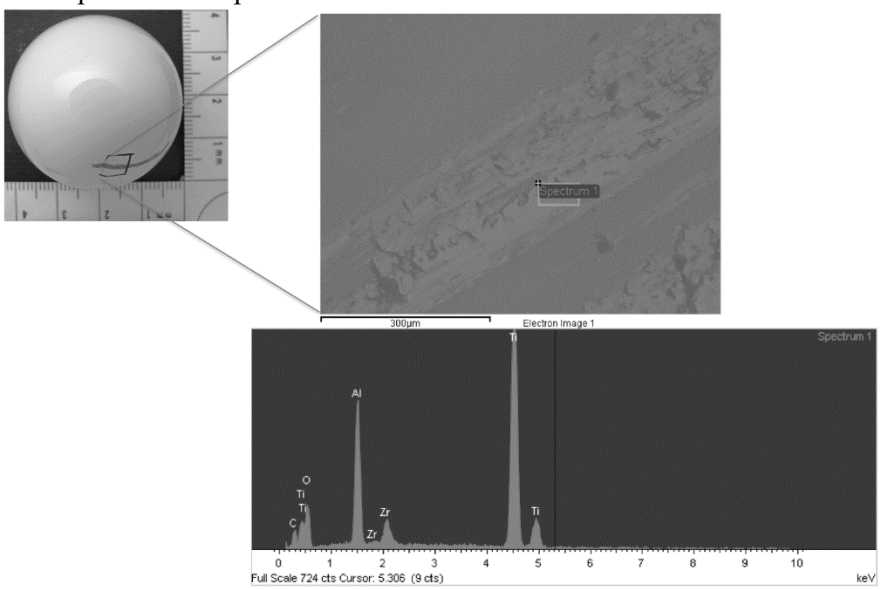

Figure III.42: *Characterization of the metal transfer on the femoral head #13 with the microanalysis performed.*

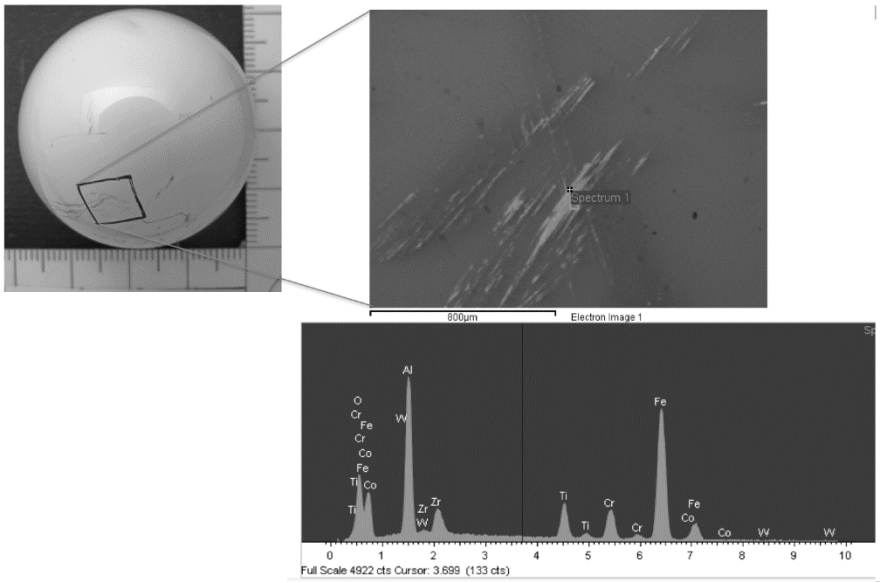

Figure III.43: *Characterization of the signs on the femoral head #23 attributable to a surgical instrument during the revision with the microanalysis performed.*

III.9.4 Discussion & Conclusions

We investigated whether metal transfer, observed on retrieved ceramic femoral heads, was associated with changes in the roughness surface compared with different *follow-up*. As explained in the Introduction section, the MT phenomenon is due to critical conditions with the increase of surface roughness and this may accelerate the implant wear. About the surface roughness, the parameters S_a and S_t appear to be slightly higher in areas affected by the MT phenomenon. The statistical analysis found significant differences ($p = 0.002$) in the comparison between affected and unaffected areas, thus highlighting that the surface roughness of the analysed femoral heads varies significantly in presence of MT phenomena. S_{sk} parameter, as shown in **Table III.11**, emphasizes variability between MT affected and unaffected areas but no statistical differences were found. The results obtained from microscopic analysis allows to emphasize that the MT resulted in a significant alteration of the contact surface; it could refer to a process of adhesion of metal on the surface, as S_a and S_t tend to increase in areas affected by the phenomenon. In particular, the S_t parameter was sensibly higher on the affected areas of common ceramic than on the ones of Biolox® Delta. Furthermore, the positive value of S_{sk} found on the affected surfaces of Biolox® Delta is an indicator of a greater occurrence of peaks. This alteration

of surface texture has sure consequences on how the synovial fluid flows on the surface [122], [200].

Our results indicate that the area of metal transfer on the ceramic femoral heads was greater for the Biolox® Forte than the Biolox® Delta and Biolox® **(Table III.10)**, even if, from a statistical point of view, no correlations were found between follow-up ***vs.*** roughness measurements and ***vs.*** MT areal coverage.

Full fluid film lubrication appears to be possible in ceramic-on-ceramic hip implants under most conditions, due to the small clearance and the smoothness of the bearing surfaces in their original state. As stated in [201] the way of fluid film in hip implants can be evaluated by comparing the estimated theoretical film thickness to typical surface roughnesses of the two bearing surfaces, by introducing the λ ratio. The strong importance of the lubrication regime on wear rate was first established by Chan et al. [202]; the volumetric wear was shown to correlate pretty good with the λ ratio. A rise in the λ ratio led to an improvement in the lubrication regime and therefore a noteworthy decrease in the wear volume. These results show that MT induces an important surface modification of the femoral heads, which could strongly modify the lubrication mechanism acting in the tribosystem (due to a sudden variation of the height of the meatus) thus favouring a fluid film rupture and/or the modification from elastohydrodynamic (EHL) or hydrodynamic lubrication backward mixed or boundary lubrication, thus causing localized contacts of the prostheses surfaces [203], [204]. As pointed out by Dowson [205], if only a small amount of the load is conducted through asperity contacts, the whole friction can rise considerably. In this framework, another important result of this study is the proposal and the successful application of a new digital procedure for evaluating the metal transfer areal coverage: the percentage of the surface covered by metal with respect to the entire surface of the retrieved femoral heads. The new digital procedure, based on an innovative 3D non-contact optical scanner and on the 3D analysis of the femoral heads' digital models, has proven to be suitable for investigating and measuring the metal transfer areal coverage. However, our results agree with the results from other authors. Kim et al. [112] analysed fifteen ceramic prosthetic femoral heads retrieved from fifteen patients at revision arthroplasty and confirmed the hypothesis that MT onto the ceramic femoral head increases surface roughness and consequently increases the wear rate of the polyethylene liner. In particular, those authors found four ceramic heads that had severe smears (>6% of the surface area), and the remaining nine heads had slight smears (<6% of the surface area). The two heads that had been *in vivo* less than one month had severe smears. Luchetti et al. [206] found metal transfer to a zirconia head when the head was scratched on the metal shell during a closed reduction of a dislocated total hip prosthesis. Elpers et al. [192] found that the roughness was not different among the apex, the equator, and the below the equator. According to our study, the authors found that the regions of metal

transfer were significantly rougher than the non-metal transfer regions of the articular surface ($p = 0.001$).

Notwithstanding, our study has several limitations mainly related to the numbers of explanted femoral heads available which affected the statistical analysis. In addition, the examination was not performed in a population of patients with identical components and same follow-up: femoral heads from three different generations were considered and they may have had different initial roughness and thus different surface characteristics. Future developments on this matter would evaluate the effect that MT could have on the lubricating phenomenon and on the acetabular cups. However, the results showed that MT induces an important surface modification of the femoral heads, which could strongly modify the fluid dynamic behaviour of the synovial fluid and favour a fluid film rupture, thus causing localized contacts of the prostheses surfaces [203].

IV Chapter
Biomechanics

Biomechanics is the application of mechanical principles, statics, strength of materials and stress analysis to the solution of biological problems of living organisms. This includes bioengineering, the research and analysis of the mechanics of living organisms and the application of engineering principles to and from biological systems. After a brief introduction to the main concepts of kinematics applied to the human body, this chapter will focus on the study of the human gait, the musculoskeletal model and the inverse dynamic analysis. The final sections will expose the results so far obtained through the model.

IV.1 Articulations

As well known, a rigid body in the space has three Degrees of Freedom (DoF) for the translation and three DoF for the rotation, whereas in a 2D plane the rigid body has two DoF for translation and two for rotation. In light of these remarks, it is possible to model the human body standing the sequent simplifications:

- each segment of the system is considered as rigid body linked to the contiguous segments with the articulations;
- the body configuration can be determined uniquely by a finite number of parameters, i.e. its DoF;
- the inertial characteristic of the segments could be calculated considering simplified shapes;
- the system, under external forces, is controlled in the movement and stability by a finite number of muscular actions, applied in the points defined by the segments.

The articulations are joints between bone extremities having conjugate shapes. They can be mobile, semi-mobile or fixed. They are divided in *synarthrosis* (immobile joint), *amphiarthrosis* (slightly mobile joint) or *diarthrosis* (freely moveable joint).

The synarthrosis are connections between two contiguous bones. The fixed nature of these joints provides a strong union between articulating bones. They can be dived in two subcategories considering the bone tissues that is present on the bone extremities, they are *gomphoses* (found in the sockets of the teeth) and *synostoses*.

An amphiarthrosis has a limited mobility. As an example, the articulation connecting the bodies of adjacent vertebrae is an amphiarthrosis. The small movements allowed between the vertebral can sum together along the length of the vertebral column providing a large range of movements.

Diarthrosis joints are freely mobile. These joints include synovial joints, that provide most of the mobility in a human body. Diarthrosis are further classified about the mobility in uniaxial (for movement in one plane), biaxial (in two planes) or multiaxial (in all the three planes). Elbow joint is an example of uniaxial joint, it allows only bending or straightening. Knuckle joint of the hand is a biaxial diarthrosis. Hip and shoulder are multiaxial joints, they allow the upper and lower limbs to move in anterior-posterior direction and medial lateral one. In addition, the limb can also rotate around its long axis. More detailed classification can be found in **Figure IV.1**.

A kinematic pair is a connection between two bodies which imposes constraints on their relative movement. A system defined by a finite number of members, connected by kinematic pair is called a *cinematic chain*, its DoF could be calculated by the *Kutzbach criterion*. In a 3D space, the explicit form of this criterion can be expressed by the following formula:

$$DoF = 6(m-1) - 5\,c_1 - 4\,c_2 - 3\,c_3 - 2\,c_4 - c_5\,, \qquad (IV.1)$$

where m is the number of members composing the chain, and c_i is the number of kinematic pairs allowing i DoF to the relative movements of the members it connects.

For 2D space, Kutzbach criterion simplifies to the *Grubler's formula*, which follows:

$$DoF = 3\,m - 2\,c_1 - c_2\,. \qquad (IV.2)$$

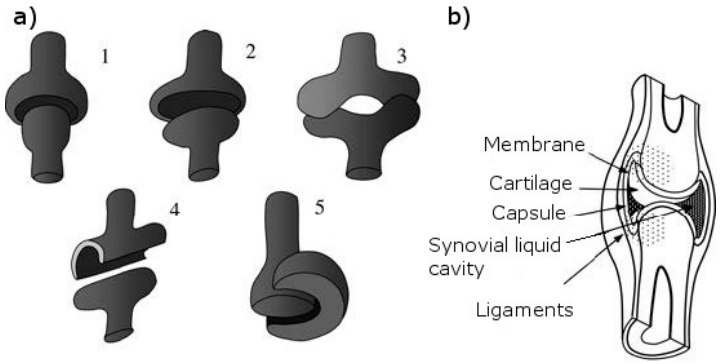

Figure IV.1: *a) Diarthrosis joints: 1-*enarthrosis *two spherical (convex-concave) members, 2-*condilarthrosis *two elliplticaI (convex-concave) members, 3-*saddle *two biaxial (convex-concave) members, 4-*trochoid *two cylindircal (empty-full) members, 5-*ginglymoid *two coaxial cylinders with axis parallel to the bone; b) A synovial joint.*

As an application example of this criterion, an interesting case of study in the human body are the upper and lower limb articulations. They are considered revolute joints – the hip articulation is a spherical one.

As a simplified example, it is possible to consider the plane cases, as it is illustrated in the lower limb example of **Figure IV.2**. In this plane case it should be used the formula of **eq. IV.2** where c_1 is 3 – the number of plane hinges – whereas c_2 is zero. Being *m* equal to 5, the degrees of freedom result 6. It is important to highlight that the reduction of the joint to such a perfectly geometrical model is a strong simplification.

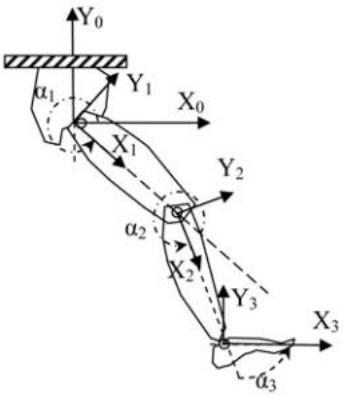

Figure IV.2*: Schematic representation of the lower limb*

The coxofemoral joint is of fundamental importance, the pelvis load bilaterally the femoral heads. The right functionality of this load is related to the perfect centring of the joint. Being a diarthrosis, the coxofemoral is strongly mobile. The hip joint operates mainly to sustain the trunk, during walking. The joint has three DoF for the rotation, which correspond to the flexo-extension movement, around a transversal axis, to the abduction-adduction around an anterior-posterior axis, of rotation interior and exterior around the longitudinal axis of the femur. Each of these movements is limited by the maximum extension of the ligaments.

IV.2 The human gait

The act of walking is a complex procedure, which humans carry out automatically, it involves different organs of the body that work together to perform a movement. First, the motion control occurs thanks to the brain, in particular the supraspinal centres (cerebellum and sensorimotor cortex) that convert an idea of movement into the pattern of muscle activity that is necessary to perform a task.

The joint forces and moments imply the rigid skeletal links (segments such as the thigh, calf, foot, etc.) to move and to apply body weight on the external environment. The sequence of events that take place to obtain walking are shown in **Figure IV.3** can be summarized as follows:

1. registration and activation of the gait command in the central nervous system;
2. transmission of the gait signals to the peripheral nervous system;
3. contraction of muscles that produce tension;
4. generation of forces in, and moments across, synovial joints;
5. regulation of the joint forces and moments by the rigid skeletal segments based on their anthropometry;
6. displacement of the segments in functional gait;
7. generation of ground reaction forces.

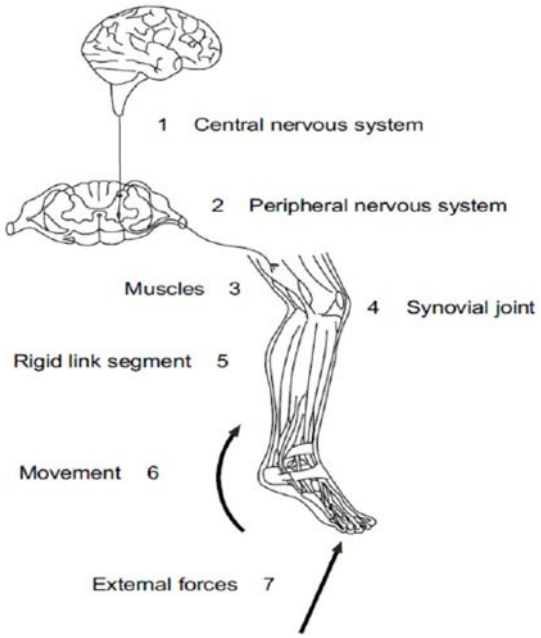

Figure IV.3: *The seven components that form the functional basis of humans walking.*

Being the act of walking a repetitive cycle, its description can be done just by analysing a single cycle, with the assumption that subsequent cycles are equal. This is considered a reasonable approximation of what actually happens. In **Figure IV.4** it is shown a single cycle of walking, by convention the cycle starts when one feet touches the ground.

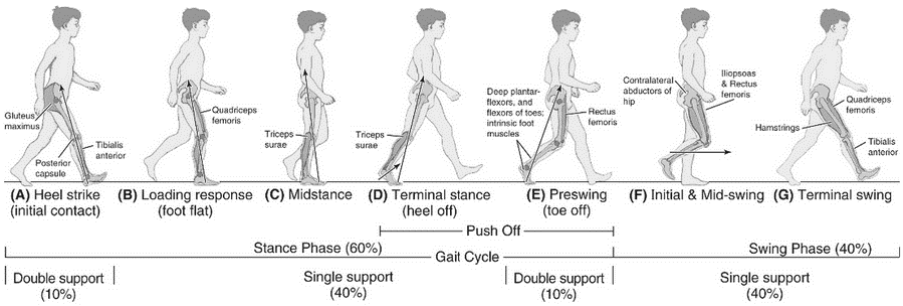

Figure IV.4: *Gait cycle* [246].

There are two main phases: during *Stance Phase*, the foot touches the ground, whereas in *Swing Phase* that same foot is no longer in contact with the it and the leg is swinging through preparing for the next strike. Furthermore, the stance phase may be divided into three phases:

1. first double support, when both feet are in contact with the ground;
2. single support, when the left foot is swinging through and only the right foot is in ground contact;
3. second double support, when both feet are again in ground contact.

Note that the nomenclature in **Figure IV.4** refers to the right side of the person, the same terminology would be used for the left side, which is usually half a cycle behind (or ahead of) the right side. Therefore, the first double support for the right side is the second double support for the left side, and vice versa. It is worth noting that in a normal gait – as the one described – there is symmetry between the left and right sides, but in pathological gait an asymmetrical pattern is often found.

The gait cycle has been divided into eight events, five of which are in the stance phase and three during the swing. These events are described by the movement of the foot, following a self-descriptive nomenclature. For the stance phase, are:

1. **Heel strike** initiates the gait cycle and represents the point where the centre of gravity is in its lowest position;
2. **Foot-flat** represents the point when the plantar surface of the foot touches the ground;
3. **Midstance** happens when the swinging (contralateral) foot goes by the stance foot and the body centre of gravity is in its highest point;
4. **Heel-off** occurs when the heel loses contact with the ground and the push off starts via the triceps muscle;
5. **Toe-off** ends the stance phase as the foot leaves the ground.

The swing phase is composed by:

6. **Acceleration** starts when the foot leaves the ground and the subject activates the hip flexor muscles to accelerate the leg forward;
7. **Midswing** occurs when the foot passes beneath the body, it corresponds with the midstance of the other foot;
8. **Deceleration** describes the action of the muscles as they slow the leg and stabilize the foot preparing for the next heel strike.

The traditional nomenclature here described, is sufficient to represent the normal gait cycle of a healthy subject. But it is not suitable in case of patients with pathologies, such as spastic cerebral palsy. An alternative nomenclature, developed by Perry (in [207]), is shown in the lower part of **Figure IV.4**. Also in this case there are eight events, but these are sufficiently vague to be applied to any type of gait:

1. Initial contact (0%);
2. Loading response (0-10%);

3. Midstance (10-30%);
4. Terminal stance (30-50%);
5. Preswing (50-60%);
6. Initial Swing (60-70%);
7. Midswing (70-85%);
8. Terminal swing (85-100%).

IV.2.1 Distance Measures.

Whereas **Figure IV.4** highlights the chronological aspects of human gait, **Figure IV.5** shows a set of footprints that provide distance parameters. *Stride length* is the distance travelled by a person during one stride (or cycle) and is evaluated as the length between the heels from one heel strike to the next heel strike on the same side. With healthy subjects, the two step lengths (left plus right) make one stride length. With normal subjects, the two step lengths will be approximately equal, whereas in certain patients there will be an asymmetry in the two step lengths. Another parameter is the *Step width* which is the mediolateral distance between the feet. At last, the angle of the foot relative to the line of progression documents the degree of external or internal rotation of the lower extremity during the stance phase.

IV.2.2 Gait Analysis

The Gait Analysis is a procedure broadly used in Europe and in the US, to assess the human gait. This test evaluates truthfully the movement of each joint in the space at any moment. Usually, the tests take place in laboratories equipped with six infrared cameras and one or more dynamometric platforms placed in the floor, which record the foot-ground reaction forces. The gait analysis is an indirect, painless measurement method based on the application of markers deflecting the light in specific anatomical place. The cameras recreate the body parts and their movements. The inspection yields an accurate analysis of the speed of walk, the distance and timing of steps and other factors. These parameters allow to assess the wellbeing of the walk, the stability of the patient, and so on. It also aims at precisely evaluating the

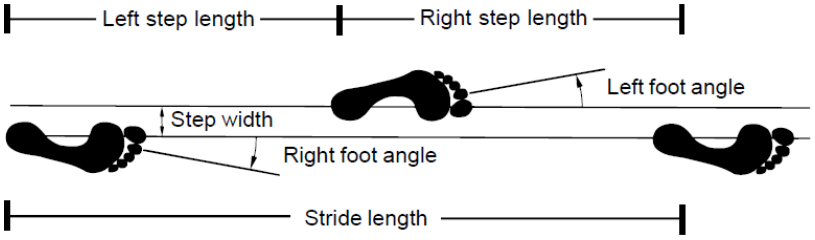

Figure IV.5*: A person's footprints*

movements of each joint, searching for defects and compensation of the physiological movement as well as the forces created and absorbed. Gait analysis is suggested to patients who walk with signs of spasticity or lack of strength or step patterns alterations.

IV.2.3 Measurements and the Inverse Approach

Measurements should be taken as high up in the movement chain as possible, so that the gait analyst handles the causes of the walking pattern, not just the effects. There are essentially two kinds of problems in rigid body dynamics: the first is the *Direct Dynamics Problem* in which the forces being applied to a mechanical system are known and the objective is to determine the resultant motion; the second is the *Inverse Dynamics Problem* in which the motion of the mechanical system is defined, and the purpose is to find the forces causing that motion. The latter is the problem that the gait analyst settle.

The direct measurement of the forces and moments transmitted by human joints, the tension in muscle groups, and the activation of the central nervous systems is far from being possible. That is why in gait analysis has been adopted the indirect or inverse method. This approach is illustrated verbally in **Figure IV.6a** and mathematically in **Figure IV.6b**.

Note that four of the components –the ones with rounded border – in the movement chain (3, electromyography; 5, anthropometry; 6, displacement of segments; and 7, ground reaction forces) could be measured by the analyst. Electromyography does not measure the tension in muscles, but it can give insight into muscle activation patterns. Ground reaction forces F_G are used with the segment masses and accelerations in the equations of motion which are solved in turn to give resultant joint forces and moments F_J.

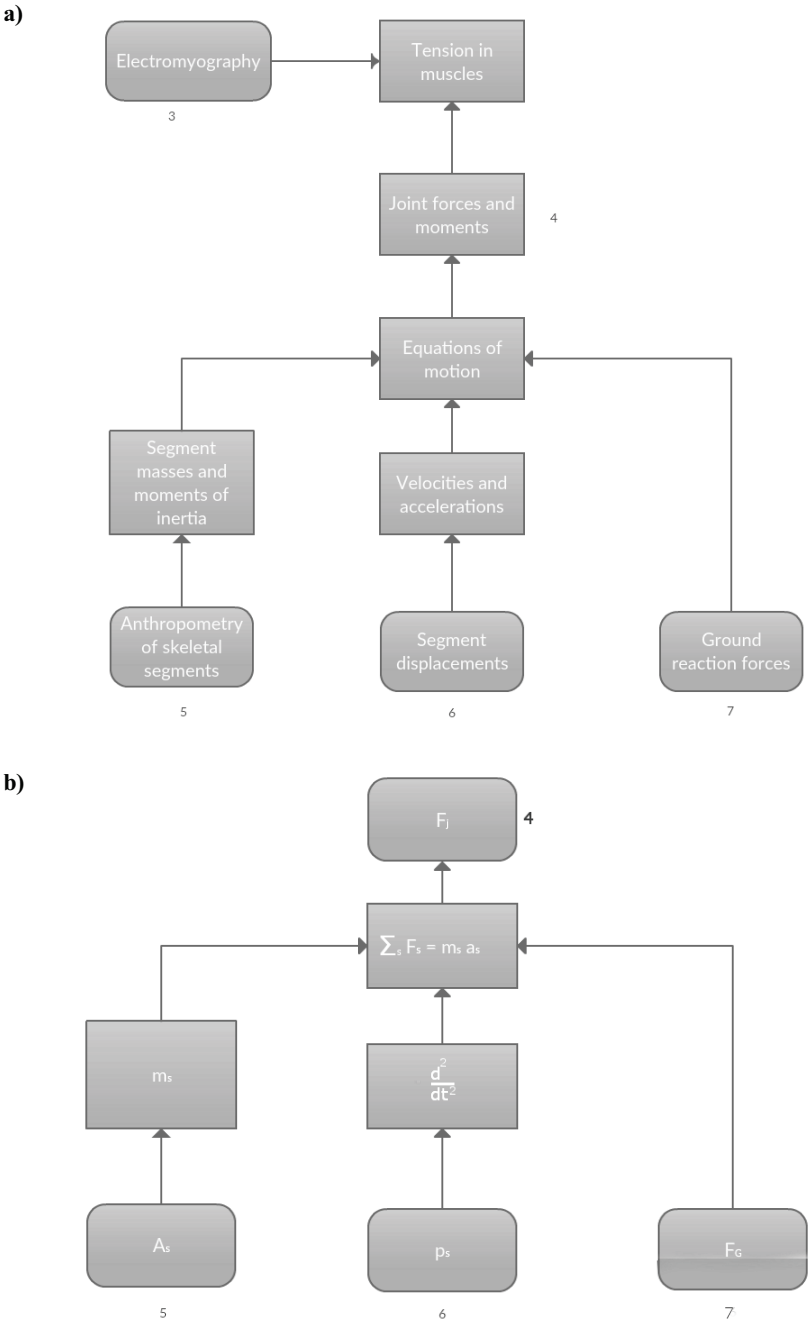

Figure IV.6: *Flow chart of the gait analysis: a) verbally and b) mathematically*

IV.2.4 Anthropometry

The Gait Analysis must chase the approach of Inverse Dynamics as the movement of the mechanical system is known. However, this approach is not simple, as it requires a high number of variables hard to define precisely.

IV.2.4.1 Body Segment

A major concern in this procedure is personalizing the body segment parameters of each patient. *The Body segment parameters* are:

- **Mass** in kilograms of the segments (e.g., thigh, calf, foot);
- **Centre of Gravity** position of the distinct segments relative to some specified anatomical landmarks (e.g., proximal and distal joints);
- **Moments of Inertia** of the segments about three orthogonal axes that pass through the segment centre of gravity.

IV.2.4.2 Segment mass

Segment mas are related to the subject body mass and to the dimension of the segment. As segment mass is evaluated as density times volume, it is necessary to link the segment with a composite parameter that has the dimension of a length cubed. Therefor it is necessary to solve a linear regression of the form:

$segement\ mass = A\ \times (total\ body\ mass) + B \times (length)^3 + C,$

where *A*, *B* and *C* are the regression coefficients. Some regression equations are available in [208].

IV.2.4.3 Moments of Inertia

Being the moment of inertia a measure of the body resistance to angular motion, the linear regression to solve is:

$segment\ moment\ of\ inertia = D \times (total\ body\ mass)^2 + E\ ,$

where *D* and *E* are regression coefficients.

IV.2.5 Linear and angular kinematics

In biomechanics, the human body is modelled through rigid body segments connected with each other. As already stated in **section IV.1**, each body segment free to move in the space has six DoF. Therefore, to locate each of this segment in the space it is required to know three coordinates in a Cartesian plane (x, y, and z) and three rotation angles (Euler angles). In order to determine these coordinates, a series of marker are placed on the elements of a person. The marker records the position in the space and, to do this, each marker is associated with a local coordinate system (x_i, y_i and z_i) located in

the centre of gravity. Therefore, it is possible to obtain each element position in the global coordinate system.

To express the orientation of the segments in the space there are two ways: first, one segment can be orientated relative to another – the anatomical joint angles; second, one segment is oriented relative to the fixed reference frame – the segment Euler angles.

IV.2.5.1 Anatomical joint angles

Anatomical joint angles are expressed as a rotation of the distal segment relative to the proximal segment. Rotations can be summed up as follows:

- flexion and extension that occur around the mediolateral axis of the proximal segment (z axis, as it appears in **Figure IV.7**);
- internal and external rotation around the longitudinal axis (x axis)
- abduction and adduction around a floating axis that is at square angles to both flexion/extension and internal/external.

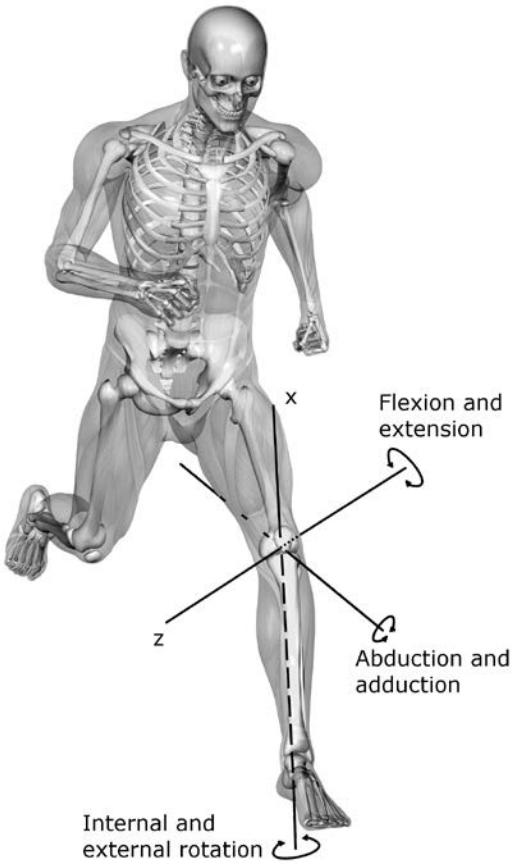

Figure IV.7: *The axes of rotation for the left knee. There are three range of motion: flexion/extension, internal/external rotation and abduction*

IV.2.5.2 Euler Angles

To define the orientation of the segment in space it is required to state the three Euler angles associated with it. Segment Euler angles play a key part in estimating angular velocities and accelerations. Euler angles are a means of representing the spatial orientation of any reference frame x_i, y_i, z_i as a composition of three elemental rotations beginning from a known orientation, represented by the global reference frame X, Y, Z. The reference (global) orientation can be imagined to be an initial orientation from which the frame virtually rotates to reach its actual orientation. In the following, the axes of the original frame are denoted as X, Y, Z and the axes of the rotated frame are denoted as x_i, y_i, z_i. In this case, it is called a "local" coordinate system, and it is meant to represent both the position and the orientation of the body. The geometrical definition of the Euler angles is based on the axes of the original

and rotated reference frames and an additional axis called the line of nodes. The line of nodes (N) is defined as the intersection of the x_iy_i and the XY coordinate planes. Namely, it is a line passing through the origin of both frames, and perpendicular to the z_iZ plane. The three Euler angles are defined as follows (see **Figure IV.8**):

- α is the angle between the x axis and the N axis;
- β is the angle between the z axis and the Z axis;
- γ is the angle between the N axis and the X axis.

Which implies that:

- α represents a rotation around the z axis;
- β represents a rotation around the N axis;
- γ represents a rotation around the Z axis.

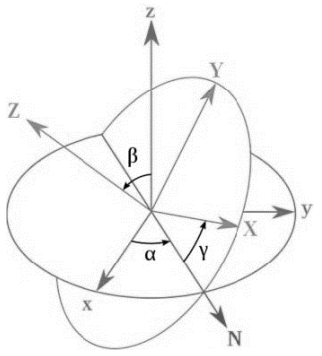

Figure IV.8: *Euler Angles*

IV.3 Dynamics of Joints

To study the dynamics, the causes of motion, it is necessary to integrate body segment parameters, linear kinematics, centres of gravity, angular kinematics, and ground reaction forces in the equations of motion to yield the resultant joint forces and moments.

IV.3.1 Ground reaction Forces

To obtain three-dimensional gait analysis, it is required a force plate that gives six pieces of information:

1. Force in the X direction, F_x
2. Force in the Y direction, F_y
3. Force in the Z direction, F_z
4. Position of the resultant force in X direction, D_x

5. Position of resultant force in Y direction, D_y
6. Torque about Z axis, T_z

To record these information, there are two possibilities: force plates, that are based in the ground and register the force between the ground and the foot; and pressure insoles, which are worn inside the shoe. Whereas the force plate can only record the stance phase, the pressure insole moving with the subject can record multiple steps.

IV.3.2 Joint Forces and Moments

Being the resultant forces and moments three-dimensional vectors, they can be expressed in term of their components. This can be done by using the global reference frame XYZ or by expressing these forces in term of body-based coordinate system (having anatomical meaning). Usually, they are used the same axes to define anatomical joint angles:

Forces

- A mediolateral force takes place along the mediolateral axis of the proximal segment
- A proximal/distal force takes place along the longitudinal axis of the distal segment.
- An anterior/posterior force takes place along a floating axis that is perpendicular to the mediolateral and longitudinal axes (see **Figure IV.9**).

Moments

- A flexion/extension moment takes place about the mediolateral axis of the proximal segment.
- An internal/external rotation moment takes place about the longitudinal axis of the distal segment.
- An abduction/adduction moment takes place about a floating axis that is perpendicular to the mediolateral and longitudinal axes (see **Figure IV.7**).

IV.4 Musculoskeletal Model

Gait analysis calculates the location of the legs as a person walks and logs their foot reaction on the ground using a force plate (see **section IV.2**); these data can be used to evaluate joint angles during the gait cycle and, by a musculoskeletal model, muscle and joint contact forces can be predicted. By doing this, they can be studied the loads taking place on the joint prosthesis, with a non-invasive method. The range of forces predicted by this model

would be used to update computational and experimental analyses. To obtain such model it was used a software called AnyBody Modelling System, developed at Aalborg University. The system can model the musculoskeletal structure and the environment that interacts with it; compute forces in muscles,

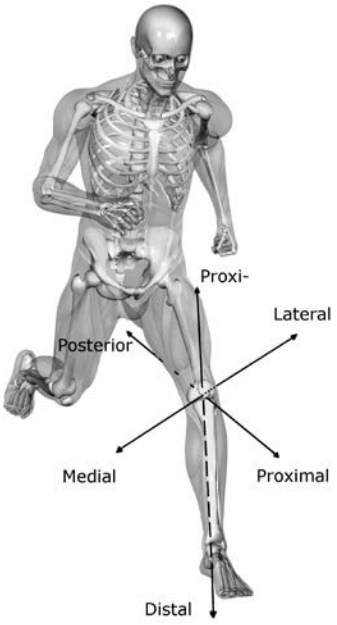

Figure IV.9: *The reference frame for the left knee expressing the component of the resultant forces.*

elastic energy in tendons, join reactions etc. Each body model consists of segments (bones), joints between segments and tendon-muscles unit.

The user can model any kind of posture or motion, through either a pre-existing model from *The AnyBody Managed Model Repository (AMMR)*; or from scratch. The AMMR is a library that contains a collection of template body models that mimic a variety of actions of daily living.

IV.4.1 Muscle models

AnyBody has three different muscle models, from simple to more complicated physiological performance.

In the simplest muscle model (*AnyMuscleModel*), the only input is the muscle's assumed isometric length, F0, i.e. the force, which the muscle can apply in static condition at its ideal length. F0 is often evaluated as proportional to the cross-sectional surface of the muscle. The second muscle model (*AnyMuscleModel2ELin*) assumes that the muscle strength is proportional to the current length and to the contraction velocity. The model

also presumes that the tendon is linearly elastic. The most complex model (*AnyMuscleModel3E*) consists of three elements:

1. A contractile section being the active assets of the muscle fibres;
2. A parallel-elastic section being the passive stiffness of the muscle;
3. A serial-elastic section being the elasticity of the tendon.

IV.4.2 The model elements

The mechanical elements that compose the model are:

- **Segments**
  Segments are the rigid bodies on which the system builds its investigation. In a body model, segments are typically bones, but they can also be cranks, pedals, handles, tools and all the other objects a body may be coupled to. They don't have any specific shape and are originated in their centre of mass. Their mass properties are described by the mass and an inertia tensor.
- **Joints**
  Through joints, the software connects multiple segments to each other and constrain the motion
- **Drivers**
  Drivers are used to create movement in the model. They are function of time defining the position of a joint or the distance between two points.
- **Kinematic measures**
  Kinematic measures are a representation of kinematical constraints. A joint angle or a distance between two points are example of kinematic measures.
- **Forces**
  There are several kinds of forces in AnyBody: forces in joint, in muscles, and gravity forces. There are also external forces, usually perceived as vectors with a point of attack, a direction, and a module.

IV.5 Inverse Dynamic Analysis

To evaluate the joint forces, the kinematic data and ground reaction force are used as input for musculoskeletal model. These data are collected using special Motion Capture tools used in the gait analysis laboratories, which allows to measure a subject's gait using optical sensors which monitors markers on the person's skin. These data, in conjunction with ground reaction forces allows to evaluate the loads acting on muscles and joints.

IV.5.1 Muscle recruitment

The body has many more muscles than needed to balance its degree of freedom. This means that there are infinitely many ways the body can employ its muscle – which the central nervous system (CNS) chooses – to perform the action. Mathematically, this implies that not enough equilibrium equations are available to determine all the unknowns of the problem. It is therefore necessary to utilize an algorithm to establish the activation of each muscle to replicate the role of the CNS. The solution of the muscle recruitment problem in the inverse dynamics approach is generally formulated as an optimization problem on the form:

$$min\, G(f^{(M)}), \qquad (IV.3)$$

with

$$Cf = d, \qquad (IV.4)$$

$$0 \le f_i^{(M)} \le N_i, \quad i \in \{1, \dots, n^{(M)}\}, \qquad (IV.5)$$

where G is the objective function **(IV.3)**, namely, the chosen criterion of the recruitment strategy of the CNS, stated in terms of the muscle forces, and minimized with respect to all unknown forces in the problem, $f = [f^{(M)T}\ f^{(R)T}]^T$, (muscle forces and joint reactions). **Eq. IV.4** is the dynamic equilibrium equation, which represent constraints in the optimization. C is the coefficient matrix for the unknown forces/moments in the system whereas d is a vector of all the known applied loads and inertia forces. The non-negativity constraints on the muscle forces imposed by equation (3), express that muscles can only pull, not push and the upper bounds limit their capability, so N_i is the strength of the muscle.

One of the most widespread expression of the objective function *G*, is the polynomial criteria:

$$G\left(f^{(M)}\right) = \sum_{i=1}^{n^{(M)}} \left(\frac{f_i^{(M)}}{N_i}\right)^p \qquad (IV.6)$$

where p is a variable power, and N_i a normalizing function for each muscle. The normalized muscle force is also known as the *muscle activity*. The most physiologically rational choice of N_i is some measure of the muscle strength. In this study the recruitment was calculated using a value of $p = 2$, since literature assess it as a reasonable predictor of muscle activation [209], [210].

The mathematical model of the mechanical system must produce the equations of motion in the form of **eq. IV.4**. The AnyBody Modelling System™ implements a general multibody system dynamics approach using a reference frame for each body to solve the equilibrium equations of the model. All segments of the system are considered rigid bodies, neglecting effects such as the unsteady forms of soft tissues. The position of the body is described by the following coordinates:

$$\boldsymbol{q}_i = \left[\boldsymbol{r}_i^T \boldsymbol{p}_i^T\right]^T \qquad (IV.7)$$

where $\boldsymbol{r}_i$ is the global position vector of the center of mass and $\boldsymbol{p}_i$ is a vector of four Euler parameters. The velocity of the bodies is defined as:

$$\boldsymbol{v}_i = \left[\dot{\boldsymbol{r}}_i^T \boldsymbol{\omega}'^T_i\right]^T \qquad (IV.8)$$

where ω'_i is the angular velocity of the body measured in the body-fixed reference frame.

The kinematic analysis is carried out in terms of all the Cartesian coordinates by solving a set of imposed kinematic constraints in the form of:

$$\Phi\,(\boldsymbol{q}, t) = 0\,, \qquad (IV.9)$$

where $\boldsymbol{q} = \left[\boldsymbol{q}_i^T \ldots \boldsymbol{q}_n^T\right]$ is the coordinate vector for all n segments. t is the time, which indicates that some of the constrains are kinematical drivers arising from the joints. In the case of inverse dynamics analysis, the imposed constraints in **eq. IV.9** must specify the motion completely.

Eq. IV.9 formula is generally a non-linear system of equations and it is solved by a modified Newton–Raphson numerical scheme. Then, the linear velocity and acceleration constraints are solved in terms of v and $\dot{v}$ instead of time-derivatives of q.

Once known the motion completely in q, v and $\dot{v}$ it is possible to define the dynamics equilibrium of **eq IV.4**. For each segment, the Newton Euler equations take this form:

$$\begin{bmatrix} m_i I & 0 \\ 0 & J_i' \end{bmatrix} \dot{v}_\iota + \begin{bmatrix} 0 \\ \widetilde{\omega_\iota'} J_i' \omega_i' \end{bmatrix} = g_i\,, \qquad (IV.10)$$

where m_i and J_i' are the mass and the inertia tensor referring to the centroidal body-frame, respectively. g_i, represents the forces, having six entries, three forces and three moments in body-fixed coordinates. It consists of muscle forces, $g_i^{(M)}$, reaction forces, $g_i^{(R)}$, and known applied loads, $g_i^{(app)}$, that could depend explicitly on in q, v and t. $g_i^{(M)}$ and $g_i^{(R)}$ enter in **eq. IV.4** on the left-hand side, whereas the remaining entries in **eq IV.10** enter d_i; thus the full right-hand side of **eq. IV.4** is assembled as $d = [d_1^T \ldots d_n^T]^T$. d_i is defined as:

$$d_i = g_i^{(app)} - \begin{bmatrix} m_i I & 0 \\ 0 & J_i' \end{bmatrix} \dot{v}_\iota - \begin{bmatrix} 0 \\ \widetilde{\omega_\iota'} J_i' \omega_i' \end{bmatrix}. \qquad (IV.11)$$

Like the unknown forces, $f = [f^{(M)T}\, f^{(R)T}]^T$, their coefficient matrix, C, can be partitioned according to muscle and reaction forces. This follows from standard forms of the constrained equations of motion for a multibody system where $f^{(R)}$ is given by Lagrange multipliers associated with the constraints. A constraint imposed on the motion by a mechanical device corresponds to a reaction force component in that device. However, the kinematical constraints also contain pure motion specification of the system's DoF. The muscles are

geometrically modelled as elastic strings bridging between two or more points and in cases wrapping over rigid obstacles.

IV.5.2 The model

The generic lower limb model consists of an 18 degrees of freedom (DoF) gait model of the lower limbs containing seven segments, the pelvis and three segments in each leg; thigh, shank and foot. The hip joints were modelled as spherical joints, the knees as revolute joints and the ankles as universal joints. As previously mentioned the software requires kinematic data and ground reaction force as input. It was used three different sets of data (three different gait cycle), available from the software repository. The first one was created with gait analysis data from Vaughan et al. [211] whereas the others two were obtained by the AnyBody research group, recorded in the gait Lab of Aalborg University: the Gait Normal (simulating a normal walking) and Gait Fast (simulating a faster walking).

The force and moment found were normalized with respect to the body weight of the subject and shown as function of a single gait cycle, that started and ended with foot contact.

IV.6 Dynamic results and load effect on retrieved knee implant

In this section they will be presented the results of the musculoskeletal model, showing the load and motion on the knee joint and an investigation on the load distribution on the roughness and wear of the explanted knee implants. This section is extracted from the article "*On the Bio-Tribology of Total Knee Replacement: a new Roughness Measurements Protocol on in-vivo Condyles Considering the Loads Obtained from Musculoskeletal Software*" published on the journal Measurement 112 in 2017 (pages 22-28), authors: Alessandro Ruggiero, Massimiliano Merola and Saverio Affatato.

IV.6.1 Aim

Many Authors focused on the analysis of loads acting on knee joint for different activities, as level walking, climbing stairs or running to estimates a more realistic load profile and, thereby, obtain a more realistic behavior of the artificial knee joints during wear simulations [212]–[214]. In these works, it is highlighted a strong inter-individual variation of load patterns among the analyzed subjects mainly due to anthropometric features specific to each patient. We have used a musculoskeletal modelling software, with different gait patterns, to estimate loads acting on knee joint during level walking. This would lead to a better understanding of the loads acting on a knee implant and gain evidences of the different loads acting on medial and lateral condyle. This hypothesis is based on a previous work [215] where the authors found

different wear intensity on the condyles of the same inserts material here analyzed, i.e. ultra-high-molecular-weight-polyethylene (UHMWPE).

The objective of this research is to find a correlation between the loads acting on the condyles and the surface roughness of 11-explanted UHMWPE inserts of the same design, to correlate the activity intensity of the patients to the alteration of the bearing couple in TKA.

IV.6.2 Materials and method

IV.6.2.1 Patients

In this study, we selected 11 total knee prostheses from the REPO database (Register of Explants of Orthopedic Prosthesis) that collects and classifies medical devices explanted at Rizzoli Orthopaedic Institute (Bologna. Italy). Since the tribological and wear behavior of a TKR is strongly influenced by prosthesis type, design, stabilization and fixation [216], [217], to prevent the variability in surface roughness due to these factors we selected the largest TKR group available with the same characteristics. The chosen prostheses have the same design (NexGen, Zimmer, Warsaw, Indiana) and were all cemented fixed bearing inserts and posterior stabilized (the UHMWPE meniscal component snaps or press fits into the tibial tray). They were explanted from 11 patients after a mean of 3.2 years (from 1.1 to 7.4 years); the patients were 9 women and 2 men with a mean age of 68 years (48 minimum and 77 maximum) at implantation. These prostheses patient's details are shown in **Table IV.1**.

Table IV.1: *Patients Details.*

Patient	Age at Surgery	Gender	Height (cm)	Weight (kg)	BMI	Implant Size	Implant Side	Follow Up (ys)
#1	48	Female	160	65	25.4	3	R	1.7
#2	77	Female	157	67	27.2	3	R	3.8
#3	67	Female	148	70	32.0	3	R	7.4
#4	60	Female	150	86	38.2	3	R	4.7
#5	76	Female	160	64	25.0	4	R	1.3
#6	71	Female	158	66	26.4	4	R	7.4
#7	72	Female	160	68	26.6	4	R	1.8
#8	57	Female	160	89	34.8	4	L	4.6
#9	73	Female	168	64	22.7	5	L	1.4
#10	71	Male	175	70	22.9	6	R	1.1

Table IV.1: *Patients Details.*

Patient	Age at Surgery	Gender	Height (cm)	Weight (kg)	BMI	Implant Size	Implant Side	Follow Up (ys)
#11	74	Male	170	87	30.1	7	R	1.2

Roughness measurements

To characterize the surface roughness of the specimens, four indicators were gained: R_a, R_t, R_q and R_{sk} as already considered in previous works [138], [167], [193], and already described in **section III.4.2**.

IV.6.2.2 Surface analyses of UHMWPE menisci

The topographic surface acquisitions, by 3D optical profiler, were performed using a Sensofar PLu Neox profilometer (Sensofar, Terrassa, Spain), already described in **section III.8.2.2**. In this work, the profiler was used in confocal mode, selecting a confocal objective with 20× magnifications. Six topographies were performed for each polyethylene compartment; three profiles were extracted for each topography, obtaining a total amount of 18 measurements per implant. The acquisition length on the Z-axis had a mean value of 160 µm, and it was varied according to the natural curvature of the surfaces. The extended topography of 1×4 stitched acquisitions, covered an area of 0.477 mm × 2.07 mm. All the specimens underwent the same procedure before acquisition: the samples were cleaned in an ultrasonic bath of distilled water for five minutes, then dried in ambient controlled temperature.

After the acquisition procedure, the elaboration of results was gained through the software Scanning Probe Image Processor (SPIP, Image Metrology A/S, Hørsholm, Denmark). The Gaussian filter (ISO 16610-21) was applied to evaluate the roughness parameters (namely, R_a, R_t, R_q and R_{sk}): cut-off length was equal to 0.25 mm and evaluation length to 1.25 mm.

IV.6.2.3 Statistical analysis

The measured roughness values were evaluated using a nonparametric Mann-Whitney (M-W) test and therefore a least significance difference as *post hoc* test. Statistical significance was set at $P < 0.05$. The analyses were, at first, executed comparing the medial ***vs.*** the lateral compartment for each specimen to investigate whether the micro-morphological behavior differs between medial and lateral compartments. Moreover, the authors goal was to understand if prosthesis size influences the surface roughness parameters distribution. Hence, we selected the two largest groups available in our cohort – size 3 and size 4 – and compared medial ***vs.*** lateral roughness parameters using a nonparametric M-W test.

In addition, any possible correlation of the variables “follow-up”, “age at surgery” and “BMI” with the analyzed surface roughness parameters was investigated, using Pearson correlation coefficient.

IV.6.2.4 Multibody simulation

The lower limb model was described in **section IV.5.2**. They were used three different sets of data (namely three different gait patterns), as ground reaction forces. The first one was created with ground reaction forces and kinematic data from Vaughan et al. [218] and the others two were realized by AnyBody research group, recorded in the Gait Lab of Aalborg University: Gait Normal (that simulates a normal walking) and Gait Fast (that simulates a faster walking). The model was validated by comparing its results to the published experimental data from Bergmann et al. [219]. The force and moment were normalized with respect to the body weight of the subject and shown as function of gait cycle, a single step that started and ended with foot contact.

IV.6.3 Results

In **Figure IV.10** are shown six topographies (three for each condyle) obtained as an example of the confocal acquisition results. The 3D images were obtained applying the above-mentioned Gaussian filter on the entire surface, with equal cut-off length along the two directions (0.25 mm). Medial and lateral compartments are on the left and right side of the image, respectively. In this specific insert, the medial and lateral compartments showed similar wear behavior: part a) shows a worn surface with scratches mainly oriented along the A/P direction. Part b) shows less damaged surface than the previous one; thin scratches along the A/P direction, whereas the lateral compartment exhibits an outlier valley in the right edge. In part c) roughness appears elevate in the center-left part of the medial section which also shows evidence of wear with scratches mainly oriented along the A/P direction; lateral portion shows few scratches and a deeper transverse dip on the left.

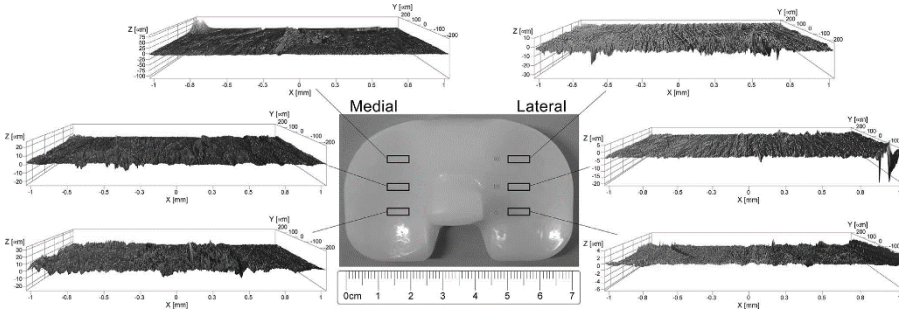

Figure IV.10: *3D topographic images on the lateral side of a tibial component. Gaussian filter was performed on the acquired area.*

Five UHMWPE inserts showed cracking on the edge and/or on the backside surfaces, together with sign of delamination. The remaining six UHMWPE inserts were characterized by mild to moderate scratching. It was emphasized that the most damaged TKAs were those implanted on patients with high BMI values, showing delamination, serious signs of scratching on the A/P direction and pitting on the articulating surface.

IV.6.3.1 Microscopic results

Table IV.2 shows roughness measurements for all the analyzed specimens distinguishing medial and lateral compartment. Retrieved specimens are arranged as function of implant size.

- R_a, R_t an R_q parameters not show a predominant pattern among the different specimens, although in most cases surface roughness of lateral compartment is higher than the medial one.
- R_a values are in good accordance with those obtained from the in-vitro analysis performed by DesJardins et. al. [220], which showed a range of 165—197 nm in the test runs between 1 to 5 million cycles (where 1 million cycle simulate 1 year of *in-vivo* activity).
- Specimen #9 appears to be the only sample with a lateral compartment surface roughness much higher than the medial compartment.
- R_{sk} does not show a pattern that is unique among different samples.

Table IV.2: *Roughness measurements performed on both medial and lateral tibial UHMWPE components.*

Patient	R_a (µm)		R_t (µm)		R_q (µm)		R_{sk}	
	Lateral	Medial	Lateral	Medial	Lateral	Medial	Lateral	Medial
#1	0.253	0.302	2.808	3.553	0.354	0.436	0.780	0.144
#2	1.789	1.648	18.370	17.193	2.515	2.317	-0.187	-0.236
#3	0.944	0.543	10.772	9.048	1.452	0.848	-0.559	0.473

Table IV.2: *Roughness measurements performed on both medial and lateral tibial UHMWPE components.*

Patient	R_a (µm)		R_t (µm)		R_q (µm)		R_{sk}	
	Lateral	Medial	Lateral	Medial	Lateral	Medial	Lateral	Medial
#4	0.836	0.744	11.234	8.252	1.345	1.113	0.609	-0.628
#5	0.326	0.172	4.855	3.733	0.480	0.315	0.543	2.246
#6	0.470	0.735	5.981	8.410	0.675	1.068	-0.634	-0.711
#7	0.503	0.298	4.180	3.240	0.686	0.440	1.053	0.343
#8	0.801	0.646	9.299	7.087	1.179	0.910	-0.816	-1.042
#9	1.798	0.739	17.427	9.276	2.746	1.092	-0.124	-0.732
#10	0.182	0.332	2.779	4.953	0.288	0.560	0.445	-0.238
#11	0.600	1.082	7.507	10.909	0.860	1.510	-0.432	-0.075

IV.6.3.2 Statistical analysis results

Results of nonparametric Mann-Whitney U test (M-W) for the medial *vs.* the lateral compartment of each specimen are shown in **Table IV.3**. Specifically, differences in R_a distribution between medial and lateral compartments were found on 4 specimens.

Nonparametric Mann-Whitney U test (M-W) performed on the subgroups size 3 *vs.* size 4 highlighted an interesting result: R_t and R_q parameter are significant different, on both medial and lateral condyle, when comparing size 3 *vs*. size 4 specimens.

Table IV.3: *Results of Mann-Whitney U test for medial vs. lateral surface roughness distribution. The asymptotic significance is shown. Cases with significant differences in distribution are highlighted in bold.*

Patient	Tibial Spacer			
	R_a	R_{sk}	R_q	R_t
#1	.462	.097	.339	.481
#2	.521	.481	.521	.606
#3	.104	**.008**	.152	.584
#4	.938	**.001**	.719	.563
#5	**.001**	.339	**.007**	**.027**
#6	**.019**	.650	**.019**	.091
#7	**.005**	.521	**.009**	**.034**
#8	.211	.765	.149	.211
#9	.152	**.012**	.308	.521
#10	**.007**	.062	**.023**	.072
#11	.059	.913	**.040**	.074

IV.6.3.3 Simulation results

With respect to the reference system shown in **Figure IV.11**, the resultant force and moment give the following components:

- Medial/Lateral Force, F_x: Force acting in lateral direction of the knee (X axis);
- Anterior/Posterior Force, F_y: Force acting in anterior direction of the knee (Y axis);
- Proximo/Distal Force, F_z: Force acting in the direction of the tibial axis (Z axis), considered positive when act in distal direction;
- Flexion Moment, M_x: Moment around the X axis;
- Lateral Moment, M_y: Moment around the Y axis;
- Axial Moment, M_z: Moment around the Z axis.

Positive moments M_x, M_y, and M_z turn clockwise around their axes.

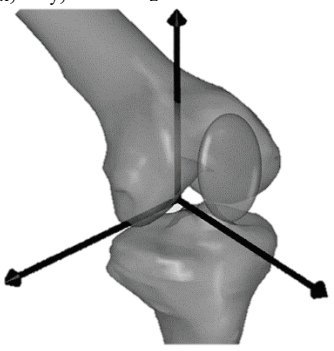

Figure IV.11: *Tibial Based Reference system.*

The behavior of loads and moments during the three types of considered gaits, illustrated in **Figure IV.12** are in good agreement (mainly the Vaughan gait) with those found experimentally by Bergmann [221], which, at the moment, is the standard when comparing calculated knee loads. What matter most for a better comprehension of the different wear of the condyles is the lateral moment, which is negative for a large part of the Vaughan, the Gait Normal and the Gait Fast.

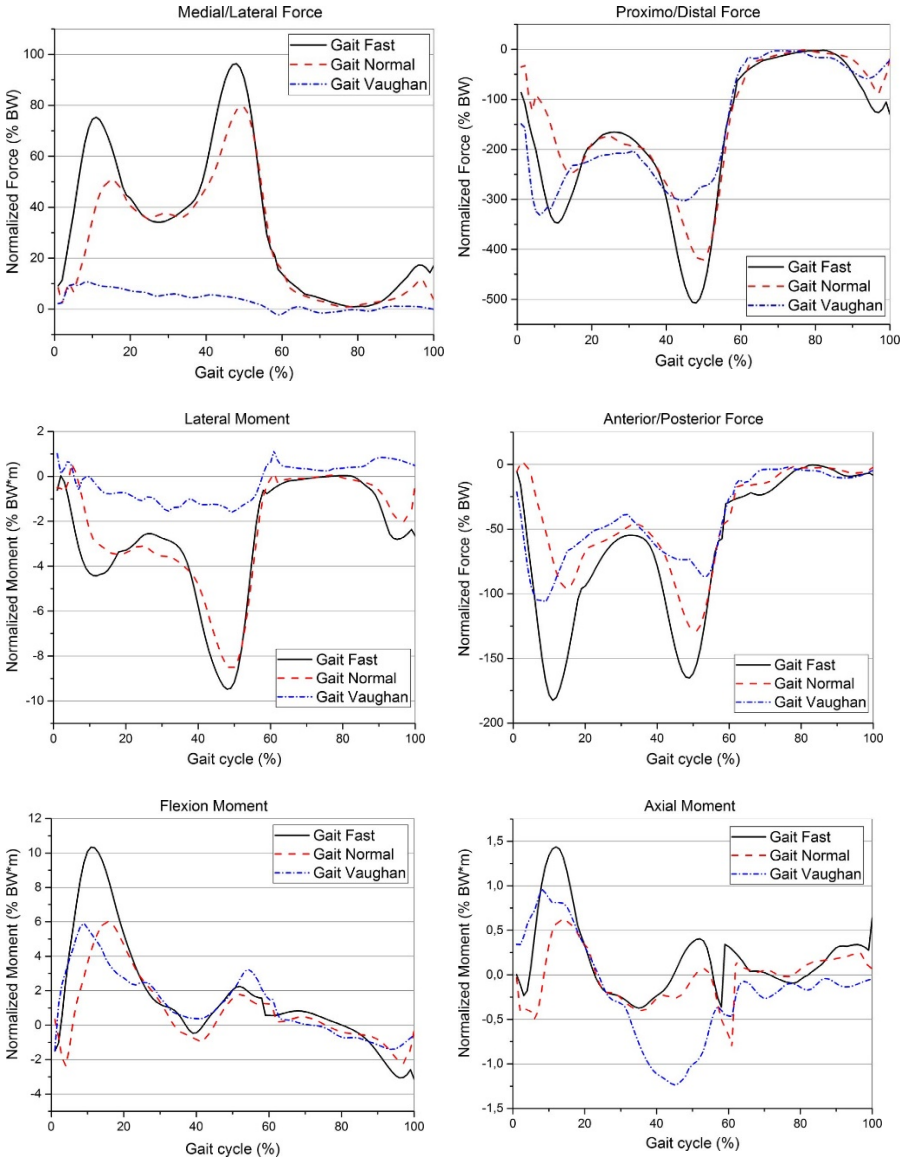

Figure IV.12: *Simulated output vs. experimental data.*

IV.6.4 Discussion

Total Knee Arthroplasty is nowadays a well-established surgical procedure performed to relieve pain and to restore function in knee osteoarthritis [215]. Even though replication of *in vivo* wear behavior on *in vitro* TKR wear tests remains a challenge, identification of damage patterns and acquisition of

surface roughness distribution of retrieved TKAs remains a fundamental step toward understanding tribological phenomena [222], [223].

In our study, we selected 11 retrieved TKAs of the same prosthesis design but with different sizes and different anthropometric features (height, weight, age and time *in situ*) to investigate surface characteristic of medial and lateral compartments. We found irregular wear intensity on the two condyles. Explanation for this behavior must be sought in the results of the multibody model. In fact, the lateral moment has always a negative sign, during the gait cycles. Standing the coordinate system and the convention on the moment, a negative lateral moment means a more intensive stress for the medial condyle – i.e. a higher compression load. This uneven distribution of loads could be considered the main cause of the dissimilar wear observed on the condyles. In fact, in a previous study, Battaglia and co-workers [215], found abrasion and scratching specially on the medial side along antero-posterior (A/P) direction. Delamination, severe signs of scratching along the antero-posterior direction and pitting on the articulating surface were highlighted on the inserts with high BMI/implant size ratio. The tibial inserts showed longitudinal scratches along the A/P direction and burnishing phenomena indicating a predominance of adhesive wear. High stress is, in fact, considered the main cause of the delamination wear in UHMWPE components [224]. Whereas, low stress produce mainly adhesion-abrasion wear, which exponentially decays as contact pressure raises [225].

M-W statistical test performed on medial *vs*. lateral compartments for each specimen of the cohort, showed a different distribution between medial and lateral surface roughness (**Table IV.3**), however the number of cases in which this difference was found is not high enough to outline a trend. Interesting results were observed on size 3 *vs*. size 4 comparison. In fact, in this case, R_q and R_t roughness parameters showed a different distribution in all comparisons. Using the Pearson Correlation Test between surface roughness and patients' characteristics for both femoral and tibial components, a relationship was found. The variable "Age at Surgery" (that is strictly related to patients' level of activities) is positive correlated to surface roughness parameters of tibial components for both medial and lateral condyles.

It has been evidenced that surface roughness affects wear rates and lubrication mechanism in total artificial joints [187]–[189]. Que et al. [187] measured surface roughness of 35 retrieved femoral and tibial components, and analyzed the relations between the femoral component surface damage and patient factors such as weight, age, sex, and total time of implantation. Statistical analysis revealed that these patient factors were all excluded as reasons that significantly affected the surface roughness R_a and PV. The presence of metal beads embedded in the UHMWPE spacer was the only factor that considerably affected the surface roughness of the femoral component. Lakdawala et al. [226] investigated the roughness influence on the failure of 22 retrieved TKA implants after revision surgery. They found

scratches and burnishing on the articular surfaces of the femoral components, nevertheless the differences in surface roughness between the articulating surfaces and the controls – the non-articulating part of the implant – were not statistically significant. After a mean follow-up of 55.6 months the surface finish of these implants did not deteriorate considerably.

From a microscopic point of view, our results confirm that it is not possible to assess if medial compartments surface is rougher than lateral compartments, or *vice versa*. Overall, the research in this field offers contradictory findings. Scholes et al. [2] who examined the surface roughness of 19 retrieved femoral components and these authors found that the surface roughness was more apparent on the lateral condyle than the medial. On the contrary, Brandt et al. [227] observed that "the surface roughness values were higher on the medial condyles than on the lateral condyles" of the 26 retrieved CoCr alloy femoral components. Heyse and coworkers [228] showed a significantly greater surface roughness on the medial condyle than the lateral on 10 CoCr retrievals femoral knee components. In this paper, the Authors claim that even if the unequal wear intensity can be a consequence of the lateral moment – namely a higher compression of the medial condyle –, the roughness of the tibial insert is mainly consequence of the flexion/extension movement. The femoral component, usually manufactured in metal, has higher hardness and its alternative sliding on the softer UHMWPE alters the latter's surface wave pattern. This movement affects both the condyles in equal manner, these two compartments, in fact, did not show sensible roughness dissimilarity. This conclusion is not in contrast with what was stated on the wear, considering that plastic deformation and loss of material can alter surface roughness, but not necessary high wear means high roughness nor the opposite.

The present study has some limitations due to the small number of retrieved TKAs and the lack of information on the level of activity of the considered patients. It was demonstrated that the latter event can have important influence on knee prostheses performance and durability [229]. Performing a study on a group with the same implant design and same type of fixation has allowed us to obtain consistent results and gave some important information about surface characterization of TKA.

IV.6.5 Conclusions

There is a need to standardize measurement of surface roughness in knee prostheses such as the measurement technique and the choice of parameters, to be able to compare results among authors and to better predict the *in vivo* outcome.

The main conclusions obtained in this work are:

- the Authors did not find sizable different roughness between medial and lateral condyles, whereas the calculated loads acting on the tibial plate are in substantial accordance with the observations;

- R_q and R_t surface roughness parameter could discriminate between different implant sizes;
- further studies are necessary to investigate more in depth about this behavior and to support the robustness of this surface metrology investigation.

IV.7 FEM analysis

IV.7.1 Introduction

A major limiting factor to the service life of hard-on-soft total hip replacements remains the wear of the polyethylene acetabular cup. Preclinical endurance testing has become a standard procedure to predict the mechanical performance of new devices during implant development. Wear tests are performed on materials and designs used in prosthetic implants to obtain quality control and acquire further knowledge about the tribological processes in joint prostheses.

By the way, wear tests have a long duration and are very expensive [28], [230], [231]. As the objective of material design through these tests is to improve the durability of prosthetic joints, there is the need to perform simulation close to the in vivo conditions. The wear simulation is run for several million cycles, as it is considered that one million cycles correspond to one year in-vivo [232], [233]. Finite element analysis represents a valid ally in the investigation of joint prostheses performance. It enables to investigate on parameters and boundary conditions that are not manageable experimentally. Thus, it became an ideal tool to predict wear in prosthesis joints. The numerical modelling tool of finite element analysis has been widely applied to analyze the behavior of articular cartilage, joints and bone structures under compressive and tensile stresses. Structural applications include the design and development of replacement joint prosthesis and fracture fixation devices. But it comes in help for predictions of the lifetime of prostheses, evaluating the effects of geometry, loads, or alignment perturbations.

Main aim is to develop an adaptive FE model of a hard-on-soft hip implant capable to replicate dynamic behavior and to compare wear depth contours with experimental results. In these sections, it will be reported the results in terms of total deformation, stress intensity and wear rate per year of an acetabular polyethylene cup.

IV.7.2 Materials and methods

IV.7.2.1 Gait cycle

In this study, it was used a musculoskeletal multibody model, by using the AnyBody Modelling System™, to estimate the loads acting on the hip joint during walking. The procedure was amply described in **section IV.2**.

IV.7.2.2 Finite Element Model

The finite elements model was realized through Ansys® Workbench commercial software. The femoral head was modelled as a rigid body, whereas for the acetabular cup it was selected the UHMWPE GUR 1050 material, **Table IV.4** summarizes its main parameters. The material is assumed to be homogenous, isotropic and linearly elastic. The presence of the pelvic bone has been neglected, since its influence has a negligible effect on contact pressure [234]. The bodies of the FE model are shown in **Figure IV.13**, the mesh was realized through tetrahedral elements and a mesh convergence study was carried out , reaching 3283 total number of nodes, 2012 elements and 383 contact elements.

Table IV.4*: UHMWPE GUR 1050 attributes.*

Density ($kg\ m^{-3}$)	**Young's modulus** (MPa)	**Poisson's ratio** (-)	**Bulk modulus** (MPa)	**Shear modulus** (MPa)	**Tensile yield strength** (MPa)	**Tensile ultimate strength** (MPa)
930	690	0.43	1640	241	21	40

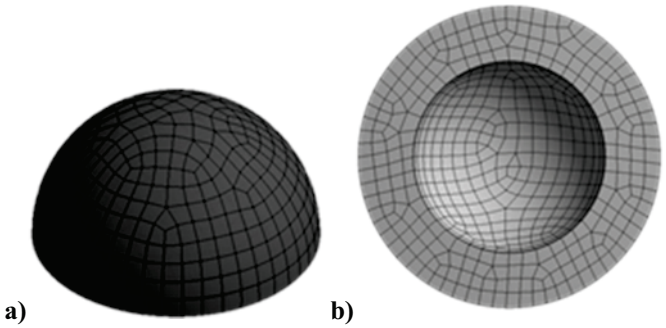

Figure IV.13: *Mesh model of a) the femoral head and b) the acetabular cup.*

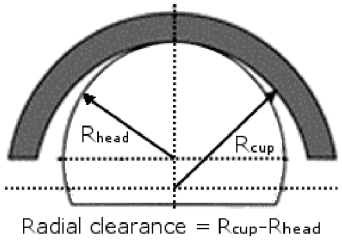

Figure IV.14: *Radial clearance is the difference in radius of the acetabular cup and the femoral head. In this image the clearance is amplified for a better understanding.*

The study was conducted to understand the wear behavior in dry condition, as the presence of lubricant would modify the pressure distribution on the surfaces. But, as further knowledge, it was introduced the influence of the friction coefficient, comparing a dry and a boundary lubrication regime. Namely, a DRY case, i.e. no lubrication, and a WET case, i.e. boundary lubrication. The different values of the friction coefficient were extrapolated from the experimental study on the prosthesis tribological pairs (see **section III.7**). Thus, it was selected a dry friction value of 0.13 and a wet friction value of 0.05.

The femoral head had a diameter of 28 mm, whereas the acetabular cup had a thickness of 5 mm. Moreover, there were studied two geometrical configurations of the coupled bodies: the simulations were executed considering the presence of the radial clearance (CC condition) and not considering it (NC condition). Radial clearance is the difference between the radius of the acetabular cup and the one of the femoral head (see **Figure IV.14**). The results of the two configurations were then compared. As value of clearance it was chose 0.5 mm.

IV.7.2.3 Wear

The results obtained can be applied to the evaluation of the cup wear. The linear wear at any point on the surface for the gait cycle can be derived by modified Archard's wear model as proposed by Uddin and Zhang [235]:

$$W_L = \sum_{i=1}^{n} k\, P_i\, S_i\,, \qquad (IV.12)$$

where W_L is the linear wear, k is the wear factor, n denotes the total number of the instances or time intervals in the gait cycle, P_i and S_i represent the contact stress and sliding distance at the i_{th} discrete instance, respectively.

The wear factor is frequently found from wear tests for a given pair of materials under a given set of conditions. For the couple UHMWPE-metal considered in this study, the wear factor has been reported to be in a broad range of values and varies upon the molecular weight of UHMWPE, the lubricant and the surface roughness of both bodies, and the sterilization procedure [236]. There is also the possibility of using a semiempirical formula, correlating its value to the maximum contact pressure, as in the experimental analysis the wear rate tended to decrease with increasing contact pressure. This relation ca be expressed as [237]:

$$k = 7.99 \times 10^{-6} \sigma_0^{-0.65}\,, \qquad (IV.13)$$

where k is the wear factor in $mm^3/N{\cdot}m{\times}10^6$ cycles and σ_0 is the maximum contact stress in MPa.

As the cumulative linear wear derives from the simple Archard model some hypothesis are needed prior to its application. This model requires a scalar value of the sliding distance and a single value of the surface stress, for each instance of the gait cycle. In this study, it has been considered for each i_{th} discrete instance, the instantaneous value of the highest pressure and the sliding distance of the discrete element subjected to this pressure. Such approximation leaded the authors to exclude those contributions related to elements where smaller values of pressure does not exclude the possibility of

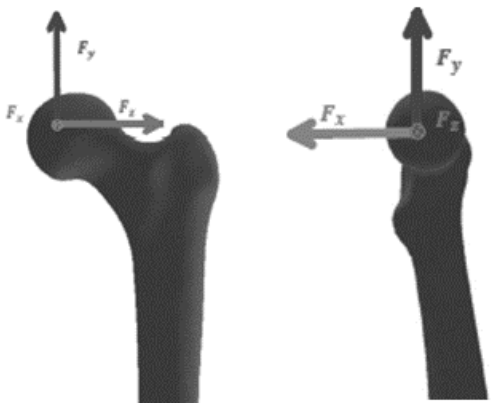

Figure IV.15: *Reference system on the femoral head.*

a mixed lubrication – i.e. where there can be partial or total separation of the sliding surfaces. Furthermore, it was not considered the effect of the linear wear on the geometry of the acetabular cup.

IV.7.3 Results

IV.7.3.1 Pressure and deformation

From the multibody analysis, they were gained the forces and the rotations taking place along the three degrees of freedom. The forces are the Medial/Lateral Force, F_x; Anterior/Posterior Force, F_y; Proximo/Distal Force, F_z (see **Figure IV.15**). The three rotations around the axes are the Flexion/Extension (around Z axes), Abduction/Adduction (around X axes)

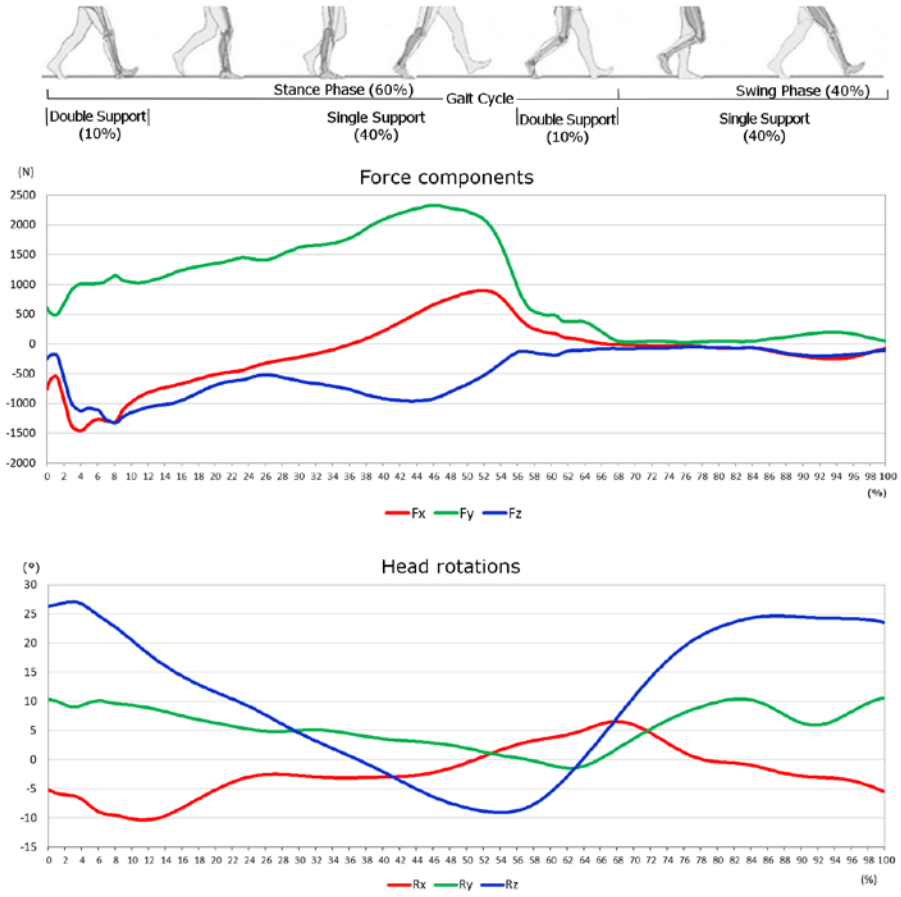

Figure IV.16: *Force vectors and head rotation evolution during the gait cycle.*

and Inward/Outward (around Y axes). In **Figure IV.16** the force components and the rotations derived from the model are shown. It is noticeable that the highest rotation is the Flexion/Extension, whereas the highest load is along the Y axes.

Forces and rotations so obtained, were used as dynamic input for the finite element model. In **Figure IV.17** it is shown the pressure distribution on the internal surface of the insert in different instants of the cycle, with regards to the dry NC condition as exemplificative case. Along with the different orientation of the femoral head it is possible to observe the pressure distribution on the polyethylene insert. Its highest values are found at 8% and 48% of the cycle (respectively **Figure IV.17a** and **c**). In the latter instant it was also found the highest level of the Anterior/Posterior force (see **Figure IV.16**), and the pressure is more concentrated in the edge zone of the insert. In the other two images, **Figure IV.17b** and **17d**, at 26% and 93% of the cycle, the pressure reaches lower values than those described before and its mostly located in the central part of the inner hemisphere. The other geometrical and frictional cases are here omitted for the brevity of exposition, but they presented a similar distribution of pressure, only leading different intensity of the tensional state. These results are in good compliance with the literature [238], [239].

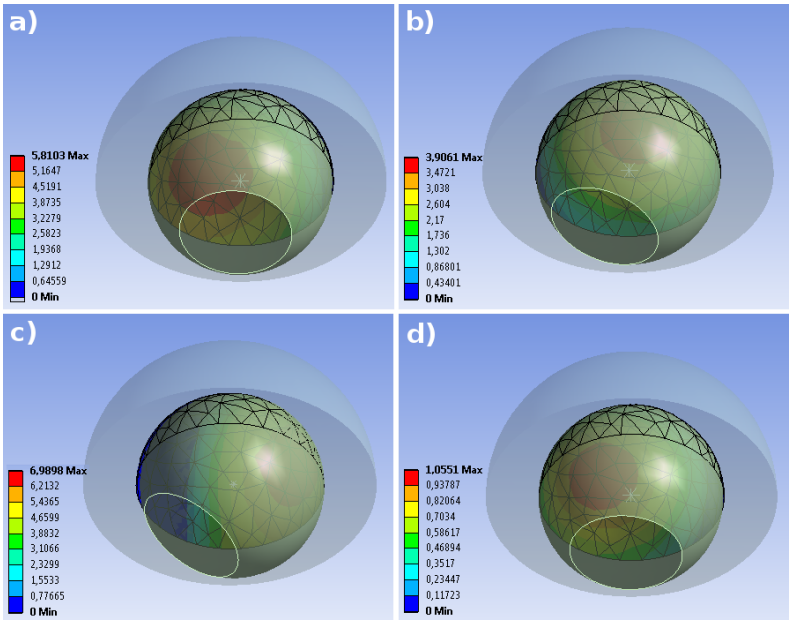

Figure IV.17: *Tensional state distribution on the inner surface of the polyethylene liner in different walking steps.*

In **Figure IV.18a** it is shown the maximum value of pressure, for each instant of the cycle. The maximum value throughout the walking cycle is equal to 7 MPa and it is found around the 45% of the cycle – agreeing with the dynamic analysis. A slightly difference was found between the two friction cases, showing a higher peak value in the wet condition. In **Figure IV.18b** is

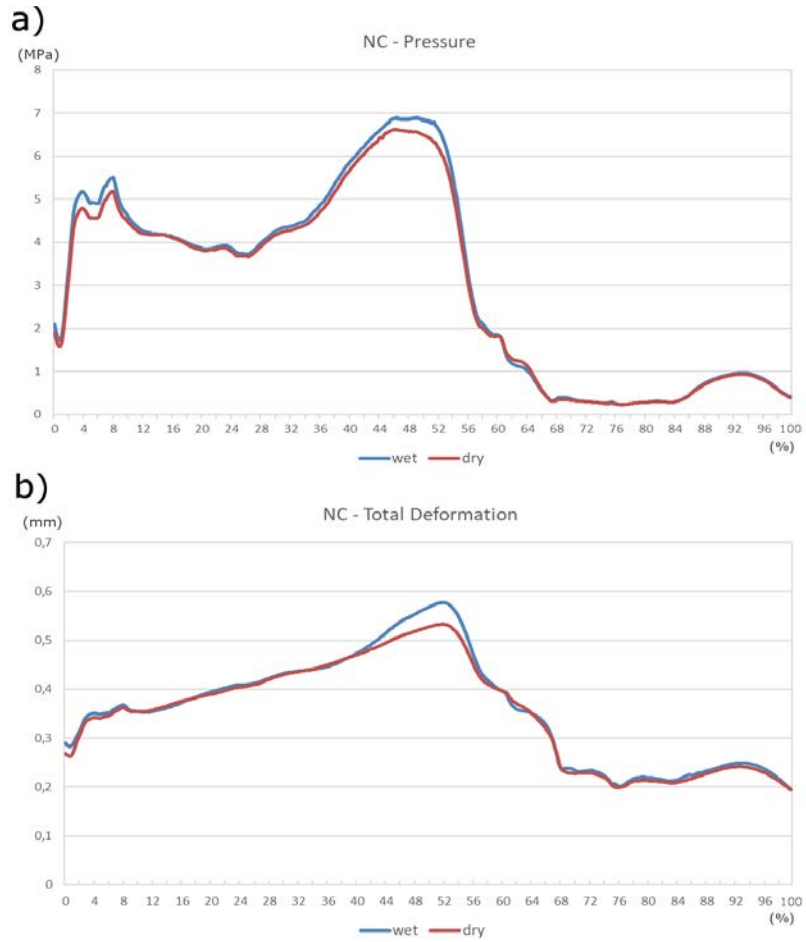

Figure IV.18: *Comparison of result in the configuration without clearance, wet and dry cases.*

displayed the maximum value of the total deformation, its highest value is again related to the wet case, reaching almost 0.6 mm. In **Figure IV.19** it is shown the comparison between the two friction cases considering the presence of the radial clearance. In **Figure IV.19a** the maximum pressure comparison highlights the almost no difference in the two conditions of friction. Whereas, in **Figure IV.19b** the curves have slightly differences, showing higher values of total deformation in the wet condition.

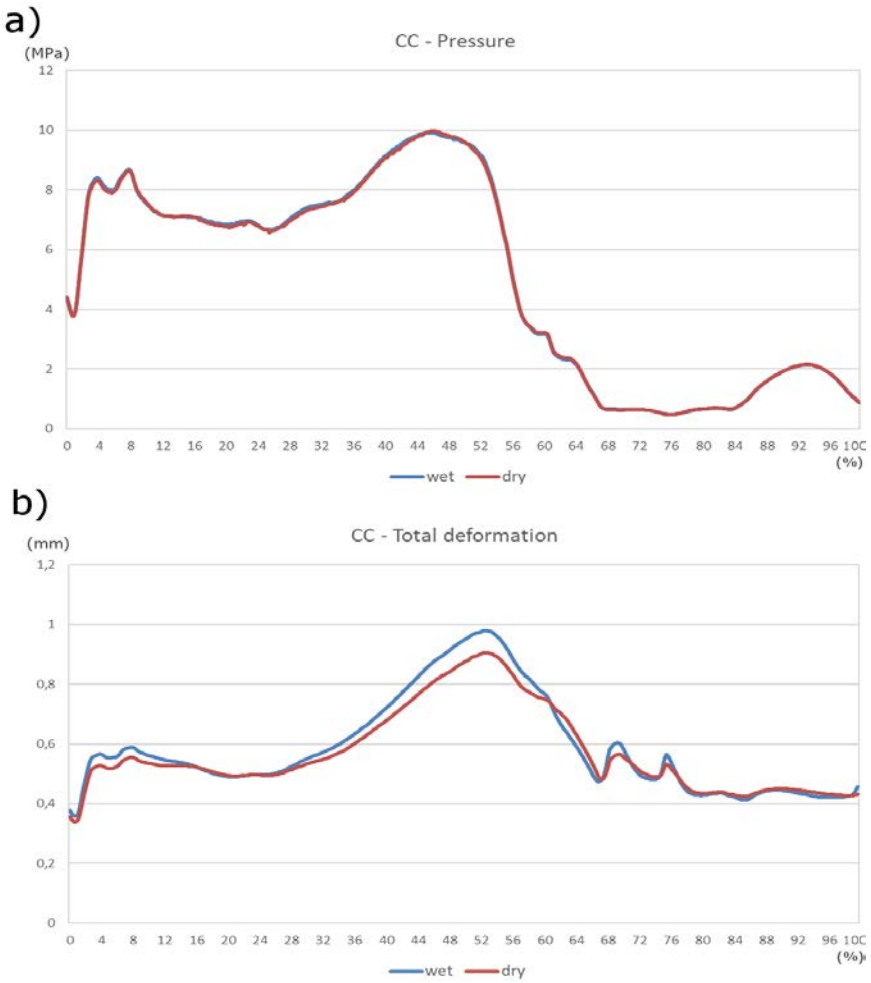

Figure IV.19: *Comparison of result in the configuration with clearance, between the wet and dry cases.*

In **Figure IV.20** there is the comparison of the two geometrical conditions, with and without radial clearance (CC and NC, respectively), considering the boundary lubrication. In **Figure IV.20a** the maximum pressure curves show the large divergence in the two geometrical solutions. As well as the curves in **Figure IV.20b**, where the total deformation is shown, the highest values are found for the CC clearance.

In **Figure IV.21** there is the comparison of the geometrical cases in the dry friction condition. The curves in **Figure IV.21a** also bring out the divergences in the two configurations, being the pressure of the CC higher than the one found for the NC. The highest values are almost 10 MPa and 6.7 MPa for the CC and NC respectively. In **Figure IV.21b** the maximum values of the total

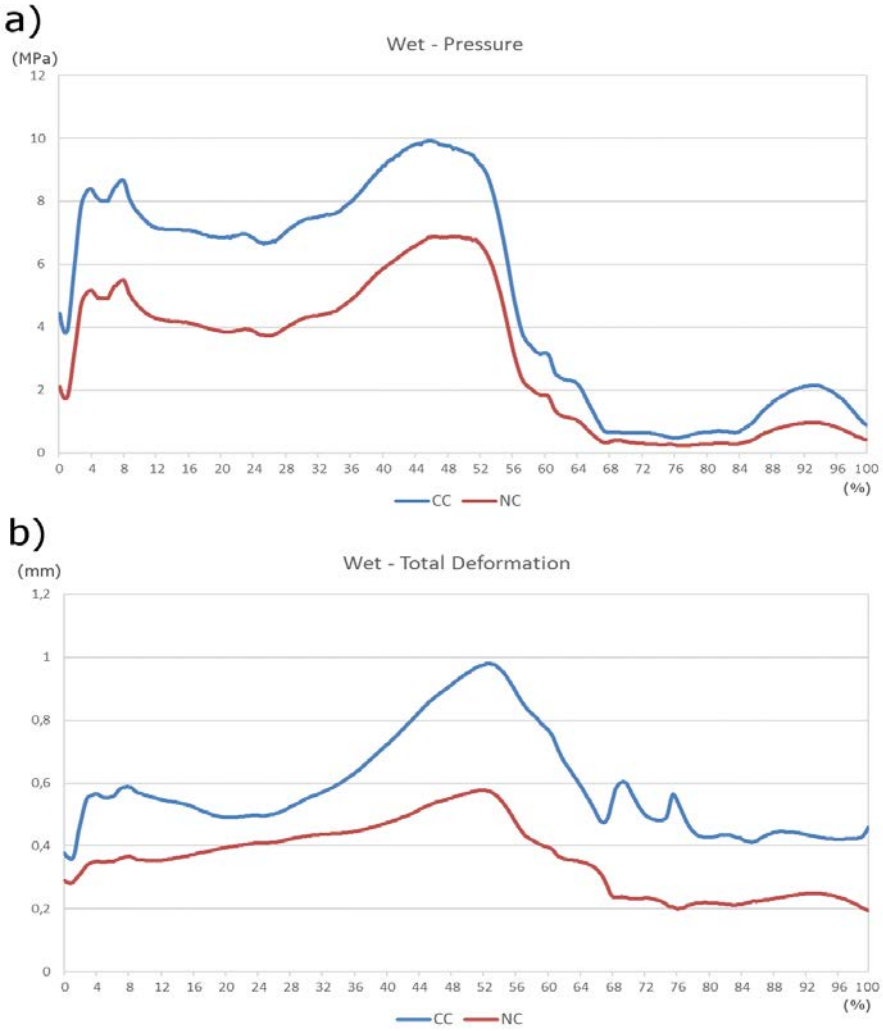

Figure IV.20: *Comparison of result in the dry condition, between the WC and NC cases.*

deformation are compared, and here it is clearly noticeable the difference in the CC and NC conditions. Whereas CC reaches a highest value of 0.9 mm, NC extends to 0.55 mm as maximum.

IV.7.3.2 Wear

As outlined from the results analysis and from the comparison of the different conditions studied, it is believed that the strongest divergences are consequence of the geometrical configuration. Whereas, the friction coefficient has a limited influence on pressure and deformation. Furthermore,

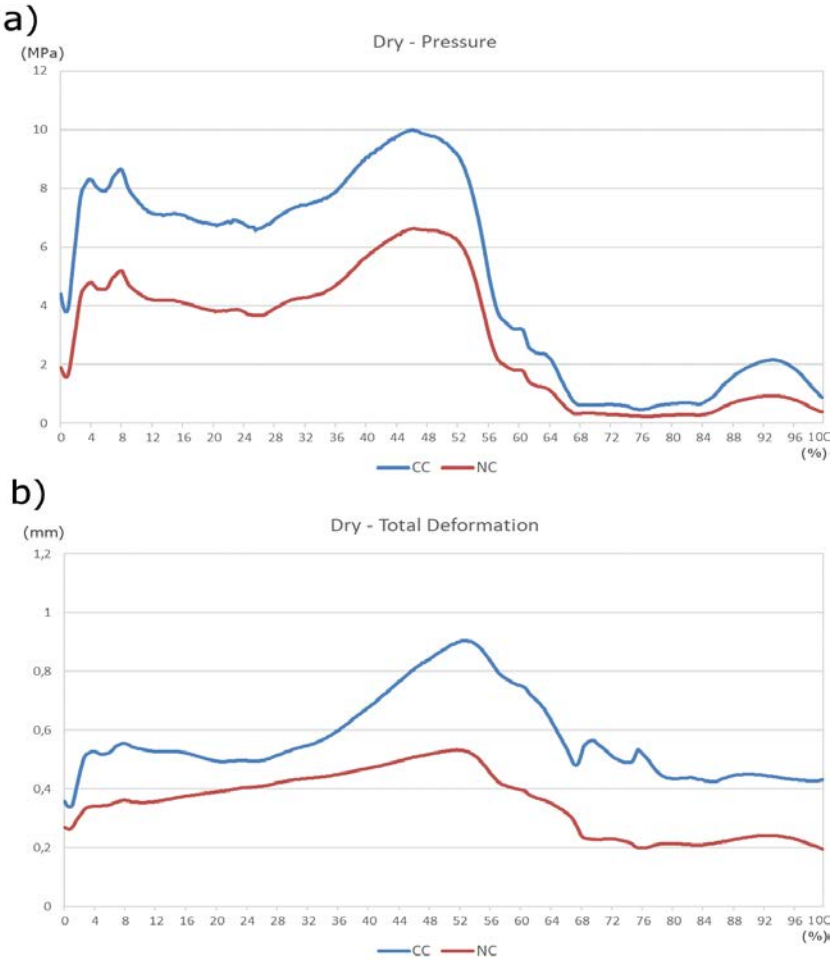

Figure IV.21: *Comparison of result in the dry condition, between the WC and NC cases.*

the lubrication system involves different conditions (as shown in **section III.5.1**), only the solution of the Reynolds Equations could offer a fully understanding of the tensional state and consequently of the wear. Because of these, the cumulative linear wear (**eq. IV.12**) was evaluated in the dry case and obtained in the conditions CC and NC.

Standing the hypothesis on the application of the wear model, the values of the maximum cumulative linear wear were evaluated considering one million of cycles, which is believed to correspond to one year of *in-vivo* employment of the implant. The values in the two cases studied are:

- with radial clearance: 0.99 mm;
- without radial clearance: 0.77 mm.

These results follow the rate found in empirical results, when they were analysed the same hard-on-soft couples. The difference in the experimental findings [240] and this model results are ascribable to the operative conditions of the implants *in-vivo*, where the presence of the synovial liquid acts as lubricant. This lubricant realizes a consistent reduction of the wear rate, that as known from literature [241], is usually equal to one order of magnitude.

The reasons to the differences come across the wear in the two geometrical conditions should be searched in the different tensional state of the surfaces. In the geometry without radial clearance it is realized a conformal contact, meaning that the contact is distributed. On the other hand, when the radial clearance is considered, the contact is non-conformal, it implies that the contact is limited to a small area – ideally a point – that increases its extension as the deformation rises. These differences in the area size led to the distinction of the pressure values, already shown in the previous paragraph.

IV.7.4 Conclusions

Most computational wear analysis [242]–[244] focused on the wear on soft acetabular liner surfaces which articulate against a femoral head. For the ease of computational modelling, they often use very simplified hip kinematic and gait load, such as one-dimensional vertical load, which does not represent actual physiological loading.

In this work it was presented a dynamic load, which considered the variability of the load direction during gait movement. Furthermore, the load and the rotation were derived by a multibody technique applied to a musculoskeletal model, with purpose of a more flexible design. As further aim the implementation of a wear model, as described in the previous section, was made possible by the obtained results.

First, they were obtained the forces and rotations on the hip joint, in the global reference system, by the resolution of the inverse dynamic problem. These data agree with the walking cycle variability, showing how during the stance phase the joint results more loaded than in the swing phase, where there is almost no contact with the ground. Afterwards, these loads and rotation were used as dynamical input in the finite element model, obtaining the pressure distribution, the elastic deformation and the sliding distance on each node of the surface and during the whole gait cycle. The comparison of the different working conditions allowed to conclude that the presence of radial clearance mainly influence the tensional state of the coupled surfaces. Whereas, for a complete understanding of the lubrication influence on the tribology of hip implants they must be involved the Reynolds equations, as varying the coefficient of friction does not allow to establish a sensible difference in results.

Finally, the tensional state and the sliding distance were applied to obtain an indicator of the maximum linear cumulative wear, finding a value of

0.99 mm per year and 0.77 mm per year, respectively with radial clearance and without it. Even though these values are higher than the ones found through empirical analysis, these difference is explicable by considering the absence of lubrication in the model.

V Conclusions

Arthroplasties of hip and knee joints are two of the most widespread and successful surgical procedures of the lasts three decades. Due to the rising in the demanding activities of patients along with their lower and lower age, highly efficiency implants are required. These prostheses should be able to restore the normal ambulation capability of a person and last for a lifetime. Such requirements can be achieved by designing and implanting prostheses with new generation materials, which combine a high biocompatibility with low values of wear rate and friction coefficient. Ceramic and polymeric based composite materials have been reviewed in the second chapter of this thesis. This review highlighted the complex nature itself of these materials, which engages combination and interaction of the multi-phase components, limiting the prediction on the friction and wear behaviour, but defining new high standards in term of tribological performance.

The third chapter of this work has been focused on the different variables that should be taken in account to understand the complex mechanisms in a tribological pair, such as a joint implant. Among those variables, a special attention was dedicated to lubrication and surface roughness. As one of the major issue that affects advanced biomaterials in hip implants is the transfer of metal debris from the surrounding components to the ceramic surface. This phenomenon substantially alters the surface properties of the affected ceramic, by varying its distribution and height of peaks and valleys.

These alterations have been analysed and reported in two cases of study, showing that these metal smears increased some surface roughness parameters, as S_a and S_t. 35 ceramics femoral heads were studied, including zirconia, Biolox® Delta, Biolox® and Biolox® Forte. Comparing the contact and the optical techniques, the statistical M-W Test underlined that no deviation was found for S_{sk} parameter. Furthermore, S_{ku} was always higher than 3, for every ceramic material studied. In the second study on the metal transfer phenomenon, it has been observed a sensibly higher value of the S_t parameter on the common ceramic than on the Biolox® Delta. Moreover, it

was successfully verified the application of a new digital procedure to assess areal coverage by metal transfer. This procedure, based on a 3D non-contact optical scanner, has proven to be suitable for measuring the metal transfer areal coverage. The MT was observed to cover an extension between 29.6 and 573.6 mm^2. It was found a slightly difference of the MT percentage relative to the different materials, finding it maximum value on the Biolox® Forte. As further finding, the MT was mostly located on the superior portion of the heads, at the centre or on a side.

Hip and knee joint prostheses are always subjected to simulation tests before receiving the required approval for clinical use. These tests are performed with the aim of determine the behaviour of the prosthesis and assess the wear rate of the components. However, wear tests on simulators are long and expensive due to the large number of cycles at low frequency that must be executed. Alternatively, to these wear simulators there is the possibility to investigate using standard tribometers. A tribological study on the most widespread tribopairs in joint implants has been conducted and described in chapter three. This investigation has been realized though a reciprocating tribometer, whose motion could reproduce the sliding flexion/extension movement of the joints. This experimental analysis has been conducted to obtain the friction coefficients of UHMWPE against titanium alloy (TiAl6V4), against AISI316L steel and against Al_2O_3. The tests were performed under dry and lubricated conditions, assuring a pressure at the interface that recreate the load condition within a human body. The results showed that the polyethylene paired with stainless steel or titanium alloy have lower frictional coefficient than when paired with the ceramic.

In the fourth chapter of the thesis it has been described the biomechanics governing the motions of the lower limb joints. Moreover, it has been presented the musculoskeletal multibody model of a lower limb, realized through the AnyBody modelling software, by means of an 18 degrees of freedom mechanism. The Gait Analysis was used to assess the human gait, reached by solving the Inverse Dynamics Problem. This model leaded to the simulation of different walking cycles and yielded the loads acting on the joints. They were used three different gait cycles: the first one was created with gait analysis data from Vaughan whereas the others two simulated a normal walking and a faster walking. A study on the wear and roughness of the polyethylene condyles of knee implants has been presented, which focused on the relation between the load distribution and the difference in the condyle surface integrity. Whereas it was not possible to find a statistical significative difference in the roughness distribution on the two condyles, the study shown that R_q and R_t surface roughness parameter could discriminate between different implant sizes.

In the last section of the thesis it is presented the analysis of the tensional state, elastic deformation and linear wear on a hip joint implant through a finite element model. The proposed model consists of hard (metal head) on soft

(UHMWPE cup) implant. Whereas, scientific literature obtains the input parameters from the standardize loads and often limits its application to a static load, this study has been conducted considering the dynamic loads and rotations derived from a musculoskeletal model, with purpose of a more flexible design. In the simulation it has been considered the variability of the load direction during the gait cycle. It was found that the strongest divergences, in term of pressure distribution and elastic deformation of the internal surface of the acetabular cup, are consequence of the geometrical configuration. In other word, the differences are related to the consideration or the exclusion of the radial clearance. Whereas, the friction coefficients considered in this study, and deriving from the experimental analysis, have a limited influence on pressure and deformation. An indicator of the maximum linear cumulative wear was obtained, finding a value of 0.99 mm per year and 0.77 mm per year, respectively with radial clearance and without it. As further aim of the study, it should be taken into consideration the presence of lubricant, evaluating the lubrication regime during the activity cycle. And, during the hydrodynamic regime, solve the governing equation to obtain the tensional state. To make computational wear simulation meaningful, realistic wear models are needed, and those can only be built on experimental data, which calls for systematic investigation in which the relationships between the wear and the prosthetic material properties, relative motion, lubrication and loading are investigated.

VI Bibliography

[1] "Hip | Clinical Gate." [Online]. Available: https://clinicalgate.com/hip-5/. [Accessed: 03-Jan-2018].

[2] S. T. (S. T. Canale, J. H. Beaty, and W. C. (Willis C. Campbell, *Campbell's operative orthopaedics*. Elsevier/Mosby, 2013.

[3] S. L. Delp, A. V. Komattu, and R. L. Wixson, "Superior displacement of the hip in total joint replacement: Effects of prosthetic neck length, neck-stem angle, and anteversion angle on the moment-generating capacity of the muscles," *J. Orthop. Res.*, vol. 12, no. 6, pp. 860–870, Nov. 1994.

[4] N. W. Rydell, "Forces acting on the femoral head-prosthesis. A study on strain gauge supplied prostheses in living persons.," *Acta Orthop. Scand.*, vol. 37, p. Suppl 88:1-132, 1966.

[5] G. Bergmann *et al.*, "Hip forces and gait patterns from rountine activities," *J. Biomech.*, vol. 34, pp. 859–871, 2001.

[6] G. Bergmann, F. Graichen, and A. Rohlmann, "Hip joint loading during walking and running, measured in two patients.," *J. Biomech.*, vol. 26, no. 8, pp. 969–90, Aug. 1993.

[7] G. Bergmann, F. Graichen, and A. Rohlmann, "Is staircase walking a risk for the fixation of hip implants?," *J. Biomech.*, vol. 28, no. 5, pp. 535–53, May 1995.

[8] G. Bergmann, F. Graichen, and A. Rohlmann, "Hip joint contact forces during stumbling," *Langenbeck's Arch. Surg.*, vol. 389, no. 1, pp. 53–59, Feb. 2004.

[9] Society for Biomaterials and Artificial Organs-India., *Trends in biomaterials & artificial organs.* Society for Biomaterials and Artificial Organs-India.

[10] A. S. Voloshin and J. Wosk, "Shock absorption of meniscectomized and painful knees: a comparative in vivo study.," *J. Biomed. Eng.*, vol. 5, no. 2, pp. 157–61, Apr. 1983.

[11] M. Bonnin, *The knee joint : surgical techniques and strategies*.

Springer, 2012.
[12] F. G. Girgis, J. L. Marshall, and A. Monajem, “The cruciate ligaments of the knee joint. Anatomical, functional and experimental analysis.,” *Clin. Orthop. Relat. Res.*, no. 106, pp. 216–31.
[13] A. A. Amis, A. M. J. Bull, C. M. Gupte, I. Hijazi, A. Race, and J. R. Robinson, “Biomechanics of the PCL and related structures: posterolateral, posteromedial and meniscofemoral ligaments,” *Knee Surgery, Sport. Traumatol. Arthrosc.*, vol. 11, no. 5, pp. 271–281.
[14] S. R. Knight, R. Aujla, and S. P. Biswas, “Total Hip Arthroplasty - over 100 years of operative history.,” *Orthop. Rev. (Pavia).*, vol. 3, no. 2, p. e16, Sep. 2011.
[15] D. J. Berry, W. S. Harmsen, M. E. Cabanela, and B. F. Morrey, “Twenty-five-year survivorship of two thousand consecutive primary Charnley total hip replacements: factors affecting survivorship of acetabular and femoral components.,” *J. Bone Joint Surg. Am.*, vol. 84–A, no. 2, pp. 171–177.
[16] J. J. Callaghan, J. C. Albright, D. D. Goetz, J. P. Olejniczak, and R. C. Johnston, “Charnley total hip arthroplasty with cement. Minimum twenty-five-year follow-up.,” *J. Bone Joint Surg. Am.*, vol. 82, no. 4, pp. 487–97, Apr. 2000.
[17] S. Affatato, F. Zanini, and S. Carmignato, “Micro X-Ray Computed Tomography Mass Loss Assessment of Different UHMWPE: A Hip Joint Simulator Study on Standard vs. Cross-Linked Polyethylene,” *PLoS One*, vol. 12, no. 1, p. e0170263, Jan. 2017.
[18] H.-G. Willert and M. Semlitsch, “Reactions of the articular capsule to wear products of artificial joint prostheses,” *J. Biomed. Mater. Res.*, vol. 11, no. 2, pp. 157–164, Mar. 1977.
[19] H. C. Amstutz, P. Campbell, N. Kossovsky, and I. C. Clarke, “Mechanism and clinical significance of wear debris-induced osteolysis.,” *Clin. Orthop. Relat. Res.*, no. 276, pp. 7–18, Mar. 1992.
[20] I. Harding *et al.*, “Serum levels of cobalt and chromium in a complex modular total hip arthroplasty system,” *J. Arthroplasty*, vol. 17, no. 7, pp. 893–895, Oct. 2002.
[21] C. Brockett, S. Williams, Z. Jin, G. Isaac, and J. Fisher, “Friction of total hip replacements with different bearings and loading conditions,” *J. Biomed. Mater. Res. Part B Appl. Biomater.*, vol. 81B, no. 2, pp. 508–515, May 2007.
[22] P. J. Firkins *et al.*, “Quantitative analysis of wear and wear debris from metal-on-metal hip prostheses tested in a physiological hip joint simulator.,” *Biomed. Mater. Eng.*, vol. 11, no. 2, pp. 143–57, 2001.
[23] F. Á. Rodriguez-Gonzalez, “Introduction to biomaterials in orthopaedic surgery,” *Biomater. Orthop. Surg.*, pp. 1–10, 2009.
[24] F. C. Campbell, “Chapter 1: Introduction to Composite Materials,” *Manuf. Process. Adv. Compos.*, p. 30, 2010.

[25] E. Salernitano and C. Migliaresi, “Composite materials for biomedical applications: a review,” *J Appl Biomat Biomech*, vol. 1, pp. 3–18, 2003.

[26] A. Ruggiero, M. Merola, P. Carlone, and V.-M. Archodoulaki, “Tribo-mechanical characterization of reinforced epoxy resin under dry and lubricated contact conditions,” *Compos. Part B Eng.*, vol. 79, pp. 595–603, 2015.

[27] W. D. Kingery, “Introduction to Ceramics,” *Journal of The Electrochemical Society*, vol. 124. p. 152C, 1977.

[28] S. Affatato, M. Testoni, G. L. Cacciari, and A. Toni, “Mixed oxides prosthetic ceramic ball heads. Part 2: effect of the ZrO2 fraction on the wear of ceramic on ceramic joints,” *Biomaterials*, vol. 20, pp. 971–975, 1999.

[29] C. Piconi and G. Maccauro, “Zirconia as a ceramic biomaterial,” *Biomaterials*, vol. 20. pp. 1–25, 1999.

[30] M. Hamadouche and L. Sedel, “Ceramics in orthopaedics.,” *J. Bone Joint Surg. Br.*, vol. 82, pp. 1095–1099, 2000.

[31] J. M. Cuckler, J. Bearcroft, and C. M. Asgian, “Femoral head technologies to reduce polyethylene wear in total hip arthroplasty.,” *Clin. Orthop. Relat. Res.*, no. 317, pp. 57–63, Aug. 1995.

[32] A. Toni *et al.*, “The use of ceramic in prosthetic hip surgery. The state of the art,” *Chir. Organi Mov.*, vol. 80, pp. 13–25, 1995.

[33] M. Vallet-Regi, *Bio-Ceramics with Clinical Applications*. John Wiley & Sons, 2014.

[34] G. Willmann, “Ceramics for total hip replacement - what a surgeon should know,” *Orthopedics*, vol. 21(2), pp. 173–177, 1998.

[35] E. J. Henssge, I. Bos, and G. Willmann, “Al2O3 against Al2O3 combination in hip endoprostheses. Histological investigations with semiquantitative grading of revision and autopsy cases and abrasion measures.,” *J Mater. Sci. Mater Med.*, vol. 5, 1994.

[36] Hsu and M. C. Shen, “Ceramic Wear Maps,” *Wear,* vol. 200, pp. 154–175, 1996.

[37] H. A. McKellop, “Bearing surfaces in total hip replacements: State of the art and future developments.,” *Instr Course Lect.* , vol. 50, pp. 165–179, 2001.

[38] B. Derbyshire, J. Fisher, D. Dowson, C. Hardaker, and K. Brummitt, “Comparative study of the wear of UHMWPE with zirconia ceramic and stainless steel femoral heads in artificial hip joints.,” *Med. Eng. Phys.*, vol. 16, no. 3, pp. 229–236, 1994.

[39] B. Cales, Y. Stefani, and E. Lilley, “Long-term in vivo and in vitro aging of a zirconia ceramic used in orthopaedy.,” *J. Biomed. Mater. Res.*, vol. 28, no. 5, pp. 619–624, 1994.

[40] G. Willmann, H. J. Fruh, and H. G. Pfaff, “Wear characteristics of sliding pairs of zirconia (Y-TZP) for hip endoprostheses,”

Biomaterials, vol. 17(22), pp. 2157–2162, 1996.
[41] C. Piconi, G. Maccauro, L. Pilloni, W. Burger, F. Muratori, and H. G. Richter, "On the fracture of a zirconia ball head," *J. Mater. Sci. Mater. Med.*, vol. 17, no. 3, pp. 289–300, 2006.
[42] C. Piconi, G. Maccauro, F. Muratori, and E. Brach Del Prever, "Alumina and zirconia ceramics in joint replacements.," *J. Appl. Biomater. Biomech.*, vol. 1, pp. 19–32, 2003.
[43] J. Rieu and P. Goeuriot, "Ceramic composites for biomedical applications.," *Clin. Mater.*, vol. 12, no. 4, pp. 211–7, 1993.
[44] F. Macchi, "ALUMINA CERAMICS IN JOINT PROSTHESES," *J. Bone Jt. Surgery, British\r\n Vol.*, vol. 87–B, no. SUPP II, pp. 187–188, Apr. 2005.
[45] R. Gadow and F. Kern, "Novel zirconia-alumina nanocomposites combining high strength and toughness," in *Advanced Engineering Materials*, 2010, vol. 12, pp. 1220–1223.
[46] G. W. Oehlert, "A note on the delta method," *Am. Stat.*, vol. 46, pp. 27–29, 1992.
[47] S. Deville *et al.*, "Low-temperature ageing of zirconia-toughened alumina ceramics and its implication in biomedical implants," *J. Eur. Ceram. Soc.*, vol. 23, no. 15, pp. 2975–2982, 2003.
[48] D. Gutknecht, J. Chevalier, V. Garnier, and G. Fantozzi, "Key role of processing to avoid low temperature ageing in alumina zirconia composites for orthopaedic application," *J. Eur. Ceram. Soc.*, vol. 27, no. 2–3, pp. 1547–1552, 2007.
[49] T. D. Stewart, J. L. Tipper, G. Insley, R. M. Streicher, E. Ingham, and J. Fisher, "Long-term wear of ceramic matrix composite materials for hip prostheses under severe swing phase microseparation," *J Biomed Mater Res B Appl Biomater*, vol. 66, no. 2, pp. 567–573, Aug. 2003.
[50] M. Knepper, B. K. Milthorpe, and S. Moricca, "Interdiffusion in short-fibre reinforced hydroxyapatite ceramics," *J. Mater. Sci. Mater. Med.*, vol. 9, no. 10, pp. 589–596, 1998.
[51] Z. J. Shen, E. Adolfsson, M. Nygren, L. Gao, H. Kawaoka, and K. Niihara, "Dense Hydroxyapatite-Zirconia Ceramic Composites with High Strength for Biological Applications," *Adv. Mater.*, vol. 13, no. 3, pp. 214–216, Feb. 2001.
[52] J. Sun, L. Gao, and W. Li, "Colloidal Processing of Carbon Nanotube / Alumina Composites," *Chem. Mater.*, vol. 14, no. 16, pp. 5169–5172, 2002.
[53] J. W. An and D. S. Lim, "Synthesis and characterization of alumina/carbon nanotube composite powders," *J. Ceram. Process. Res.*, vol. 3, no. 3 PART 2, pp. 174–177, 2002.
[54] Y. F. Zhu, L. Shi, J. Liang, D. Hui, and K. T. Lau, "Synthesis of zirconia nanoparticles on carbon nanotubes and their potential for enhancing the fracture toughness of alumina ceramics," *Compos. Part*

B Eng., vol. 39, no. 7–8, pp. 1136–1141, 2008.

[55] S. Ramakrishna, J. Mayer, E. Wintermantel, and K. W. Leong, "Biomedical applications of polymer-composite materials: a review," *Compos. Sci. Technol.*, vol. 61, no. 9, pp. 1189–1224, Jul. 2001.

[56] Z. D. Mikić and A. R. Lesić, "50 years of total hip prosthesis--a tribute to Prof. Sir John Charnley," *Acta Chir. Iugosl.*, vol. 60, no. 1, pp. 9–13, Jan. 2013.

[57] Dupont, "Teflon PTFE ® Properties Handbook," p. 38.

[58] J. Blumm, A. Lindemann, M. Meyer, and C. Strasser, "Characterization of PTFE using advanced thermal analysis techniques," in *International Journal of Thermophysics*, 2010, vol. 31, no. 10, pp. 1919–1927.

[59] S. M. Kurtz, O. K. Muratoglu, M. Evans, and A. A. Edidin, "Advances in the processing, sterilization, and crosslinking of ultra-high molecular weight polyethylene for total joint arthroplasty," *Biomaterials*, vol. 20, no. 18, pp. 1659–1688, 1999.

[60] M. C. Sobieraj and C. M. Rimnac, "Ultra high molecular weight polyethylene: Mechanics, morphology, and clinical behavior," *Journal of the Mechanical Behavior of Biomedical Materials*, vol. 2. pp. 433–443, 2009.

[61] S. M. Kurtz, *UHMWPE Biomaterials Handbook*. Elsevier, 2009.

[62] a Wang, C. Stark, and J. H. Dumbleton, "Role of cyclic plastic deformation in the wear of UHMWPE acetabular cups.," *J. Biomed. Mater. Res.*, vol. 29, no. 5, pp. 619–626, 1995.

[63] H. McKellop, F. W. Shen, B. Lu, P. Campbell, and R. Salovey, "Development of an extremely wear-resistant ultra high molecular weight polyethylene for total hip replacements.," *J. Orthop. Res.*, vol. 17, no. 2, pp. 157–167, 1999.

[64] O. K. Muratoglu *et al.*, "Larger diameter femoral heads used in conjunction with a highly cross-linked ultra–high molecular weight polyethylene: A new concept," *J. Arthroplasty*, vol. 16, no. 8, pp. 24–30, Dec. 2001.

[65] J. R. Atkinson and R. Z. Cicek, "Silane cross-linked polyethylene for prosthetic applications. Part I. Certain physical and mechanical properties related to the nature of the material," *Biomaterials*, vol. 4, no. 4, pp. 267–275, 1983.

[66] S. M. Kurtz, O. K. Muratoglu, M. Evans, and A. A. Edidin, "Advances in the processing, sterilization, and crosslinking of ultra-high molecular weight polyethylene for total joint arthroplasty," *Biomaterials*, vol. 20. pp. 1659–1688, 1999.

[67] H. Oonishi, Y. Kadoya, and S. Masuda, "Gamma-irradiated cross-linked polyethylene in total hip replacements--analysis of retrieved sockets after long-term implantation.," *J. Biomed. Mater. Res.*, vol. 58, no. 2, pp. 167–71, Jan. 2001.

[68] A. A. Edidin, L. Pruitt, C. W. Jewett, D. J. Crane, D. Roberts, and S. M. Kurtz, "Plasticity-induced damage layer is a precursor to wear in radiation-cross-linked UHMWPE acetabular components for total hip replacement. Ultra-high-molecular-weight polyethylene.," *J. Arthroplasty*, vol. 14, no. 5, pp. 616–627, 1999.

[69] E. Oral and O. K. Muratoglu, "Radiation cross-linking in ultra-high molecular weight polyethylene for orthopaedic applications," *Nucl. Instruments Methods Phys. Res. Sect. B Beam Interact. with Mater. Atoms*, vol. 265, no. 1, pp. 18–22, 2007.

[70] W. H. Harris and O. K. Muratoglu, "A Review of Current Cross-linked Polyethylenes Used in Total Joint Arthroplasty," *Clin. Orthop. Relat. Res.*, vol. NA;, no. 430, pp. 46–52, Jan. 2005.

[71] S. J. Burnett and D. Abos, "Total hip arthroplasty: Techniques and results," *BB Med. J.*, vol. 52, no. November, pp. 455–464, 2010.

[72] N. Rushton and T. Rae, "The intra-articular response to particulate carbon fibre reinforced high density polyethylene and its constituents: An experimental study in mice," *Biomaterials*, vol. 5, pp. 352–356, 1984.

[73] R. Bader, E. Steinhauser, H. Rechl, W. Siebels, W. Mittelmeier, and R. Gradinger, "Carbon fiber-reinforced plastics as implant materials," *Orthopade*, vol. 32, pp. 32–40, 2003.

[74] M. Deng and S. W. Shalaby, "Properties of self-reinforced ultra-high-molecular-weight polyethylene composites," *Biomaterials*, vol. 18, no. 9, pp. 645–655, 1997.

[75] W. R. J O Galante, "Unbound MEDLINE : Wear in total hip prostheses. An experimental evaluation of candidate material," 1973. .

[76] W. Rostoker and J. O. Galante, "Indentation creep of polymers for human joint applications.," *J. Biomed. Mater. Res.*, vol. 13, no. 5, pp. 825–8, Sep. 1979.

[77] W. Rostoker and J. O. Galante, "Some new studies of the wear behavior of ultrahigh molecular weight polyethylene.," *J. Biomed. Mater. Res.*, vol. 10, no. 2, pp. 303–10, Mar. 1976.

[78] E. Sclippa and K. Piekarski, "Carbon fiber reinforced polyethylene for possible orthopedic uses," *J. Biomed. Mater. Res.*, vol. 7, no. 1, pp. 59–70, Jan. 1973.

[79] G. M. Connelly, C. M. Rimnac, T. M. Wright, R. W. Hertzberg, and J. A. Manson, "Fatigue crack propagation behavior of ultrahigh molecular weight polyethylene.," *J. Orthop. Res.*, vol. 2, no. 2, pp. 119–25, Jan. 1984.

[80] E. J. Olson, J. D. Kang, F. H. Fu, H. I. Georgescu, G. C. Mason, and C. H. Evans, "The biochemical and histological effects of artificial ligament wear particles: in vitro and in vivo studies.," *Am. J. Sports Med.*, vol. 16, no. 6, pp. 558–70, Jan. .

[81] A. Brandwood, K. R. Noble, and K. Schindhelm, "Phagocytosis of

carbon particles by macrophages in vitro.," *Biomaterials*, vol. 13, no. 9, pp. 646–8, Jan. 1992.
[82] "Biological Responses to PEEK-Based Wear Debris." .
[83] "Developing PEEK Polymer as a Bearing Material for Implants | MDDI Medical Device and Diagnostic Industry News Products and Suppliers." .
[84] H. McKellop, I. Clarke, K. Markolk, and H. Amstutz, "Friction and wear properties of polymer, metal and ceramic prosthetic joint materials evaluated on a multichannel screening device.," *J Biomed Mater Res*, vol. 15, pp. 619–623, 1981.
[85] J. F. Mano, R. a. Sousa, L. F. Boesel, N. M. Neves, and R. L. Reis, "Bioinert, biodegradable and injectable polymeric matrix composites for hard tissue replacement: State of the art and recent developments," *Compos. Sci. Technol.*, vol. 64, pp. 789–817, 2004.
[86] R. M. Streicher, M. Schmidt, and S. Fiorito, "Nanosurfaces and nanostructures for artificial orthopedic implants.," *Nanomedicine (Lond).*, vol. 2, no. 6, pp. 861–874, 2007.
[87] B. B. Johnson, M. H. Santare, J. E. Novotny, and S. G. Advani, "Wear behavior of Carbon Nanotube/High Density Polyethylene composites," *Mech. Mater.*, vol. 41, no. 10, pp. 1108–1115, 2009.
[88] J. A. Puértolas and S. M. Kurtz, "Evaluation of carbon nanotubes and graphene as reinforcements for UHMWPE-based composites in arthroplastic applications: A review," *J. Mech. Behav. Biomed. Mater.*, vol. 39, pp. 129–145, 2014.
[89] W. J. Wood, R. G. Maguire, and W. H. Zhong, "Improved wear and mechanical properties of UHMWPE-carbon nanofiber composites through an optimized paraffin-assisted melt-mixing process," *Compos. Part B Eng.*, vol. 42, no. 3, pp. 584–591, 2011.
[90] N. A. Kotov, "Materials science: carbon sheet solutions.," *Nature*, vol. 442. pp. 254–255, 2006.
[91] C. Soldano, A. Mahmood, and E. Dujardin, "Production, properties and potential of graphene," *Carbon*, vol. 48. pp. 2127–2150, 2010.
[92] A. K. Geim and A. H. MacDonald, "Graphene: Exploring carbon flatland," *Phys. Today*, vol. 60, pp. 35–41, 2007.
[93] Y. Si and E. T. Samulski, "Synthesis of water soluble graphene," *Nano Lett.*, vol. 8, pp. 1679–1682, 2008.
[94] D. R. Dreyer, S. Park, C. W. Bielawski, and R. S. Ruoff, "The chemistry of graphene oxide.," *Chem. Soc. Rev.*, vol. 39, no. 1, pp. 228–240, 2010.
[95] Y. Zhu *et al.*, "Graphene and graphene oxide: synthesis, properties, and applications.," *Adv. Mater.*, vol. 22, pp. 3906–3924, 2010.
[96] Y. Chen, C. Tan, H. Zhang, and L. Wang, "Two-dimensional graphene analogues for biomedical applications," *Chem. Soc. Rev.*, Dec. 2015.
[97] T. Kuilla, S. Bhadra, D. Yao, N. H. Kim, S. Bose, and J. H. Lee,

"Recent advances in graphene based polymer composites," *Prog. Polym. Sci.*, vol. 35, pp. 1350–1375, 2010.

[98] S. Suñer, R. Joffe, J. L. Tipper, and N. Emami, "Ultra high molecular weight polyethylene/graphene oxide nanocomposites: Thermal, mechanical and wettability characterisation," *Compos. Part B Eng.*, vol. 78, pp. 185–191, 2015.

[99] K. Yang, J. Wan, S. Zhang, Y. Zhang, S.-T. Lee, and Z. Liu, "In vivo pharmacokinetics, long-term biodistribution, and toxicology of PEGylated graphene in mice.," *ACS Nano*, vol. 5, no. 1, pp. 516–22, Jan. 2011.

[100] X. Yan, J. Chen, J. Yang, Q. Xue, and P. Miele, "Fabrication of free-standing, electrochemically active, and biocompatible graphene oxide-polyaniline and graphene-polyaniline hybrid papers," *ACS Appl. Mater. Interfaces*, vol. 2, no. 9, pp. 2521–2529, 2010.

[101] Y. Chen, Y. Qi, Z. Tai, X. Yan, F. Zhu, and Q. Xue, "Preparation, mechanical properties and biocompatibility of graphene oxide/ultrahigh molecular weight polyethylene composites," *Eur. Polym. J.*, vol. 48, no. 6, pp. 1026–1033, 2012.

[102] D. Lahiri, F. Hec, M. Thiesse, A. Durygin, C. Zhang, and A. Agarwal, "Nanotribological behavior of graphene nanoplatelet reinforced ultra high molecular weight polyethylene composites," *Tribol. Int.*, vol. 70, pp. 165–169, 2014.

[103] G. M. Jenkins and F. X. de Carvalho, "Biomedical applications of carbon fibre reinforced carbon in implanted prostheses," *Carbon N. Y.*, vol. 15, no. 1, pp. 33–37, 1977.

[104] T. Fu, L. P. He, Y. Han, K. W. Xu, and Y. W. Mai, "Induction of bonelike apatite on carbon-carbon composite by sodium silicate," *Mater. Lett.*, vol. 57, no. 22–23, pp. 3500–3503, 2003.

[105] H. Jianfeng, L. Juanying, C. Liyun, and Z. Liping, "Preparation and properties of carbon fiber/ hydroxyapatite-poly(methyl methacrylate) biocomposites," *J. Appl. Polym. Sci.*, vol. 23, no. 2, p. NA-NA, Jan. 2009.

[106] J. R. H. Foran and S. J. Fischer, "Unicompartmental Knee Replacement - OrthoInfo," 2016. [Online]. Available: https://orthoinfo.aaos.org/en/treatment/unicompartmental-knee-replacement. [Accessed: 04-Jan-2018].

[107] S. Affatato, F. Traina, M. De Fine, S. Carmignato, and A. Toni, "Alumina-on-alumina hip implants: A wear study of retrieved components.," *J. Bone Joint Surg. Br.*, vol. 94, no. 1, pp. 37–42, Jan. 2012.

[108] J. E. Nevelos, E. Ingham, C. Doyle, A. B. Nevelos, and J. Fisher, "The influence of acetabular cup angle on the wear of 'Biolox Forte' alumina ceramic bearing couples in a hip joint simulator," *J Mater. Sci. Mater Med.*, vol. 12, pp. 141–144, 2001.

[109] M. Manaka, I. C. Clarke, K. Yamamoto, T. Shishido, A. Gustafson, and A. Imakiire, "Stripe wear rates in alumina THR--comparison of microseparation simulator study with retrieved implants.," *J. Biomed. Mater. Res. B. Appl. Biomater.*, vol. 69, no. 2, pp. 149–57, May 2004.

[110] J. Nevelos *et al.*, "Microseparation of the centers of alumina-alumina artificial hip joints during simulator testing produces clinically relevant wear rates and patterns," *J Arthroplast.*, vol. 15, no. 6, pp. 793–795, 2000.

[111] S. Affatato, F. Traina, and A. Toni, "Microseparation and stripe wear in alumina-on-alumina hip implants.," *Int. J. Artif. Organs*, vol. 34, no. 6, pp. 506–12, 2011.

[112] Y.-H. Kim, A. Ritchie, and C. Hardaker, "Surface roughness of ceramic femoral heads after in vivo transfer of metal: correlation to polyethylene wear.," *J. Bone Joint Surg. Am.*, vol. 87, no. 3, pp. 577–82, Mar. 2005.

[113] B. S. Bal, M. N. Rahaman, T. Aleto, F. S. Miller, F. Traina, and A. Toni, "The significance of metal staining on alumina femoral heads in total hip arthroplasty.," *J. Arthroplasty*, vol. 22, no. 1, pp. 14–9, Jan. 2007.

[114] C. Restrepo, J. Parvizi, S. M. Kurtz, P. F. Sharkey, W. J. Hozack, and R. H. Rothman, "The Noisy Ceramic Hip: Is Component Malpositioning the Cause?," *J. Arthroplasty*, vol. 23, no. 5, pp. 643–649, 2008.

[115] I. M. Tomek, J. H. Currier, M. B. Mayor, and D. W. Van Citters, "Metal transfer on a ceramic head with a single rim contact.," *J. Arthroplasty*, vol. 27, no. 2, p. 324.e1-4, 2012.

[116] F. a Müller *et al.*, "Transfer of metallic debris after dislocation of ceramic femoral heads in hip prostheses.," *Arch. Orthop. Trauma Surg.*, vol. 126, no. 3, pp. 174–80, Apr. 2006.

[117] B. C. Chong, J. Y. Jeong, S. S. Won, J. K. Deug, K. H. Koo, and H. J. Kim, "Transfer of metallic debris from the metal surface of an acetabular cup to artificial femoral heads by scraping: Comparison between alumina and cobalt-chrome heads," *J. Biomed. Mater. Res. - Part B Appl. Biomater.*, vol. 85, no. 1, pp. 204–209, 2008.

[118] P. Taddei, A. Ruggiero, E. Pavoni, and S. Affatato, "Transfer of metallic debris after in vitro ceramic-on-metal simulation: Wear and degradation in Biolox® Delta composite femoral heads," *Compos. Part B Eng.*, 2016.

[119] S. T. Tzeng and E. Saibel, "Surface Roughness Effect on Slider Bearing Lubrication," *A S L E Trans.*, vol. 10, no. 3, pp. 334–348, Jan. 1967.

[120] N. Patir and H. S. Cheng, "An Average Flow Model for Determining Effects of Three-Dimensional Roughness on Partial Hydrodynamic Lubrication," *J. Lubr. Technol.*, vol. 100, no. 1, p. 12, 1978.

[121] N. Patir and H. S. Cheng, “Application of Average Flow Model to Lubrication Between Rough Sliding Surfaces.pdf,” *Trans. ASME*, vol. 101, no. April, pp. 220–230, 1979.
[122] C. Gachot, A. Rosenkranz, S. M. Hsu, and H. L. Costa, “A critical assessment of surface texturing for friction and wear improvement,” *Wear*, vol. 372, pp. 21–41, 2017.
[123] C. Chevillotte, R. T. Trousdale, K.-N. An, D. Padgett, and T. Wright, “Retrieval analysis of squeaking ceramic implants: are there related specific features?,” *Orthop. Traumatol. Surg. Res.*, vol. 98, no. 3, pp. 281–7, May 2012.
[124] T. Eickmann, M. Manaka, I. C. Clarke, and A. Gustafson, “Squeaking and Neck-Socket Impingement in a Ceramic Total Hip Arthroplasty,” *Key Eng. Mater.*, vol. 240–242, pp. 849–852, 2003.
[125] C. Chevillotte, R. T. Trousdale, Q. Chen, O. Guyen, and K.-N. An, “‘Hip Squeaking’: A Biomechanical Study of Ceramic-on-ceramic Bearing Surfaces,” *Clin. Orthop. Relat. Res.*, vol. 468, no. 2, pp. 345–350, Feb. 2010.
[126] E. K. Fredette *et al.*, “Does metal transfer differ on retrieved ceramic and CoCr femoral heads?,” *Biomed Res. Int.*, vol. 2015, 2015.
[127] K. L. Johnson, K. Kendall, A. D. Roberts, and K. L. Johnsont, “Surface Energy and the Contact of Elastic Solids,” *Source Proc. R. Soc. London. Ser. A, Math. Phys. Sci.*, vol. 324, no. 324, pp. 301–313, 1971.
[128] C. Yang, *Role of surface roughness in tribology from atomic to macroscopic scale*. Forschungszentrum, Zentralbibliothek, 2008.
[129] T. R. Thomas, *Rough Surfaces*, Second. London: Iperial College Press, 1999.
[130] J. A. Greenwood and J. B. P. Williamson, “Contact of Nominally Flat Surfaces,” *Proc. R. Soc. A Math. Phys. Eng. Sci.*, vol. 295, no. 1442, pp. 300–319, Dec. 1966.
[131] M. Ciavarella, J. A. Greenwood, and M. Paggi, “Inclusion of ‘interaction’ in the Greenwood and Williamson contact theory,” *Wear*, vol. 265, no. 5–6, pp. 729–734, Aug. 2008.
[132] S. Ilincic, N. Tungkunagorn, A. Vernes, G. Vorlaufer, P. A. Fotiu, and F. Franek, “Finite and boundary element method contact mechanics on rough, artificial hip joints,” *Proc. Inst. Mech. Eng. Part J J. Eng. Tribol.*, vol. 225, no. 11, pp. 1081–1091, Nov. 2011.
[133] D. Zhu and Y. Z. Hu, “The study of transition from full film elastohydrodynamic to mixed and boundary lubrication,” *Proc. STLE/ASME*, no. May, pp. 150–156, 1999.
[134] T. V. Vorburger and E. C. Teague, “Optical techniques for on-line measurement of surface topography,” *Precis. Eng.*, vol. 3, no. 2, pp. 61–83, Apr. 1981.
[135] C. W. Jones and R. K. Leach, “Adding a dynamic aspect to amplitude–wavelength space,” *Meas. Sci. Technol.*, vol. 19, no. 5, p. 55105, May

2008.
[136] S. Rosén, T. R. Thomas, and B.-G. Rosén, “The Stedman diagram revisited,” *Surf. Topogr. Metrol. Prop.*, vol. 2, no. 1, p. 14005, Dec. 2013.
[137] M. Merola, A. Ruggiero, J. S. De Mattia, and S. Affatato, “On the tribological behavior of retrieved hip femoral heads affected by metallic debris. A comparative investigation by stylus and optical profilometer for a new roughness measurement protocol,” *Meas. J. Int. Meas. Confed.*, vol. 90, 2016.
[138] S. Affatato, G. Bersaglia, Y. Junqiang, F. Traina, A. Toni, and M. Viceconti, “The predictive Power of Surface Profile Parameters on the Amount of Wear Measured In Vitro on Metal-On-Polyethylene Artificial Hip Joints,” *Proc. Inst. Mech. Eng. Part H J. Eng. Med.*, vol. 220, no. 3, pp. 457–464, Jan. 2006.
[139] P. Taddei, S. Tozzi, S. Carmignato, and S. Affatato, “May the surface roughness of the retrieved femoral head influence the wear behavior of the polyethylene liner?,” *J Biomed Mater Res B Appl Biomater*, pp. 1–12, 2015.
[140] C. Y. Poon and B. Bhushan, “Comparison of surface roughness measurements by stylus profiler, AFM and non-contact optical profiler,” *Wear*, vol. 190, no. 1, pp. 76–88, 1995.
[141] P. Samyn, J. Van Erps, and H. Thienpont, “Relation between optical non-contact profilometry and AFM roughness parameters on coated papers with oil-filled nanoparticles,” *Measurement*, vol. 82, pp. 75–93, 2016.
[142] D. H. Lee, “3-Dimensional profile distortion measured by stylus type surface profilometer,” *Meas. J. Int. Meas. Confed.*, vol. 46, no. 1, pp. 803–814, 2013.
[143] D. J. Whitehouse, *Surfaces and their Measurement*. Elsevier, 2004.
[144] T. V. Vorburger, H. G. Rhee, T. B. Renegar, J. F. Song, and A. Zheng, “Comparison of optical and stylus methods for measurement of surface texture,” *Int. J. Adv. Manuf. Technol.*, vol. 33, no. 1–2, pp. 110–118, 2007.
[145] M. N. Durakbasa, P. H. Osanna, M. E. Yurci, and P. Aksoy, “Contact and Contactless Investigations of Manufactured High-Precise Surface Structures,” pp. 1962–1965, 2009.
[146] P. Demircioglu and M. N. Durakbasa, “Investigations on machined metal surfaces through the stylus type and optical 3D instruments and their mathematical modeling with the help of statistical techniques,” *Meas. J. Int. Meas. Confed.*, vol. 44, no. 4, pp. 611–619, 2011.
[147] M. N. Durakbasa, P. H. Osanna, and P. Demircioglu, “The factors affecting surface roughness measurements of the machined flat and spherical surface structures – The geometry and the precision of the surface,” *Measurement*, vol. 44, no. 10, pp. 1986–1999, 2011.

[148] E. S. Gadelmawla, M. M. Koura, T. M. A. Maksoud, I. M. Elewa, and H. H. Soliman, “Roughness parameters.”
[149] F. . Falez, F. . La Cava, and G. . Panegrossi, “Femoral prosthetic heads and their significance in polyethylene wear,” *Int. Orthop.*, vol. 24, pp. 126–129, 2000.
[150] R. S. Timsit, “Electrical Contacts Resistance: Fundamental Principles,” in *Electrical Contacts: Principles and Applications*, P. G. Slade, Ed. New York: Marcel Dekker, Inc, 1999, p. 1104.
[151] R. D’Amato, “Análisis y Modelizado del Comportamiento Dinámico de Articulaciones Humanas Mediante la Caracterización Metrológica y Tribológica de Sus Superficies,” Univerisdad Politecnica de Madrid, 2017.
[152] B. J. Hamrock and D. Dowson, “Elastohydrodynamic Lubrication of Elliptical Contacts for Materials of Low Elastic-Modulus I - Fully Flooded Conjunction,” *Trans. ASME, J. Lubr. Technol.*, vol. 100, no. 2, pp. 236–245, 1978.
[153] M. Jagatia and Z. M. Jin, “Elastohydrodynamic lubrication analysis of metal-on-metal hip prostheses under steady state entraining motion.,” *Proc. Inst. Mech. Eng. H.*, vol. 215, no. 6, pp. 531–541, 2001.
[154] D. C. Wright and Rapra Technology Limited., *Failure of polymer products due to thermo-oxidation.* Rapra Technology Limited, 2001.
[155] S. Affatato, M. Goldoni, M. Testoni, and A. Toni, “Mixed oxides prosthetic ceramic ball heads. Part 3: effect of the ZrO2 fraction on the wear of ceramic on ceramic hip joint prostheses. A long-term in vitro study,” *Biomaterials*, vol. 22, pp. 717–723, 2001.
[156] S. Affatato *et al.*, “Advanced nanocomposite materials for orthopaedic applications. I. A long-term in vitro wear study of zirconia-toughened alumina,” *J. Biomed. Mater. Res. - Part B Appl. Biomater.*, vol. 78, no. 1, pp. 76–82, 2006.
[157] S. Williams, J. J. Wu, a Unsworth, and I. Khan, “Wear and surface analysis of 38 mm ceramic-on-metal total hip replacements under standard and severe wear testing conditions,” *Proc. Inst. Mech. Eng. Part H J. Eng. Med.*, vol. 225, no. 8, pp. 783–796, 2011.
[158] S. Affatato, E. Modena, A. Toni, and P. Taddei, “Retrieval analysis of three generations of Biolox® femoral heads: spectroscopic and SEM characterization.,” *J. Mech. Behav. Biomed. Mater.*, vol. 13, pp. 118–128, Sep. 2012.
[159] S. Affatato, M. Zavalloni, P. Taddei, M. Di Foggia, C. Fagnano, and M. Viceconti, “Comparative study on the wear behaviour of different conventional and cross-linked polyethylenes for total hip replacement,” *Tribol. Int.*, vol. 41, no. 8, pp. 813–822, Aug. 2008.
[160] Q. Wang, J. Liu, and S. Ge, “Study on Biotribological Behavior of the Combined Joint of CoCrMo and UHMWPE/BHA Composite in a Hip Joint Simulator,” *J. Bionic Eng.*, vol. 6, no. 4, pp. 378–386, 2009.

[161] S. Ge, S. Wang, and X. Huang, "Increasing the wear resistance of UHMWPE acetabular cups by adding natural biocompatible particles," *Wear*, vol. 267, no. 5–8, pp. 770–776, 2009.
[162] C. L. Brockett, G. John, S. Williams, Z. Jin, G. H. Isaac, and J. Fisher, "Wear of ceramic-on-carbon fiber-reinforced poly-ether ether ketone hip replacements," *J. Biomed. Mater. Res. - Part B Appl. Biomater.*, vol. 100 B, no. 6, pp. 1459–1465, 2012.
[163] A. Borruto, "A new material for hip prosthesis without considerable debris release," *Med. Eng. Phys.*, vol. 32, no. 8, pp. 908–913, 2010.
[164] A. Ruggiero, E. Gómez, and R. D'Amato, "Approximate closed-form solution of the synovial fluid film force in the human ankle joint with non-Newtonian lubricant," *Tribol. Int.*, vol. 57, pp. 156–161, 2013.
[165] R. D'Amato, R. Calvo, and E. Gómez, "Sensitivity study of the morphometric fitting on the pressure field inside ankle joints," *Case Stud. Mech. Syst. Signal Process.*, vol. 1, pp. 8–14, Jul. 2015.
[166] M. Fellah *et al.*, "Tribological behavior of Ti-6Al-4V and Ti-6Al-7Nb Alloys for Total Hip Prosthesis," *Adv. Tribol.*, vol. 2014, pp. 1–13, Jul. 2014.
[167] S. A. Jaber, A. Ruggiero, S. Battaglia, and S. Affatato, "On the roughness measurement on knee prostheses.," *Int. J. Artif. Organs*, vol. 38, no. 1, pp. 39–44, Jan. 2015.
[168] H. Liang, B. Shi, A. Fairchild, and T. Cale, "Applications of plasma coatings in artificial joints: an overview," *Vacuum*, vol. 73, no. 3–4, pp. 317–326, Apr. 2004.
[169] R. M. Hall and A. Unsworth, "Friction in hip prostheses.," *Biomaterials*, vol. 18, no. 15, pp. 1017–26, Aug. 1997.
[170] A. Wang, A. Essner, and G. Schmidig, "The effects of lubricant composition onin vitro wear testing of polymeric acetabular components," *J. Biomed. Mater. Res.*, vol. 68B, no. 1, pp. 45–52, Jan. 2004.
[171] T. Kitano, G. A. Ateshian, V. C. Mow, Y. Kadoya, and Y. Yamano, "Constituents and pH changes in protein rich hyaluronan solution affect the biotribological properties of artificial articular joints," *J. Biomech.*, vol. 34, no. 8, pp. 1031–1037, Aug. 2001.
[172] V. Saikko, O. Calonius, and J. Keränen, "Effect of counterface roughness on the wear of conventional and crosslinked ultrahigh molecular weight polyethylene studied with a multi-directional motion pin-on-disk device.," *J. Biomed. Mater. Res.*, vol. 57, no. 4, pp. 506–12, Dec. 2001.
[173] M. P. Gispert, a. P. Serro, R. Colaço, and B. Saramago, "Friction and wear mechanisms in hip prosthesis: Comparison of joint materials behaviour in several lubricants," *Wear*, vol. 260, no. 1–2, pp. 149–158, 2006.
[174] *ISO 11357-1:2009 - Plastics -- Differential scanning calorimetry*

(DSC) -- Part 1: General principles. 2009.
[175] F. J. Buchanan, J. R. White, B. Sim, and S. Downes, "The influence of gamma irradiation and aging on degradation mechanisms of ultra-high molecular weight polyethylene," *J. Mater. Sci. Mater. Med.*, vol. 12, no. 1, pp. 29–37, 2001.
[176] J. M. Axe, L. Snyder-Mackler, and M. J. Axe, "The Role of Viscosupplementation," *Sports Med. Arthrosc.*, vol. 21, no. 1, pp. 18–22, Mar. 2013.
[177] D. Cerniglia, T. Ingrassia, L. D'Acquisto, and M. Saporito, "Contact between the components of a knee prosthesis: numerical and experimental study," *Fract. Struct. Integr.*, vol. 22, pp. 56–68, 2012.
[178] L. Zach, L. Horak, P. Ruzicka, and S. Konvickova, "Knee Joint Edoprosthesis - Verification of Contact Pressures by Pressure Sensitive Films," vol. II, pp. 6–9, 2008.
[179] M. R. Gevaert, M. LaBerge, J. M. Gordon, and J. D. DesJardins, "The Quantification of Physiologically Relevant Cross-Shear Wear Phenomena on Orthopaedic Bearing Materials Using the MAX-Shear Wear Testing System," *J. Tribol.*, vol. 127, no. 4, p. 740, Oct. 2005.
[180] C. Liu, L. Ren, R. D. Arnell, and J. Tong, "Abrasive wear behavior of particle reinforced ultrahigh molecular weight polyethylene composites," *Wear*, vol. 225–229, pp. 199–204, Apr. 1999.
[181] A. Ruggiero, M. Merola, P. Carlone, and V.-M. Archodoulaki, "Tribo-mechanical characterization of reinforced epoxy resin under dry and lubricated contact conditions," *Compos. Part B Eng.*, vol. 79, pp. 595–603, 2015.
[182] H. Ito, C. M. Maloney, R. D. Crowninshield, J. C. Clohisy, D. J. McDonald, and W. J. Maloney, "In Vivo Femoral Head Damage and Its Effect on Polyethylene Wear," *J. Arthroplasty*, vol. 25, no. 2, pp. 302–308, 2010.
[183] J.-M. Brandt *et al.*, "Clinical failure analysis of contemporary ceramic-on-ceramic total hip replacements," *Proc. Inst. Mech. Eng. Part H J. Eng. Med.* , vol. 227, no. 8, pp. 833–846, Aug. 2013.
[184] B. S. Bal, M. N. Rahaman, T. Aleto, F. S. Miller, F. Traina, and A. Toni, "The significance of metal staining on alumina femoral heads in total hip arthroplasty.," *J. Arthroplasty*, vol. 22, no. 1, pp. 14–9, Jan. 2007.
[185] A. W. Eberhardt, R. T. McKee, J. M. Cuckler, D. W. Peterson, P. R. Beck, and J. E. Lemons, "Surface Roughness of CoCr and ZrO(2) Femoral Heads with Metal Transfer: A Retrieval and Wear Simulator Study.," *Int. J. Biomater.*, no. October, p. Article ID 185456, 2009.
[186] A. G. Della Valle, S. Doty, G. Gradl, A. Labissiere, and B. J. Nestor, "Wear of a highly cross-linked polyethylene liner associated with metallic deposition on a ceramic femoral head," *J. Arthroplasty*, vol. 19, no. 4, pp. 532–536, Jun. 2004.

[187] L. Que, L. D. Timmie Topoleski, and N. L. Parks, “Surface roughness of retrieved CoCrMo alloy femoral components from PCA artificial total knee joints,” *J. Biomed. Mater. Res.*, vol. 53, no. 1, pp. 111–118, 2000.

[188] B. Welghtman and D. Light, “The effect of the surface finish of alumina and stainless steel on the wear rate of UHMW polyethylene,” *Biomaterials*, vol. 7, no. 1, pp. 20–24, Jan. 1986.

[189] J. R. Cooper, D. Dowson, and J. Fisher, “The effect of transfer film and surface roughness on the wear of lubricated ultra-high molecular weight polyethylene,” *Clin. Mater.*, vol. 14, no. 4, pp. 295–302, Jan. 1993.

[190] C. Chang, J. Yoo, W. Song, D. Kim, K. KH, and K. HJ, “Transfer of metallic debris from the metal surface of an acetabular cup to artificial femoral heads by scraping: comparison between alumina and cobalt-chrome heads,” *J. Biomed. Mater. Res. - Part B Appl. Biomater.*, vol. 85, no. 1, pp. 204–209, 2008.

[191] D. Chen, S. Lin, N. Cutrera, D. Padgett, and T. Wright, “Ceramic bearings in total hip replacement: a retrieval analysis,” *Minerva Ortop. e Traumatol.*, vol. 61, no. 1, pp. 46–49, 2010.

[192] M. Elpers, D. Nam, S. Boydston-White, M. P. Ast, T. M. Wright, and D. E. Padgett, “Zirconia Phase Transformation, Metal Transfer, and Surface Roughness in Retrieved Ceramic Composite Femoral Heads in Total Hip Arthroplasty,” *J. Arthroplasty*, vol. 29, no. 11, pp. 2219–2223, 2014.

[193] S. Affatato, A. Ruggiero, J. S. De Mattia, and P. Taddei, “Does metal transfer affect the tribological behaviour of femoral heads? Roughness and phase transformation analyses on retrieved zirconia and Biolox® Delta composites,” *Compos. Part B Eng.*, vol. 92, pp. 290–298, May 2016.

[194] Y. Abu-amer, I. Darwech, and J. C. Clohisy, “Aseptic loosening of total joint replacements : mechanisms underlying osteolysis and potential therapies,” vol. 7, pp. 1–7, 2007.

[195] A. Astarita *et al.*, “On the Improvement of AA2024 Wear Properties through the Deposition of a Cold-Sprayed Titanium Coating,” *Metals (Basel).*, vol. 6, no. 8, p. 185, 2016.

[196] M. Merola, A. Ruggiero, J. S. De Mattia, and S. Affatato, “On the tribological behavior of retrieved hip femoral heads affected by metallic debris. A comparative investigation by stylus and optical profilometer for a new roughness measurement protocol,” *Measurement*, vol. 90, pp. 365–371, Aug. 2016.

[197] P. Hreha *et al.*, “Roughness Parameters Calculation By Means Of On-Line Vibration Monitoring Emerging From AWJ Interaction With Material,” *Metrol. Meas. Syst.*, vol. 22, no. 2, pp. 315–326, Jan. 2015.

[198] Z. Lipa and D. Tomaníčková, “Choosing The Most Appropriate

Mathematical Model To Approximate The Abbott Curve," *Mater. Sci. Technol.*, pp. 37–43, 2010.
[199] "ISO 13565-2:1996 Geometrical Product Specifications (GPS) - Surface texture: Profile method; Surfaces having stratified functional properties -- Part 2: Height characterization using the linear material ratio curve." 1996.
[200] M. Wakuda, Y. Yamauchi, S. Kanzaki, and Y. Yasuda, "Effect of surface texturing on friction reduction between ceramic and steel materials under lubricated sliding contact," *Wear*, vol. 254, no. 3, pp. 356–363, 2003.
[201] Z. M. Jin, J. B. Medley, and D. Dowson, "Fluid film lubrication in artificial hip joints," *Tribol. Res. Des. Eng. Syst.*, pp. 237–256, 2003.
[202] F. W. Chan, J. D. Bobyn, J. B. Medley, J. J. Krygier, and M. Tanzer, "The Otto Aufranc Award. Wear and lubrication of metal-on-metal hip implants.," *Clin. Orthop. Relat. Res.*, no. 369, pp. 10–24, Dec. 1999.
[203] A. Ruggiero, E. Gòmez, and R. D'Amato, "Approximate analytical model for the squeeze-film lubrication of the human ankle joint with synovial fluid filtrated by articular cartilage," *Tribol. Lett.*, vol. 41, no. 2, pp. 337–343, 2011.
[204] A. Ruggiero, S. Hloch, D. Kozak, and P. Valasek, "Analytical fluid film force calculation in the case of short bearing with a fully developed turbulent flow," *Proc. Inst. Mech. Eng. Part J J. Eng. Tribol.*, vol. 230, no. 4, pp. 395–401, Apr. 2016.
[205] D. Dowson, "New joints for the Millennium: wear control in total replacement hip joints.," *Proc. Inst. Mech. Eng. H.*, vol. 215, no. 4, pp. 335–58, 2001.
[206] W. T. Luchetti, L. A. Copley, E. J. Vresilovic, J. Black, and M. E. Steinberg, "Drain entrapment and titanium to ceramic head deposition: Two unique complications following closed reduction of a disclocated total hip arthroplasty," *J. Arthroplasty*, vol. 13, no. 6, pp. 713–717, 1998.
[207] G. V. B. Cochran, *A primer of orthopaedic biomechanics*. Churchill Livingstone, 1982.
[208] R. F. Chandler, C. E. Clauser, J. T. McConville, H. M. Reynolds, and J. W. Young, "Investigatio of Intertial Properties of the Human Body," Mar. 1975.
[209] B. M. van Bolhuis and C. C. A. M. Gielen, "A comparison of models explaining muscle activation patterns for isometric contractions," *Biol. Cybern.*, vol. 81, no. 3, pp. 249–261, Sep. 1999.
[210] U. Glitsch and W. Baumann, "The three-dimensional determination of internal loads in the lower extremity.," *J. Biomech.*, vol. 30, no. 11–12, pp. 1123–31, Nov. 1997.
[211] C. . Vaughan, B. L. Davis, and J. C. O'Connor, "The Man data set provided at the website of the International Society of Biomechanics,"

Human Kinetic Publisher, 1992. [Online]. Available: http://isbweb.org/o/content/view/66/73.

[212] J. Schwiesau *et al.*, "Definition and evaluation of testing scenarios for knee wear simulation under conditions of highly demanding daily activities," *Med. Eng. Phys.*, vol. 35, no. 5, pp. 591–600, 2013.

[213] S. Battaglia, C. Belvedere, S. A. Jaber, S. Affatato, V. D'Angeli, and A. Leardini, "A new protocol from real joint motion data for wear simulation in total knee arthroplasty: stair climbing," *Med. Eng. Phys.*, vol. 36, pp. 1605–1610, 2014.

[214] S. A. Jaber, P. Taddei, S. Tozzi, A. Sudanese, and S. Affatato, "In vitro effects on mobile polyethylene insert under highly demanding daily activities: stair climbing.," *Int. Orthop.*, 2014.

[215] S. Battaglia, P. Taddei, E. Castiello, S. Tozzi, A. Sudanese, and S. Affatato, "Combined effect of the body mass index and implant size on the wear of retrieved total knee prostheses.," *J. Mech. Behav. Biomed. Mater.*, vol. 38, pp. 69–77, 2014.

[216] H. M. J. McEwen *et al.*, "The influence of design, materials and kinematics on the in vitro wear of total knee replacements," *J. Biomech.*, vol. 38, no. 2, pp. 357–365, 2005.

[217] S. Battaglia, P. Taddei, S. Tozzi, A. Sudanese, and S. Affatato, "Toward the interpretation of the combined effect of size and body weight on the tribological performance of total knee prostheses," *Int Orthop*, 2014.

[218] C. L. Vaughan, B. L. Davis, and J. C. O'Connor, *Dynamics of gait*. Human Kinetics Publishers, 1992.

[219] G. Bergmann *et al.*, "Standardized loads acting in knee implants.," *PLoS One*, vol. 9, no. 1, p. e86035, Jan. 2014.

[220] J. D. DesJardins, B. Burnikel, and M. LaBerge, "UHMWPE wear against roughened oxidized zirconium and CoCr femoral knee components during force-controlled simulation," *Wear*, vol. 264, no. 3–4, pp. 245–256, Feb. 2008.

[221] G. Bergmann *et al.*, "Standardized loads acting in knee implants.," *PLoS One*, vol. 9, no. 1, p. e86035, Jan. 2014.

[222] M. Harman, S. Affatato, M. Spinelli, M. Zavalloni, S. Stea, and a Toni, "Polyethylene insert damage in unicondylar knee replacement: a comparison of *in vivo* function and *in vitro* simulation," *Proc. Inst. Mech. Eng. Part H J. Eng. Med.*, vol. 224, no. 7, pp. 823–830, Jul. 2010.

[223] A. Ruggiero, R. D'Amato, and E. Gómez, "Experimental analysis of tribological behavior of UHMWPE against AISI420C and against TiAl6V4 alloy under dry and lubricated conditions," *Tribol. Int.*, vol. 92, pp. 154–161, 2015.

[224] F. E. Kennedy *et al.*, "Contact fatigue failure of ultra-high molecular weight polyethylene bearing components of knee prostheses," *J.*

Tribol. Asme, vol. 122, no. 1, pp. 332–339, 2000.
[225] V. Saikko, "Effect of contact pressure on wear and friction of ultra-high molecular weight polyethylene in multidirectional sliding," *Proc Inst Mech Eng [H]*, vol. 220, no. 7, pp. 723–731, 2006.
[226] a Lakdawala, S. Todo, and G. Scott, "The significance of surface changes on retrieved femoral components after total knee replacement.," *J. Bone Joint Surg. Br.*, vol. 87, no. 6, pp. 796–9, 2005.
[227] J.-M. M. Brandt, L. Guenther, S. O'Brien, A. Vecherya, T. R. Turgeon, and E. R. Bohm, "Performance assessment of femoral knee components made from cobalt-chromium alloy and oxidized zirconium," *Knee*, vol. 20, no. 6, pp. 388–396, Dec. 2013.
[228] T. J. Heyse, M. E. Elpers, D. H. Nawabi, T. M. Wright, and S. B. Haas, "Oxidized zirconium versus cobalt-chromium in TKA: profilometry of retrieved femoral components.," *Clin. Orthop. Relat. Res.*, vol. 472, no. 1, pp. 277–83, Jan. 2014.
[229] S. Banks, J. Bellemans, H. Nozaki, L. A. Whiteside, M. Harman, and W. A. Hodge, "Knee motions during maximum flexion in fixed and mobile-bearing arthroplasties," *Clin Orthop Relat Res*, no. 410, pp. 131–138, 2003.
[230] S. Affatato, M. Zavalloni, M. Spinelli, L. Costa, P. Bracco, and M. Viceconti, "Long-term in-vitro wear performance of an innovative thermo-compressed cross-linked polyethylene," *Tribol. Int.*, vol. 43, no. 1–2, pp. 22–28, Jan. 2010.
[231] M. Merola, P. Carlone, A. Ruggiero, and V. M. Archodoulaki, "Mechanical and Tribological Characterization of Composite Laminates Manufactured by Liquid Composite Molding Processes," *Key Eng. Mater.*, vol. 651–653, pp. 907–912, 2015.
[232] J. H. Dumbleton, *Tribology of Natural and Artificial Joints*. New York: Elsevier, 1981.
[233] D. Petersen *et al.*, "The Significance of Nonlinear Motion in the Wear Screening of Orthopaedic Implant Materials," *J. Test. Eval.*, vol. 25, no. 2, p. 239, Mar. 1997.
[234] S. Barreto, J. Folgado, P. R. Fernandes, and J. Monteiro, "The Influence of the Pelvic Bone on the Computational Results of the Acetabular Component of a Total Hip Prosthesis," *J. Biomech. Eng.*, vol. 132, no. 5, p. 54503, 2010.
[235] M. S. Uddin and L. C. Zhang, "Predicting the wear of hard-on-hard hip joint prostheses," *Wear*, vol. 301, no. 1–2, pp. 192–200, Apr. 2013.
[236] R. Pietrabissa, M. Raimondi, and E. Di Martino, "Wear of polyethylene cups in total hip arthroplasty: a parametric mathematical model," *Med. Eng. Phys.*, vol. 20, no. 3, pp. 199–210, Apr. 1998.
[237] A. Wang, A. Essner, and R. Klein, "Effect of contact stress on friction and wear of ultra-high molecular weight polyethylene in total hip replacement," *Proc. Inst. Mech. Eng. Part H J. Eng. Med.*, vol. 215,

no. 2, pp. 133–139, Feb. 2001.
[238] S. H. Teoh, W. H. Chan, and R. Thampuran, “An elasto-plastic finite element model for polyethylene wear in total hip arthroplasty,” *J. Biomech.*, vol. 35, no. 3, pp. 323–330, 2002.
[239] T. A. Maxian, T. D. Brown, D. R. Pedersen, and J. J. Callaghan, “A sliding-distance-coupled finite element formulation for polyethylene wear in total hip arthroplasty,” *J. Biomech.*, vol. 29, no. 5, pp. 687–692, May 1996.
[240] J. M. Kabo, J. S. Gebhard, G. Loren, and H. C. Mastutz, “In vivo wear of polyethylene acetabular components,” *J. Bone Jt. Surgery1*, vol. 75–B, no. 2, pp. 254–258, 1993.
[241] V. D’Agostino, *Fondamenti di Tribologia*. Naples: CUEN, 1988.
[242] S. L. Bevill, G. R. Bevill, J. R. Penmetsa, A. J. Petrella, and P. J. Rullkoetter, “Finite element simulation of early creep and wear in total hip arthroplasty,” *J. Biomech.*, vol. 38, no. 12, pp. 2365–2374, Dec. 2005.
[243] T. A. Maxian, T. D. Brown, D. R. Pedersen, and J. J. Callaghan, “Adaptiive finite element modeling of long-term polyethylene wear in total hip arthroplasty,” *J. Orthop. Res.*, vol. 14, no. 4, pp. 668–675, Jul. 1996.
[244] G. Matsoukas, R. Willing, and I. Y. Kim, “Total Hip Wear Assessment: A Comparison Between Computational and In Vitro Wear Assessment Techniques Using ISO 14242 Loading and Kinematics,” *J. Biomech. Eng.*, vol. 131, no. 4, p. 41011, Apr. 2009.
[245] T. R. Thomas, “Trends in surface roughness,” *Int. J. Mach. Tools Manuf.*, vol. 38, no. 5–6, pp. 405–411, May 1998.
[246] “Physical Examination: Gait | Epomedicine.” [Online]. Available: http://epomedicine.com/clinical-medicine/physical-examination-gait/. [Accessed: 20-Nov-2017].